

ABSTRACT

Title of Document: IN-SITU MEASUREMENT OF EPITHELIAL TISSUE OPTICAL PROPERTIES: DEVELOPMENT AND IMPLEMENTATION OF DIFFUSE REFLECTANCE SPECTROSCOPY TECHNIQUES

Quanzeng Wang, Doctor of Philosophy, 2009

Directed By: Professor Nam Sun Wang, Department of Chemical & Biomolecular Engineering

Cancer is a severe threat to human health. Early detection is considered the best way to increase the chance for survival. While the traditional cancer detection method, biopsy, is invasive, noninvasive optical diagnostic techniques are revolutionizing the way that cancer is diagnosed. Reflectance spectroscopy is one of these optical spectroscopy techniques showing promise as a diagnostic tool for pre-cancer detection. When a neoplasia occurs in tissue, morphologic and biochemical changes happen in the tissue, which in turn results in the change of optical properties and reflectance spectroscopy. Therefore, a pre-cancer can be detected by extracting optical properties from reflectance spectroscopy.

This dissertation described the construction of a fiberoptic based reflectance system and the development of a series of modeling studies. This research is aimed at establishing an improved understanding of the optical properties of mucosal tissues by analyzing reflectance signals at different wavelengths. The ultimate goal is to reveal the potential of reflectance-based optical diagnosis of pre-cancer. The research is detailed in Chapter 3 through Chapter 5. Although related with each other, each chapter was designed to become a journal paper ultimately. In Chapter 3, a multi-wavelength, fiberoptic system was constructed, evaluated and implemented to determine internal tissue optical properties at ultraviolet A and visible wavelengths. A

condensed Monte Carlo model was deployed to simulate light-tissue interaction and generate spatially distributed reflectance data. These data were used to train an inverse neural network model to extract tissue optical properties from reflectance. Optical properties of porcine mucosal and liver tissues were finally measured. In Chapter 4, the condensed Monte Carlo method was extended so that it can rapidly simulate reflectance from a single illumination-detection fiber thus enabling the calculation of large data sets. The model was implemented to study spectral reflectance changes due to breast cancer. The effect of adding an illumination-detection fiber to a linear array fiber for optical property determination was also evaluated. In Chapter 5, an investigation of extracting the optical properties from two-layer tissues was performed. The relationship between spatially-resolved reflectance distributions and optical properties in two-layer tissue was investigated. Based on all the aforementioned studies, spatially resolved reflectance system coupled with condensed Monte Carlo and neural network models was found to be objective and appear to be sensitive and accurate in quantitatively assessing optical property change of mucosal tissues.

**IN-SITU MEASUREMENT OF EPITHELIAL TISSUE OPTICAL PROPERTIES:
DEVELOPMENT AND IMPLEMENTATION OF DIFFUSE REFLECTANCE
SPECTROSCOPY TECHNIQUES**

By

Quanzeng Wang

Dissertation submitted to the Faculty of the Graduate School of the
University of Maryland, College Park, in partial fulfillment
of the requirements for the degree of
Doctor of Philosophy
2009

Advisory Committee:
Professor Nam Sun Wang, Chair
Doctor Josh Pfefer
Professor William E. Bentley
Professor Srinivasa R. Raghavan
Professor Yang Tao
Professor Kyu Yong Choi

© Copyright by
Quanzeng Wang
2009

Acknowledgements

I am extremely grateful to both of my advisors, Prof. Nam Sun Wang at the University of Maryland (UM) and Dr. Joshua Pfefer at the Food and Drug Administration (FDA), for seeing my research potential and pushing me to complete my PhD degree. Without their guidance and invaluable suggestions, I wouldn't have been possible to finish my degree and get my publications done. I want to express my appreciation to all of the members of my laboratory at UM for their continuous friendship and support. I appreciate the help from the physics division of the Center for Devices and Radiological Health in FDA. The division provided me a great laboratory and environment for my research and the staff in the division was just wonderful. I would also like to thank my committee members, Willian E. Bentley, Srinivasa R. Raghavan, Kyu Yong Choi, and Yang Tao, who have known me for several years now and have never wavered their support of me. It was a privilege to have them on my PhD committee.

Finally, I would like to extend my deepest gratitude to my wife, my parents, my brother, and my other family members, who have always believed in me and love me. Special thanks are given to my eight-month old son. He brought me the greatest pleasure and supported me by behaving well.

Table of Contents

Acknowledgements.....	ii
Table of Contents.....	iii
List of Tables.....	v
List of Figures.....	vi
Chapter 1. Introduction.....	1
1.1 Overview.....	1
1.2 Overall objective.....	3
1.3 Organization of the dissertation.....	4
Chapter 2. Background.....	8
2.1 Interaction of light with tissue.....	8
2.1.1 Absorption and scattering – the basic.....	8
2.1.2 Tissue absorption.....	9
2.1.3 Tissue scattering.....	12
2.2 Significance of study of optical properties.....	18
2.2.1 For disease diagnosis.....	18
2.2.2 For disease treatment.....	20
2.2.3 For tissue monitoring.....	20
2.2.4 For theoretical study.....	20
2.3 Tissue-simulating phantoms.....	21
2.3.1 Phantom composition.....	21
2.3.2 Determination of phantom μ_a - Beer's law.....	23
2.3.3 Determination of phantom μ_s - Mie theory.....	25
2.4 Spectroscopy techniques for measuring tissue optical properties.....	26
2.4.1 Spectrophotometer with an integrating sphere.....	27
2.4.2 Fiberoptic-based spectroscopy techniques.....	29
Chapter 3. Optical property measurement of single-layer tissues with a fiberoptic reflectance system.....	32
3.1 Introduction.....	32
3.2 Monte Carlo modeling of light transport in single-layer tissues.....	33
3.3 Condensed Monte Carlo modeling of single-layer tissues.....	37
3.4 Development and evaluation of neural network models for single-layer tissues.....	43
3.5 Construction of single-layer phantoms.....	49
3.6 Construction and calibration of the fiberoptic diffuse reflectance system.....	54
3.6.1 Light source.....	54
3.6.2 Construction of the fiberoptic diffuse reflectance system.....	55
3.6.3 Measurement of absolute reflectance intensity.....	56
3.6.4 System calibration - Converting intensity to reflectance.....	57
3.7 <i>In vitro</i> validation of the reflectance system.....	60
3.8 <i>Ex vivo</i> tissue measurements.....	62
3.9 Conclusion.....	69
Chapter 4. Optical study of single-layer tissues with an illumination-detection fiber.....	71

4.1	Introduction.....	71
4.2	Condensed Monte Carlo simulation for an illumination-detection fiber.....	73
4.2.1	Convolution equations for an illumination-detection fiber.....	73
4.2.2	Scaling equation for maximum penetration depth.....	75
4.2.3	Condensed Monte Carlo model.....	76
4.2.4	Evaluation of convolution equations for an illumination-detection fiber and the scaling equation for maximum penetration depth of a photon.....	77
4.3	Effect of fiber diameter on reflectance from an illumination-detection fiber.....	84
4.4	Reflectance from an illumination-detection fiber to improve the accuracy of neural network.....	87
4.5	Reflectance spectra of breast tissues from illumination-detection fibers.....	89
4.6	Maximum penetration depth of a photon and detection depth of a fiber.....	92
4.7	Conclusions.....	103
Chapter 5.	Optical property measurement of layered tissues.....	105
5.1	Introduction.....	105
5.2	Multi-layer Monte Carlo simulation.....	107
5.3	Multi-layer fast Monte Carlo simulation.....	109
5.4	Influence of optical properties of each layer on reflectance.....	113
5.5	Determination of optical properties of a two-layer tissue with neural network models.....	119
5.6	Conclusions.....	122
Chapter 6.	Concluding remarks.....	124
6.1	Summary and contributions.....	124
6.2	Suggestions for future study.....	125
	Bibliography.....	127

List of Tables

Table 1. Absolute errors of four neural networks (cm^{-1})	45
Table 2. Refractive indexes of water and polystyrene at different wavelengths.....	52
Table 3. The anisotropy factors of polystyrene microspheres in water.....	52
Table 4. Optical properties from literature.....	68
Table 5. Optical properties for evaluation of the scaling equation	81
Table 6. Absolute errors of neural networks (cm^{-1})	89
Table 7. Detection depth of fibers into different tissues (cm)	97
Table 8. Monte Carlo simulation parameters of a 3-layer tissue	107
Table 9. Monte Carlo simulation parameters of a 2-layer tissue	112
Table 10. Parameters of fast Monte Carlo simulations	113
Table 11. Fiber geometries for neural network training (radius of each fiber is 0.1 mm)	120
Table 12. Optical property estimation errors for neural networks based on four different probe geometries.....	122

List of Figures

Fig. 1 Propagation of photons in a tissue.....	10
Fig. 2 Absorption coefficient of hemoglobin.....	11
Fig. 3 Absorption coefficient of water.....	12
Fig. 4 Sizes of some biological scatterers.....	13
Fig. 5 A scattering event with a deflection angle and an azimuthal angle.....	14
Fig. 6 The phase function of a Rayleigh scattering.....	16
Fig. 7 The phase function of a Mie scattering.....	17
Fig. 8 μ_s' of dermis.....	18
Fig. 9 Light intensity as a function of depth (cm) in media with different μ_a (cm^{-1}).....	24
Fig. 10 Refractive indexes of polystyrene and water.....	26
Fig. 11 Measurement of reflectance and transmittance with one integrating sphere.....	28
Fig. 12 Flow chart of the investigation.....	33
Fig. 13 Deflection of a photon by scattering event.....	34
Fig. 14 Simulation results of a semi-infinite homogeneous tissue.....	35
Fig. 15 Simulation results of a homogeneous bulk tissue.....	36
Fig. 16 Diffuse reflectance as a function of radius (r) - Comparison of MC simulation results with results from literature.....	37
Fig. 17 The 4 mm diameter face of the fiberoptic probe.....	39
Fig. 18 Contours of dimensionless reflectance from each detection fiber with radius of 0.1 mm.....	43
Fig. 19 The calculated μ_a and μ_s' from the neural network based on four detection fibers versus their theoretical values.....	47
Fig. 20 Absolute errors of μ_a and μ_s' of each evaluation dataset from neural network based on 4 detection fibers.....	49
Fig. 21 μ_a of nigrosine as a function of wavelength at different concentrations.....	50
Fig. 22 μ_a of nigrosine as a function of concentration at different wavelengths.....	51
Fig. 23 μ_a of hemoglobin as a function of wavelength at different concentrations.....	51
Fig. 24 μ_a of hemoglobin as a function of concentration at different wavelengths.....	51
Fig. 25 μ_s' of polystyrene microsphere (0.989 micron diameter) as a function of wavelength.....	53
Fig. 26 μ_s' of polystyrene microsphere (0.989 micron diameter) as a function of density.....	53
Fig. 27 Phantoms with increasing μ_a and μ_s' held constant (nigrosine as absorber).....	54
Fig. 28 Multi-wavelength, fiberoptic diffuse reflectance system for optical property measurement.....	56
Fig. 29 Light propagation and the detection of scattered light by a fiber probe.....	57
Fig. 30 Light intensity at tissue surface as a function of distance from an illumination fiber.....	57
Fig. 31 CCD camera image of light intensity obtained by the five detection fibers.....	57
Fig. 32 Reflectance versus intensity per mJ of illumination light at 325 nm.....	59
Fig. 33 Reflectance versus intensity per mJ of illumination light at 375 nm.....	59

Fig. 34 Reflectance versus intensity per mJ of illumination light at 405 nm.....	59
Fig. 35 Reflectance versus intensity per mJ of illumination light at 445 nm.....	60
Fig. 36 Reflectance versus intensity per mJ of illumination light at 543 nm.....	60
Fig. 37 Comparison of theoretical optical properties (curves in the graphs) with estimates based on reflectance measured with the fiberoptic system	62
Fig. 38 Optical properties of porcine tissues (average values of three animals).....	66
Fig. 39 Reflectance as a function of distance from center of illumination fiber (r).....	67
Fig. 40 Absorption coefficient of Hb and type I collagen.....	69
Fig. 41 Schematic of the fiber configuration ($0 < r_t \leq r_i$).....	74
Fig. 42 Schematic of the fiber configuration ($r_i < r_t \leq 2r_i$)	75
Fig. 43 The 4 mm diameter face of the fiberoptic probe	76
Fig. 44 Optical properties for evaluation of Eq. 23 and Eq. 24	78
Fig. 45 Reflectance from condensed MC simulations versus reflectance from standard MC simulations	79
Fig. 46 Simulation speeds of (a) standard Monte Carlo (in minutes) and (b) condensed Monte Carlo (in seconds) models for an illumination-detection fiber with radius of 0.1 mm	80
Fig. 47 Average values of maximum penetration depth from condensed MC simulations versus the values from standard MC simulations	81
Fig. 48 Reflectance of the illumination-detection fiber and other detection fibers from condensed Monte Carlo simulations (hollow symbols) and standard Monte Carlo simulations (solid symbols) at different optical properties	83
Fig. 49 Reflectance from condensed Monte Carlo simulations versus reflectance from standard Monte Carlo simulations	84
Fig. 50 Contours of dimensionless reflectance from illumination-detection fibers with different radii.....	86
Fig. 51 Reflectance as a function of fiber radius	86
Fig. 52 Standard deviation of reflectance with trend line	89
Fig. 53 Optical properties of breast tissue from literature	90
Fig. 54 Reflectance spectra of adipose and malignant breast tissues from illumination-detection fibers.....	91
Fig. 55 Percentage change of reflectance of malignant breast tissue.....	92
Fig. 56 Percentage detection depth of as a function of maximum penetration depth	95
Fig. 57 Detection depth as a function of square root of center position of detection fibers	99
Fig. 58 Percentage detection depths of illumination-detection fibers with different sizes	102
Fig. 59 Cancer developed from superficial layer	105
Fig. 60 3-D simulation results of a 3-layer tissue	108
Fig. 61 Reflectance signal on top of a 3-layer tissue	108
Fig. 62 Diffuse reflectance as a function of radius in a 3-layer Monte Carlo simulation.....	109
Fig. 63 Transmittance as a function of radius in a 3-layer Monte Carlo simulation.....	109
Fig. 64 Baseline simulation and number of fundamental layers corresponding to each layer in a layered tissue	111
Fig. 65 Comparison of standard Monte Carlo results and scaling Monte Carlo results .	112

Fig. 66 Influence of top layer μ_a on reflectance	114
Fig. 67 Influence of top layer μ_s' on reflectance.....	115
Fig. 68 Influence of bottom layer μ_a on reflectance	116
Fig. 69 Influence of bottom layer μ_s' on reflectance	117
Fig. 70 Neural network results with different probe geometries	121

Chapter 1. INTRODUCTION

1.1 Overview

Cancer is any of various malignant neoplasms characterized by the proliferation of anaplastic cells that tend to invade surrounding tissue and metastasize to new body sites. Most cancers begin with abnormal cell growing to form a lump called tumor until the tumor is out of control and spread to other part of the body. The longer the tumor goes unnoticed, the smaller the chance that the cancer can be treated effectively. In the USA and other developed countries, 25% of all deaths come from cancer. The most fatal cancers for males include lung cancer, prostate cancer, colorectal cancer, and pancreatic cancer and those for females include lung cancer, breast cancer, colorectal cancer, ovarian cancer, and pancreatic cancer. ¹

Cancer is a preventable disease. Early detection of cancer is considered the best way to increase the chance for survival. For example, colorectal cancer is reported by the American Cancer Society to have a five-year survival rate is 92% if detected and treated at an early stage. The rate drops to 64% if the cancer spreads outside the colon to the lymph nodes. This number drops dramatically to 7% if the cancer has spread further to the liver or other organs. It is clear from these outcomes that early detection is essential to patient survival. Unfortunately, it is also reported that only 37% of colorectal cancer is currently found at an early stage. ² The five-year relative survival rate for cervical cancer is 92.2% when it is detected at a localized stage. The survival rate drops to only 16.5% when diagnosed with distant metastasis. ³

The visible inspection of a tissue such as skin has long been use to assess the tissue lesions of patients. This is probably the rudiment of modern optical diagnostics. Since visible inspection depends on the evaluator's skill and the evaluations by different

observers can be inconsistent, quantitative instrumental methods are necessary to offer a more objective means of diagnosis. The traditional method for cancer detection is by a surgical procedure which is painful and it takes time for the wound to heal. However, a new technique, *in vivo* optical spectroscopy which use light to detect tissues without moving them out of the body, is revolutionizing the way that cancer is diagnosed by facilitating the localization of biopsies or, eventually, eliminating their need altogether. This technique has great potential to provide rapid, accurate, minimally-invasive disease detections.⁴ When light interacts with a tissue, it could be absorbed, scattered out of the tissue, or emit fluorescence after absorbing excitation photons. All these interactions can provide useful and critical information about chromospheres, physiological functions and structure of the tissue.

Many researchers are focusing on the research, development and commercialization of *in vivo* technologies which aid in the early detection and localization of cancer and several companies have commercialized their own products. Xillix® Technologies Corp. (<http://www.xillix.com>) developed innovative fluorescence endoscopy systems including Xillix LIFE-Lung™, Xillix LIFE II™, and Onco-LIFE™ which allow physicians to see very small, early stage cancer and even subtle pre-cancerous lesions especially in lung. MediSpectra (<http://www.medispectra.com>) has commercialized its LUMA® Cervical Imaging System to evaluate the cervix as an aid in the early detection of high-grade cervical cancer and its precursors. The LUMA® system scans tissue with a combination of fluorescence spectroscopy and white light diffuse reflectance spectroscopy to detect pre-cancerous cervical abnormalities that have the potential of becoming invasive cancer. TruScreen® by Polartechnics (<http://www.polartechnics.com.au>) is also designed to detect abnormalities of the cervix. The WavSTAT™ optical biopsy system by SpectraScience (<http://www.spectrascience.com>) is used to detect colorectal cancer by collecting the emitted fluorescent signals.

Most of these commercialized instruments mentioned work in the ultraviolet A (UVA) and visible (VIS) regions where fluorescence information of the tissue can be used in diagnosis. Despite these commercialized instruments, the optical properties (μ_a and μ_s) of tissues are minimally studied. Most research on determination of μ_a and μ_s has been carried out in the spectral regions from 600 to 1300 nm and has focused on low and moderate absorption coefficient values ⁵ because the absorption of water and chromophores such as hemoglobin, melanin, and nucleic acids is low in this spectral range. However, since spectral regions below 600nm are essential for *in vivo* fiberoptic diagnostics, especially for the fluorescence study, improved understanding of the μ_a and μ_s values of tissues is crucial for these clinical instruments to achieve their full potential.

Spectroscopy signals from a tissue can be detected as an image or a spectrum and the signals can be reflectance or fluorescence. While imaging can visualize lesions directly, a spectrum can provide a quantitative understanding on optical properties of the tissue by showing the spatial or temporal distribution of the radiance. Some instruments - hyperspected imaging system - actually work as a hybrid form by producing a spectrum at each pixel in the image.

1.2 Overall objective

More than 85% of all cancers originate in the epithelia of mucosa tissues lining the internal surface of the human body.⁶ Reflectance spectroscopy has been demonstrated to be useful for providing biochemical and morphological information for minimally-invasive detection of cancer in these mucosa tissues, including cervix ⁷⁻⁹, esophagus ⁹⁻¹², colon ^{13, 14} *etc.* It has also been used for monitoring of tissue oxygenation ¹⁵⁻²⁴ and analytes such as bilirubin ²⁵⁻³⁰ and glucose ³¹⁻³⁵. Furthermore, reflectance-based approaches are critical for providing fundamental optical property data on biological tissues which can be used in disease diagnosis, disease treatment, theoretical models, or to enable extraction of intrinsic signals for disease diagnosis ³⁶⁻³⁹. These tasks can be

accomplished using imaging techniques or fiberoptic probes. Fiberoptic based optical systems are essential for *in vivo* tissue diagnosis since fiber probes can be easily coupled with endoscope.

Although the literature contains a wealth of data on tissue optical properties in the far visible (600-750 nm) and near-infrared range (750-1400 nm), there is a lack of information in the ultraviolet A (UVA) to short visible (VIS) range where μ_a and μ_s' may be high. Furthermore, there is a lack of established experimental and numerical approaches that are suitable for use in this spectral range. The data being available is from tissue samples that have been sectioned or frozen, which reduce their relevance to the *in vivo* condition.

The overall objective of my research is to improve quantitative understanding of the relationship between reflectance spectroscopy and optical properties of mucosal tissues and to obtain optical property data of these tissues from reflectance spectroscopy with a fiberoptic reflectance system. The ultimate goal of my research is to know optical properties of all relevant human mucosal tissues under *in vivo* condition.

1.3 Organization of the dissertation

My research includes construction, evaluation, and implementation of a fiberoptic-based reflectance spectroscopy system, light-tissue interaction modeling, neural network model development, probe geometry investigation and single- and multi-layer tissue study. This dissertation is organized into the following chapters. Chapter 2 provides some background information relevant to the research described in this dissertation, including absorption and scattering, tissue optical properties, principle of reflectance spectroscopy for diagnosis of pre-cancer, tissue-simulating phantoms, and two common spectroscopic techniques for measuring tissue optical properties. Chapter 3 through Chapter 5 are arranged in such a way that each chapter will finally become an independent journal paper (Chapter 3 has been published.⁴⁰ Chapter 4 is ready to submit

and chapter 5 is in preparation. These chapters are detailed in following paragraphs) Chapter 6 summarizes the whole research and recommends several directions for future study.

In Chapter 3, I provide theoretical and experimental evidence of the capability of my multi-wavelength fiberoptic reflectance system to yield accurate optical property measurements within the UVA-VIS wavelength range. The system was constructed, evaluated and implemented to determine internal tissue optical properties. Inverse modeling was performed with a neural network algorithm to estimate absorption coefficients (μ_a) and reduced scattering coefficients (μ_s') based on spatially-resolved reflectance distributions. The inverse models were calibrated with simulated reflectance datasets generated using a condensed Monte Carlo approach with μ_a up to 85 cm^{-1} and μ_s' up to 118 cm^{-1} , which covers most of the optical properties of mammalian tissues within the UVA–VIS wavelength range. After theoretical and experimental evaluations of the system, optical properties of porcine bladder, colon, esophagus, oral mucosa, and liver were measured at 325, 375, 405, 445 and 532 nm. These data provide evidence that as wavelengths decrease into the UVA, the dominant tissue chromophore shifts from hemoglobin to structural proteins such as collagen. This system provides a high level of accuracy over a wide range of optical properties, and should be particularly useful for *in situ* characterization of highly attenuating biological tissues in the UVA-VIS.

Based on the study of condensed Monte Carlo model in Chapter 3, I extended the model so that it could facilitate computation of large sets of reflectance data for single illumination-detection fiber (a fiber that both illuminates and detect the signal) probes in biological tissues in Chapter 4. The model was validated against results from a standard Monte Carlo model and implemented to perform four tasks involving large numbers of individual simulations. First, by performing simulations at a wide range of optical property combinations, I was able to characterize the effect of fiber diameter on the relationship between reflectance and tissue optical properties. Secondly, I simulated

reflectance over a range of wavelengths from 400 to 500 nm based on the optical properties of malignant and adipose breast tissues to elucidate the effect of fiber diameter on reflectance spectra. The third task involved evaluating the effect of adding an illumination-detection fiber to a linear array fiber probe for optical property determination. The implications of this approach for optimization of probe geometries are discussed. Finally, I developed a scaling equation to calculate the maximum penetration depth of a photon. Influence of optical properties, detection distance from the illumination point, and size of an illumination-detection fiber on detection depth were studied. My results show that this approach represents a powerful technique for rapid simulation of light-tissue interactions when combined with existing methods for condensed modeling with separated fiber geometries.

While Chapter 3 and Chapter 4 were focused on single-layer tissue, the two-layer tissue situation was investigated in Chapter 5. In order to elucidate light propagation mechanisms involved in optical spectroscopy devices, the optical properties of layered mucosal tissues at UVA and VIS wavelengths are needed. Previous approaches to measuring these data have typically been based on spatially-resolved reflectance. However, these approaches have limitations, some of which are not well understood. Therefore, the objectives of Chapter 5 were (1) to elucidate the relationship between spatially-resolved reflectance distributions and optical properties in two-layer tissue models and (2) to introduce and assess an unconstrained approach to optical property measurement. The first part of this study involved calculating reflectance from two-layer tissues for a wide variety of optical property combinations ($\mu_a= 1-22.5 \text{ cm}^{-1}$, $\mu_s'= 5-42.5 \text{ cm}^{-1}$) using a Monte Carlo scaling technique. In the second part, a neural network inverse model trained with the aforementioned results was evaluated using simulated reflectance data. The relationship between optical properties and reflectance provides fundamental insights into the strengths, weaknesses and potential limitations of strategies for optical property measurement based on spatially-resolved reflectance. The neural

network approach estimated optical property values with a degree of accuracy that depended on the probe geometry (5-, 6-, 10- and 11-fiber probes were simulated). The average error in μ_a determination ranged from 15 to 51% and average error for μ_s' ranged from 8 to 32%. While computationally expensive to develop, neural network models calibrated with simulation data may prove to be a highly effective approach for rapid, unconstrained estimation of the optical properties of two-layer tissues.

Chapter 2. BACKGROUND

This chapter provided some background information relevant to the research described in this dissertation, including interaction of light with tissue, significance of study of tissue optical properties, tissue-simulating phantoms, and two common spectroscopy techniques for measuring tissue optical properties.

2.1 Interaction of light with tissue

2.1.1 Absorption and scattering – the basic

An atom can have many states which are defined by the arrangement of electrons in atomic orbits and these states have different energy levels. When an atom interacts with an incoming photon, the photon can be either absorbed or scattered depending on its energy ($E=h\nu$). If the photon's energy matches the energy difference between an excited state and current state of the atom, the atom will absorb the photon and jump to the excited state. The excitation energy will then either be rapidly transferred, via collisions, to random atomic motion or thermal energy, before a lower energy photon can be emitted⁴¹, or vice versa. The process of “taking up” a photon and consuming its energy is called absorption. The whole process from the hitting of a photon on an atom, to the transfer of the excitation energy to other energy, to the final discharge of another photon with lower energy is called inelastic scattering. Inelastic scattering is also the principle of fluorescence. In contrast to the inelastic scattering, if the atom radiates a photon with the same frequency as the incident one without transferring the excitation energy to other energy, the whole process is called elastic scattering or coherent scattering. In the elastic scattering process, the energy (and therefore the wavelength) of an incident photon is conserved and only its direction is changed. To be precise, scattering is seldom complete elastic and absorption always goes with some degree of scattering. On a macroscopic

scale, however, treating them separately is often convenient especially for the theoretical study. We can think that “absorption” and “scattering” take place independently without any appreciable contribution from the other process.

The theory of absorption and scattering by an atom can be extended to a big molecule. Similar as an atom, a molecule also have many energetic states which are defined by the energy states of one or more atoms of the molecule or by the molecule’s modes of vibration and rotation. A large molecule’s energetic state can be looked as being packed on top of each of its small components such as different functional groups. Like atomic orbital, these energetic states are also quantized and have discrete energy levels. Light can be absorbed by a molecule through electronic transitions or vibrational transitions which will excite a molecule from a less energetic state to a more energetic one. Electronic transitions change the energetic state of a molecule by exciting its electrons to a higher energy level. Such transitions are relatively energetic and hence are often associated with absorption of ultraviolet, visible and near-infrared wavelengths. Vibrational transitions change the energetic state of a molecule by changing the ways of vibration and rotation of a molecule’s bonds. Such transitions are not as strong as electronic transitions and are hence associated with absorption of infrared wavelengths. Same as the atomic case, the excited states usually do not persist. They will revert back to lower energy states and emit photons. If the emitted photons have the same energy level as the exciting ones, this process is called elastic scattering. Otherwise, it is called inelastic scattering.

2.1.2 Tissue absorption

As shown in Fig. 1, when a photon enters a tissue, quite a large number of scattering events by cell constituents, tissue fibers, intercellular structures, organelles in cells and the interfaces between structural components will occur. Besides scattering, the photon can also be absorbed by chromophores such as water, hemoglobin, melanin, *etc.*

The photon will then be remitted from the tissue as diffuse reflectance, be totally absorbed inside the tissue or lose some energy becoming fluorescence signal. All of these signals carry useful biochemical and morphological information about the tissue.

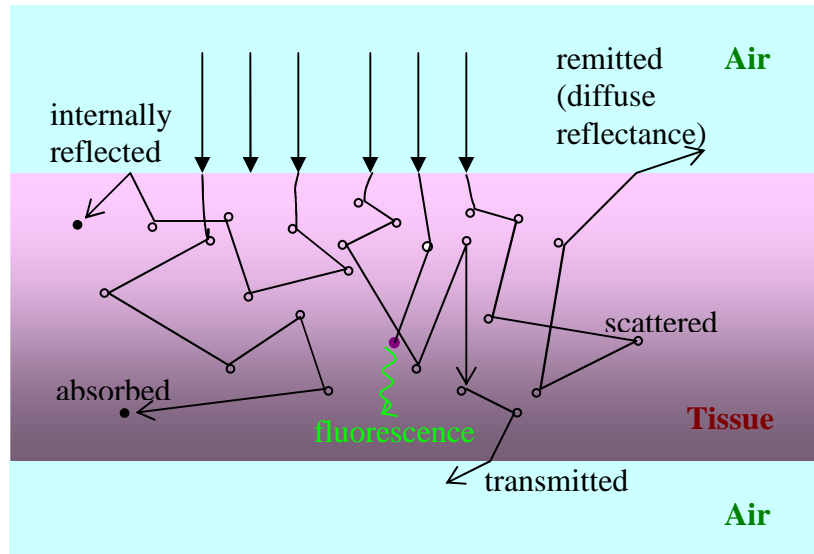


Fig. 1 Propagation of photons in a tissue

In a biological tissue, molecules that absorb light are called biological chromophores or biological absorbers. A biological chromophore can (1) absorb radiant energy in the far-infrared and microwave regions, converting it to rotational kinetic energy; (2) absorb infrared photons, transforming its energy into vibrational motion of the molecule; (3) absorb energy in the visible and ultraviolet regions through the mechanism of electron transitions, much like that of an atom. Biological chromophores that can absorb energy in the visible and ultraviolet regions generally have a string of double bonds whose pi-orbital electrons behave as a small antenna which can “receive” the electromagnetic wave of a passing photon. Porphyrins, including hemoglobin, vitamin B12, cytochrome C and P450, are a main group of biological chromophores.⁴² As the main composition of tissue, water is a main chromophore in the near-infrared wavelengths. Fig. 2 and Fig. 3 show the absorption spectra of hemoglobin and water respectively.

The parameter that describes the absorption property of tissue is the absorption coefficient, μ_a . When a photon propagates over infinitesimal distance ds , the probability for an absorption event is $\mu_a ds$. In other words, the mean free path for an absorption event is $1/\mu_a$. On a macro scale, the absorption coefficient is the fraction of light absorbed per unit distance in a participating medium. The absorption coefficient of a tissue varies strongly over the wavelength ranging from ultraviolet to visible light.

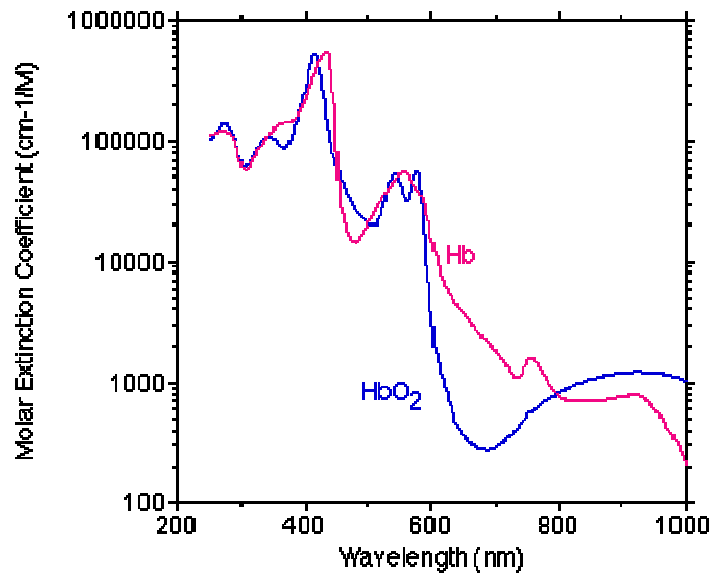


Fig. 2 Absorption coefficient of hemoglobin
(<http://omlc.ogi.edu/spectra/hemoglobin/summary.gif>)

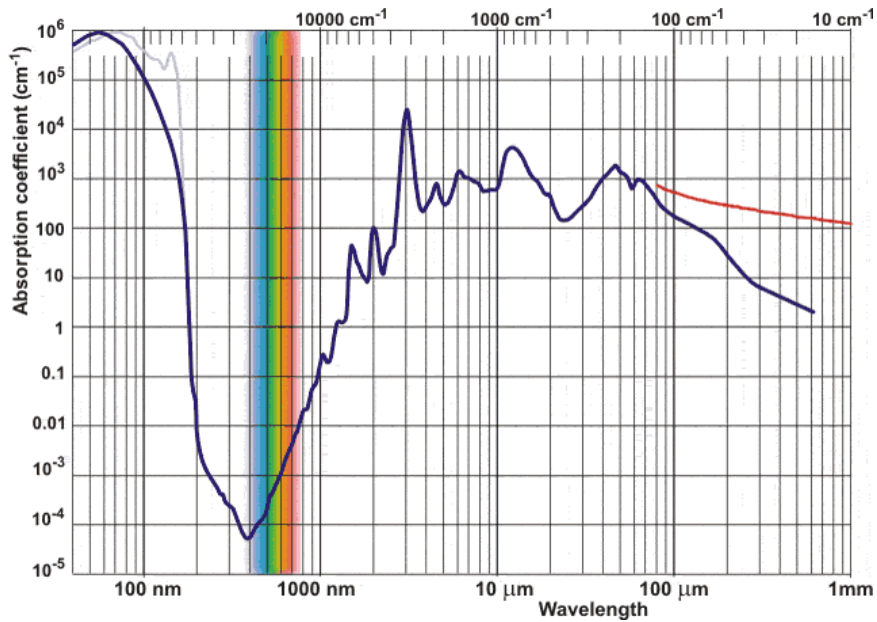


Fig. 3 Absorption coefficient of water
<http://www.lsbu.ac.uk/water/images/watopt.gif>

2.1.3 Tissue scattering

As a bulk turbid medium, the most pronounced event of light-tissue interaction is scattering. Light propagation in biological tissues is often dominated by scattering interactions. Extending from macromolecules to membranes to membrane aggregates to collagen fibers to cell organelles such as nuclei to cell, microstructures and ultrastructures of a tissue that can scatter light are called biological scatterers. Structures with size matching light wavelength scatter the light most strongly.⁴² The turbidity or apparent nontransparency of tissue is caused by multiple scattering of light from these biological scatterers. Fig. 4 shows the sizes of some biological scatterers.

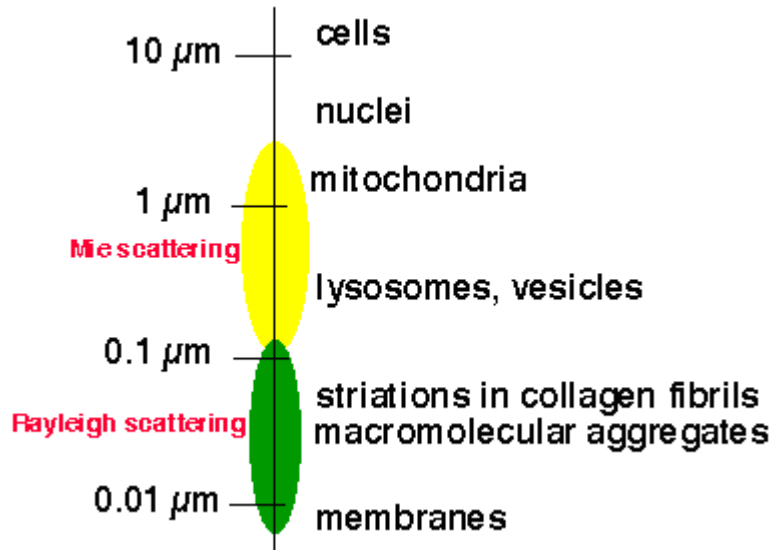


Fig. 4 Sizes of some biological scatterers
<http://omlc.ogi.edu/classroom/ece532/class3/scatterers.html>

Like scattering in any other medium, scattering in a tissue can be inelastic or elastic. In inelastic scattering, the incident and scattered photons are of different energy/frequencies. If the difference in energy generates acoustic photons, the scattering is called Brillouin scattering. If the difference in energy generates a vibrational excitation in the molecule, it is called Raman scattering. The inelastic scattering in biological tissues is weak.⁴³

The elastic scattering, in which the incident and scattered photons are of the same energy/frequencies, is strong in a tissue. There are two categories of elastic scattering. The first one is Rayleigh scattering, which happens when the size of the scatterer is smaller than the wavelength of light (*i.e.* less than about $\lambda/15$). In Rayleigh scattering, the intensity of the scattered light is proportional to $1/\lambda^4$ and therefore increases with ν^4 , where λ is wavelength and ν is frequency.⁴¹ The second one is Mie scattering, which happens when the scatterer size is comparable to λ . Mie scattering depends only weakly on λ with the intensity of the scattered light being proportional to $1/\lambda^{-X}$ ($0.4 \leq X \leq 0.5$)⁴³ and becomes independent of it (white light in, white light out) when the particle size exceed λ ⁴¹.

Mie theory, which is named after its developer German physicist Gustav Mie, is a complete analytical solution of Maxwell's equations for the scattering of electromagnetic radiation from spherical particles of any size. So Rayleigh scattering is the small-size limiting case of Mie scattering. The Mie theory reduces to Rayleigh scattering when the particle is much smaller than the wavelength. However, in most conditions, Mie theory is used in the intermediate size-to-wavelength ratio range where the Rayleigh is not valid. To accurately describe the scattering interactions of light with tissue, both Rayleigh scattering and Mie scattering are needed. Rayleigh scattering describes the scattering of light by tissue structures much smaller than λ including cellular components such as membranes and cell subcompartments, and extracellular components such as the banded ultrastructure of collagen fibrils. Mie scattering describes the scattering of light by various cellular structures like mitochondria and nuclei, and extracellular components like collagen fibers. Even though some biological scatterers are not necessarily spherical, their scattering behavior can still be modeled reasonably well by Mie theory.⁴⁴

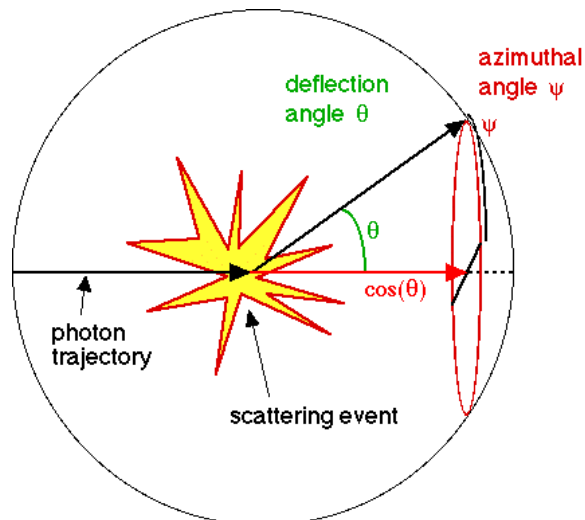


Fig. 5 A scattering event with a deflection angle and an azimuthal angle (<http://omlc.ogi.edu/classroom/ece532/class3/gdefinition.html>)

Scatter angles are important parameters to describe a scattering event. Fig. 5 shows the deflection angle (θ) and the azimuthal angle (Ψ) of a scattering event. Tissues are anisotropic and their optical properties are a function of the incident light direction. However, they are often assumed to be isotropic to simplify the conditions. For an isotropic medium, scattering depends only on the angle θ between the direction of incident light \hat{S} and the direction of reflected light \hat{S}' . The phase function is defined as the reflected intensity as a function of angle normalized by the intensity at normal incidence. It gives the intensity of reflected light from per unit intensity of incident light for a given angle of scattering event. It is also the single scattering probability density function $p(\hat{S}, \hat{S}')$ which can be written as

$$p(\hat{S}, \hat{S}') = p(\hat{S} \cdot \hat{S}') = p(\cos \theta) = p(v) \quad (1)$$

where $v = \cos \theta$. The integral of a density function around the incident point (solid angle of 4π steradian) is unit one.

$$\int_{4\pi} p(\hat{S}, \hat{S}') d\omega' = 2\pi \int_{-1}^1 p(v) dv = 1 \quad (2)$$

Therefore, for an isotropic scattering event

$$p(v) = \frac{1}{4\pi} \quad (3)$$

Unfortunately, light scattering in a tissue is far from isotropic. Therefore, the anisotropy factor (g) which is the average cosine value of the angle between the incident light and the reflected light is defined to describe the direction property of scattered light. The anisotropy factor g has a value between -1 and 1. A value of -1 indicates total backward scattering and a value of 1 indicates total forward scattering. Isotropic scattering means $g=0$. The anisotropy factor of a tissue, which is a combination number from both Rayleigh scattering and Mie scattering ranges from 0.3 to 0.98, but quite often it is around 0.9 in the visible spectrum.⁴⁵ The g value of Rayleigh scattering is around zero. While the g value of Mie scattering is near one.

Fig. 6 shows the phase function of a Rayleigh scattering in air calculated from a web site (http://omlc.org.edu/calc/mie_calc.html). It describes the angular distribution of 375 nm light scattered by a 10 nm diameter sphere with reflective index of 1.5. Light is incident from the left with the sphere located at the center of the linear polar plot. The green and blue curves demonstrate the situations of perpendicular and parallel light incident while the red curve demonstrated the situation of unpolarized natural light. From this figure, the forward and backward scattering is the same and the g value is 0.0014. However, the scattering is not isotropic. If the sphere diameter is increased to 400 nm, then the scattering become Mie scattering as shown in Fig. 7 which shows a strong forward scattering pattern.

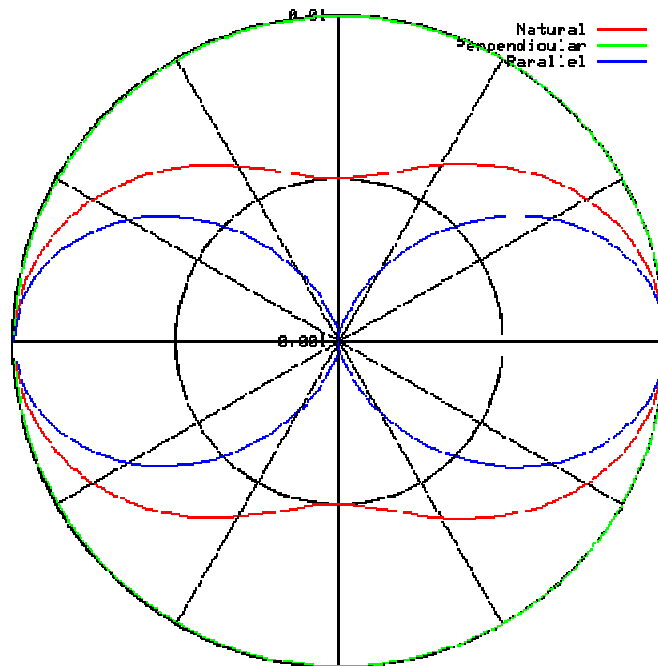


Fig. 6 The phase function of a Rayleigh scattering

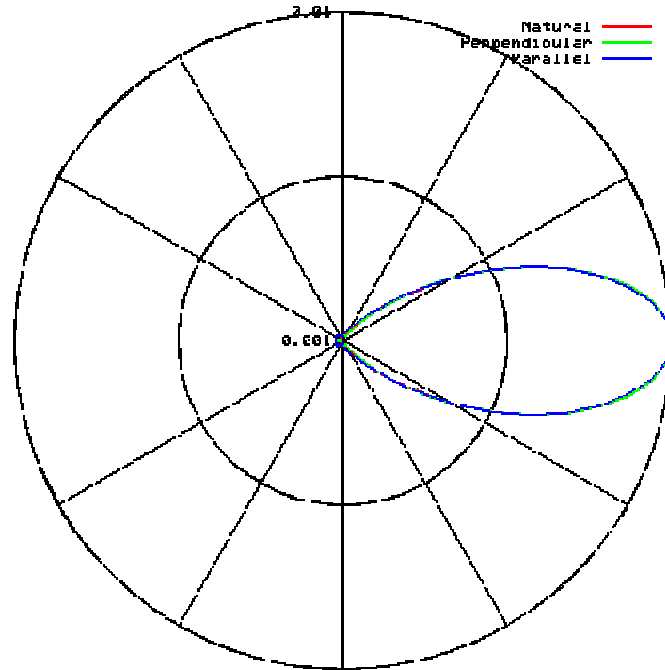


Fig. 7 The phase function of a Mie scattering

The parameter that describes the absorption property of tissues is the scattering coefficient, μ_s . When a photon propagates over infinitesimal distance ds , the probability for an scattering event is $\mu_s ds$. In other words, the mean free path for a scattering event is $1/\mu_s$. On a macro scale, the scattering coefficient is the fraction of light scattered per unit distance in a participating medium. The scattering coefficient usually decreases monotonically with increasing wavelength.

The scattering coefficient and the anisotropy factor are sometimes lumped to form a new parameter, reduced scattering coefficient ($\mu_s' = (1-g) \mu_s$). In a multiple scattering event in a tissue, an anisotropic scattering process with an anisotropy factor g and a scattering coefficient μ_s appears identical to an isotropic scattering process with an anisotropy factor zero and a scattering coefficient μ_s' . That means a photon will either take one big step of isotropic scattering (anisotropy factor 0) with mean free path $1/\mu_s'$ or $1/(1-g)$ smaller steps of anisotropic scattering (anisotropy factor g) with mean free path $1/\mu_s$ to get to the same position. This is called similarity principle, which is often used in

theoretical study. Fig. 8 shows the μ_s' of skin dermis, where the red line is tissue data, the green line comes from Mie theory based on collagen cylinders, the blue line is from Rayleigh scattering due to small-scale structure of collagen fibers, and the black dashed line is the combination of the green line and the blue line.

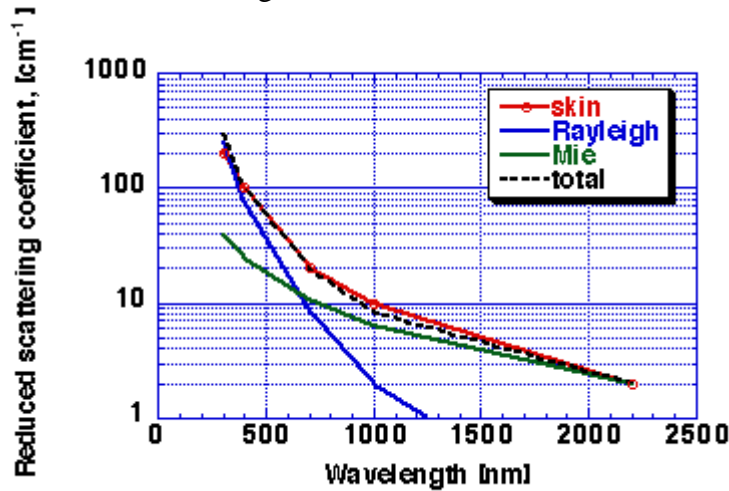


Fig. 8 μ_s' of dermis
<http://omlc.ogi.edu/news/jan98/skinoptics.html>

2.2 Significance of study of optical properties

The optical properties of a tissue mainly include μ_a , μ_s , g , and n (the index of refraction). While the values of g and n of a tissue usually do not change much and can be approximated by experience numbers, μ_a and μ_s change a lot with tissue type, structure, and health condition. Study of μ_a and μ_s of tissues can provide valuable information in several issues detailed below.

2.2.1 For disease diagnosis

As precancers develop, the morphology change of epithelial cells of mucosa tissue like cervix is characterized by increased concentration of chromatin, increased variation in nuclear size and shape, an increased nuclear to cytoplasmic ratio, roughing of the chromatin texture, the margination of nuclear chromatin, and increased metabolic activity. Accompanied with the development of intraepithelial neoplasia, stromal layer is

also altered with increased angiogenesis, decreased matrix density, and other alterations in the epithelial-stromal communication.^{6, 46-49} Dysplasia and carcinoma in the oral cavity had features including hyperproliferation and nuclear crowding of basal cells. The epithelium often showed features like epithelium thickening, loss of cell stratification, and enlargement of epithelial cell nuclei. Parts of the basement membrane and underlying collagen network (source of scattering) degraded and the volume of fraction of fibers decreases, facilitating tumor cell invasion and ultimately metastatic dissemination via the lymphatic and vascular systems.⁵⁰⁻⁵⁴ Milord *et al.* showed that urothelial neoplasms of the urinary bladder were characterized by the presence of numerous cells with large irregular and hyperchromatic nuclei that may be present either in the entire thickness of the epithelium or only a part of it⁵⁵. A study of esophagus indicated that cancer esophagus had higher density of cells with irregular cell size and shape and extreme heterogeneity. The nucleus cytoplasm ratio was also very irregular.⁵⁶ Biochemical changes often accompany the morphologic changes. Study shows that blood supply increased in dysplastic tissue, which is usually due to the increased microvessel density and the angiogenesis in the mucosal and submucosal tissues.⁵⁷⁻⁵⁹

As stated above, the tissue's biochemical and morphological characters will change when a tumor formed in a tissue, which in turn results in the change of optical properties. For a mucosa tissue, dysplastic changes include increased scattering from epithelial cells, decreased scattering from collagen fibers in the stroma, and increased absorption in stroma owing to increases in hemoglobin concentration.⁶⁰ The change of optical properties will then bring change of reflectance spectroscopy. Therefore, by extracting optical properties out of reflectance signal, we can diagnose disease quantitatively.

2.2.2 For disease treatment

Modeling light propagation in tissues to get the optical properties is essential for photochemical reaction in tissue such as in photodynamic therapy. The key dosimetry parameter for photodynamic therapy is the fluence rate $\phi(z)$ which is a function of depth z . For highly scattering tissue, the diffuse light in tissue decreases exponentially with depth according to the equation of $\phi(z) = A \exp(-\mu_{eff} z)$, where A is a constant and μ_{eff} is the effective attenuation coefficient with $\mu_{eff} = \sqrt{3\mu_a[\mu_a + \mu_s(1-g)]}$. Fluence rates lower than expected will not do the therapy job. On the other hand, fluence rates higher than expected produce a greater than expected photochemical reaction, rate of heat production, and temperature rise, which will in turn damage some health tissue. Therefore, accurate μ_a and μ_s values are essential for dosimetry in optical therapy.

2.2.3 For tissue monitoring

Reflectance spectroscopy together with the extracted optical properties can be applied for tissue monitoring, which overlaps with its function of disease diagnosis and treatment. It can be used for margin assessment during core needle biopsy⁶¹, monitoring tumor respond to therapy⁶²⁻⁶⁵, monitoring tissue oxygenation^{15-24, 66} and analytes such as bilirubin²⁵⁻³⁰ and glucose³¹⁻³⁵ in order to guide future health care.

2.2.4 For theoretical study

Optical properties from reflectance-based approaches are critical for providing fundamental optical property data on biological tissues which can be used in theoretical models or to enable extraction of intrinsic signals for disease diagnosis³⁶⁻³⁹. Furthermore, optical properties can be utilized for probe geometry optimization and accurate light-tissue interaction simulation^{8, 40, 67}, which in turn will facilitate the clinical detection and therapy.

2.3 Tissue-simulating phantoms

Mimicking the properties of human or animal tissues, the tissue-simulating phantoms play a crucial role in aiding on understanding of light-tissue interaction and on developing diagnostic imaging or spectroscopy systems and physical therapeutic interventions. Many tissue-simulating phantoms have been proposed in optical applications such as spectroscopy and imaging.⁶⁸⁻⁷⁰ In general, phantoms are used for several purposes, including: (1) calibrating and optimizing an instrument; (2) testing of stability and reproducibility of an instrument; (3) comparing performances between systems; (4) providing a qualitative means of testing mathematical models, simulations, and theories.⁷¹

To achieve these goals, an ideal phantom should have the following properties: (1) the optical properties of the phantom (μ_a , μ_s' , g and n) are similar to those of the tissue at specified wavelengths; (2) the optical properties of the phantom are adjustable to mimic different tissues. Molecules of specific interest can be incorporated to mimic those in a tissue; (3) The thermal, mechanical, chemical and surface properties of the phantom are similar to those of the tissue and stable over time and environmental conditions; (4) The regions in the phantom can be incorporated with different optical properties; (5) The phantom can be incorporated with Brownian motion or flow; (6) The phantom is inexpensive and easy to manufacture and transport.⁷¹ A phantom having above properties can be used for any application. However, no single tissue phantom possesses all these properties. In real application, only some of these properties are important and the others can be neglected. For example, if one wants to calibrate the instrument, the accurate optical properties are most important and the other requirements are of low priority.

2.3.1 Phantom composition

The basic compositions in a phantom include matrix materials, scatterers and absorbers. The matrix materials are typically water, hydrogels (gelatin⁷², collagen⁷³,

agar⁷⁴, polyacrylamide⁷⁵⁻⁷⁸, poly(vinyl alcohol)⁷⁹⁻⁸⁰) and hard polymers (polyester^{81, 82}, epoxy⁸³, polyurethane⁸⁴). Some novel materials such as soft silicone^{85, 86} are also used. The water and hydrogel based phantoms are usually biologically compatible but can not be kept permanently. On the other hand, the polymer based phantoms are not biologically compatible but can be kept permanently. The fabrication of a water based phantom is the easiest, and that of a polymer based phantom is the most difficult. Since the polymer based phantoms can be preserved permanently, they are good for calibrating and optimizing the instrument.

The scatterers typically include lipid based emulsions (Intralipid^{74, 87}, milk⁸⁸), inorganic powders (titanium dioxide, aluminum oxide, gold⁸⁹) and polymer microspheres (polystyrene⁹⁰). The lipid based emulsions have biologically similar chemical and mechanical structure as the bilipid membrane of cells and organelles what is thought to cause scattering in a tissue. The disadvantage of such scatterers is that they are not as stable as other scatterers. The inorganic powders are the most common choice for scatterers because of their wide availability and high scattering coefficients. They can be obtained in well-controlled spherical formulations. Titanium dioxide and aluminum oxide are two commonly used inorganic scatterers. A primary difference between them is the maximum attainable value for the anisotropy factor. Firbank and Depty reported that the anisotropy factor of titanium dioxide is limited to 0.7, whereas the anisotropy factor of aluminum oxide can reach 0.97 in polyester resin.⁶⁹ The main downsides of the inorganic scatterers are that they subside in suspension in most media due to their high density and that they are not exactly representative of tissue scattering spectra. Polymer microspheres are also common choices as scatterers, with polystyrene microspheres being the most popular. From a scientific perspective, polystyrene microspheres are excellent for a standard phantom because they are produced with good quality control over the size and index of reflection. Thus, Mie theory can accurately predict the scattering coefficient of the phantom with polystyrene microspheres as scatterers. Previous studies show that

polystyrene microspheres are less fluorescent and less absorbing compared with other microspheres.⁹¹ Furthermore, they can suspend in water for longer time because their specific density, which ranges from 1.04 to 1.09, is very close to that of water. The shortcoming of polystyrene microspheres is that they are expensive.

The choice for absorbers varies widely from blood, cells, or hemoglobin to molecular dyes and inks (black ink⁷⁴, Protoporphyrin IX⁹⁰, methylene blue⁹²). The absorbers from organisms provide realistic tissue spectra but cost much than the molecular dyes and inks. Besides, they are less stable.

The early studies in tissue phantoms were mainly focused on mimicking the reduced scattering coefficient and the absorption coefficient of a tissue at specific wavelength. In the past decade, phantoms that can mimic tissue optical properties in a wider wavelength range and that are made of biologically important molecules such as hemoglobin and melanin and biologically compatible materials such as collagen are of interest. Besides, the mass flow in phantoms is also attracting more attentions. Methods that image mass flow in tissue include Doppler shift measurements^{93, 94} and correlation analysis of speckle⁹⁵⁻⁹⁸.

2.3.2 Determination of phantom μ_a - Beer's law

Tissue phantoms with known values of μ_a and μ_s are essential to the study of tissue optics and calibration of optical instruments. The absorption coefficient of an absorber can be determined from the transmittance value or absorbance value of its solution by Beer's law. The law states that the quantity of light absorbed by a substance dissolved in a nonabsorbing solvent is directly proportional to the concentration of the substance and the path length of the light through the solution. The law is also referred to as the Beer-Lambert law or the Bouguer-Beer law. A mutation of Beer's law is shown as following equations.

$$T = \frac{I_1}{I_0} = e^{-\mu_a d} \quad (4)$$

$$A = -\log_{10} T = \mu_a \cdot d \cdot \log_{10} e \quad (5)$$

where I_0 is the intensity of incident light, I_1 the intensity of the transmitted light, T the transmittance, A the absorbance, and d the path length. From above equations, the absorption coefficient can be calculated as

$$\mu_a = (A \cdot \ln 10) / d \quad (6)$$

or
$$\mu_a = -\ln T / d \quad (7)$$

From Beer's law, the absorbance is proportional to the concentration of absorber, so is the absorption coefficient. Therefore, the absorption coefficient of an absorber at desired wavelength can be calculated from the absorbance measured by a spectrophotometer. When light irradiate on the surface of a media with an absorption coefficient μ_a , the light intensity decrease exponentially with depth as shown in Fig. 9.

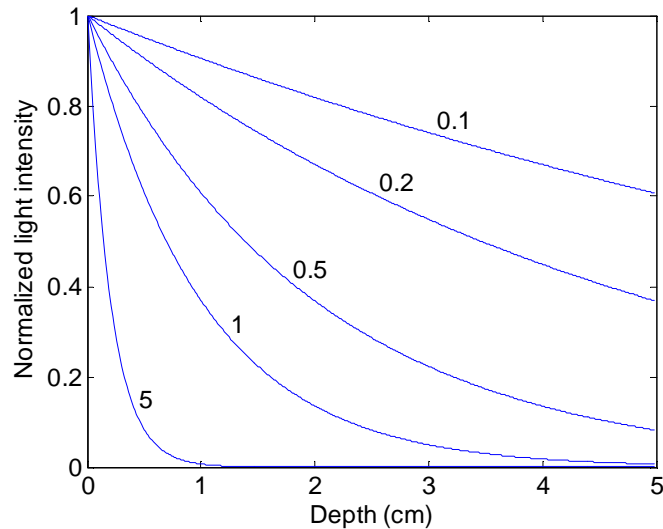


Fig. 9 Light intensity as a function of depth (cm) in media with different μ_a (cm^{-1})

Several sources can cause errors of the Beer's law. The law is accurate only for a dilute solution. Deviations from the law occur in concentrated solutions due to electrostatic interactions between solute molecules and changes in refractive index at high solute concentration. The linear-range concentration must be determined experimentally.

Scattering of light due to particulates in the sample and fluorescence/phosphorescence of the sample can also cause error.

2.3.3 Determination of phantom μ_s - Mie theory

Mie theory, which is named after its developer German physicist Gustav Mie, is very important in tissue phantom study. The μ_s of scatterers in tissue phantoms can be calculated by this theory. Mie theory is not a theory. Instead, it is a complete analytical solution of Maxwell's equations for the scattering of electromagnetic radiation. Therefore, it is called Mie solution sometimes. The theoretical scattering coefficient, absorption coefficient, and anisotropy factor of microspheres in a phantom can be accurately calculated with the Mie theory. In Mie theory, the imaginary index of refraction which indicates the amount of absorption loss when the electromagnetic wave propagates through the material is needed. Generally, the imaginary index of reflection is very small and neglected. Some on line Mie theory calculators are available (e.g. <http://www.lightscattering.de/MieCalc/> by Bernhard Michel, http://omlc.ogi.edu/calc/mie_calc.html by Scott Prahl).

The Mie theory dependent on the wavelength in vacuum, the sphere diameter, the refractive index of medium, the refractive index of microspheres (both real and imaginary), and the sphere density. The refractive indexes of the medium and microspheres are usually functions of wavelength and temperature.^{99 100-103} The refractive indexes of polystyrene¹⁰¹ and water¹⁰² are show in Fig. 10.

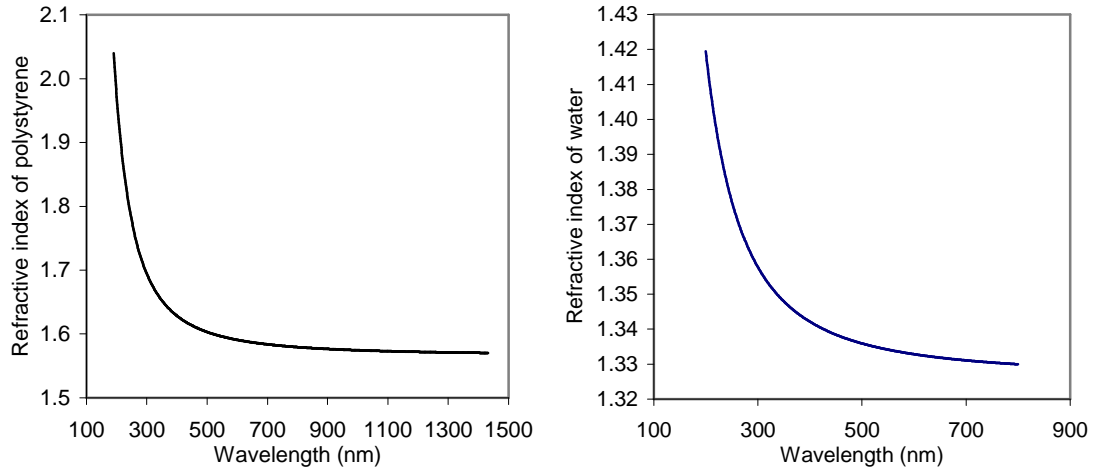


Fig. 10 Refractive indexes of polystyrene and water

2.4 Spectroscopy techniques for measuring tissue optical properties

Cancer detection with reflectance spectroscopy is based on the fact that tissue optical properties, such as absorption coefficient and scattering coefficient, change as tissue become dysplastic, which will in turn change the reflectance spectrum. By analyzing the reflectance spectrum, optical property change resulting from dysplastic change can be quantified.

The spectroscopy techniques for measuring tissue optical properties can be classified in different ways such as *in vitro* and *in vivo* or direct and indirect. *In vitro* techniques usually measure tissue sections while *in vivo* techniques measure tissues on living body. Direct techniques are generally performed *in vitro* and are independent of any model of light propagation in tissue. In direct method, the tissue section is thin enough that multiple photon scattering is negligible. The optical absorption and scattering properties of a tissue can be calculated directly from the fractional light absorbed or scattered by the sample.¹⁰⁴ Although the principle of the direct method is simple, it is extremely difficult to prepare the sample. The thickness of a sample for direct techniques should be much smaller than $1/\mu_s$, which is only several microns. Such a sample is difficult to make without altering the optical properties. In contrast, an indirect technique can be performed either *in vitro* or *in vivo* and it highly depends on the models. In an

indirect method, the parameters such as reflectance and transmittance of a bulk tissue are measured, from which the optical properties are deduced by applying one or more of the light propagation models.¹⁰⁵ Two prevalent spectroscopy techniques were discussed as following.

2.4.1 Spectrophotometer with an integrating sphere

One technique for optical property measurement is spectrophotometer with an integrating sphere. An integrating sphere, which is typically used with a light source and a detector for optical power, is an optical component consisting of a hollow spherical cavity. Its inner surface is coated with highly reflective materials such as barium sulfate (BaSO_4). Its spherical shape and highly reflective inner surface make it a diffuser which preserves power but destroys spatial information. Light rays incident on any point of the inner surface are distributed equally to all other points by multiple scattering reflections. Therefore, effects of the original direction of such light are minimized. An integrating sphere usually has several relatively small windows for entrance and exit of light or as a sample port. The sizes of these windows should be considered when calibrating the system.

Integrating spheres are often used to measure the reflectance or/and transmittance of a tissue. The measurements can be made in different ways. The incident light can be either collimated or diffuse and the light beam can be either one or two. The reflectance (R) and transmittance (T) of a tissue can be measured using one single integrating sphere in two steps or two combining integrating sphere in one step. Depending on the experiment design, either total or diffuse reflectance/transmittance can be measured as shown in Fig. 11.

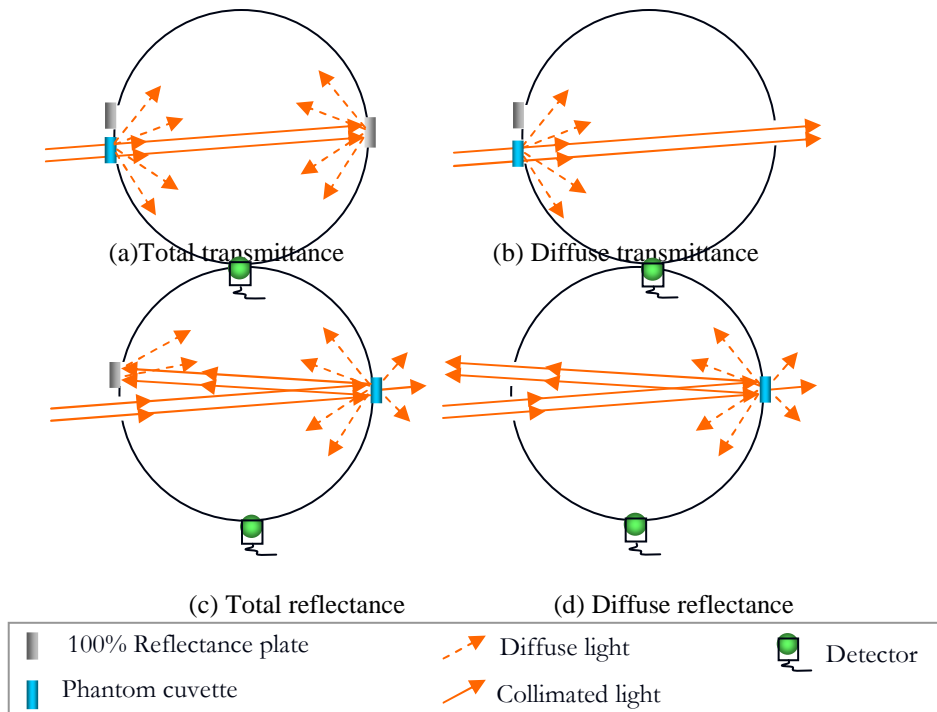


Fig. 11 Measurement of reflectance and transmittance with one integrating sphere

Integrating spheres can be used in different ways such as direct *in vitro*, indirect *in vitro*, or indirect *in vivo*. If the sample is thin enough (only several microns) that multiple photon scattering is negligible, it is a direct *in vitro* method. If the sample is optically thick tissue section, it is an indirect *in vitro* method. If the living tissue is directly attached to the sphere window, it is an indirect *in vivo* method. Since the sample for direct *in vitro* method is difficult to prepare and it is not convenient to attach the sphere to a living tissue, the indirect *in vitro* method is used mostly.

The inverse adding-doubling (IAD) method¹⁰⁶ is usually used to extract the optical properties from the reflectance and transmittance measured with an integrating sphere attached to a spectrophotometer. Therefore, the whole technique which includes the measurement of reflectance and transmittance with an integrating sphere and the extraction of optical properties from the measured reflectance and transmittance with the IAD method is sometimes also called the IAD method.

2.4.2 Fiberoptic-based spectroscopy techniques

Although the integrating sphere is widely used in optical studies, it is not convenient, especially for *in vivo* measurements. The introduction of optical fibers into the tissue optics area makes the real-time diagnosis possible. In recent years, significant progress has been made in the development of fiberoptic techniques for measuring tissue optical properties within the UVA-VIS wavelength range. These approaches make it possible to characterize internal tissues *in situ*, including via endoscopic delivery. They also enable measurements of intact *ex vivo* tissues, as opposed to prior *ex vivo* techniques which involved freezing, sectioning or homogenization, which may change the tissue optical properties. Amelink et al.¹⁰⁷ demonstrated the capability of differential path-length spectroscopy which consisted of two bifurcated optical fibers to determine the local optical properties of a tissue. Moffitt et al.¹⁰⁸ constructed a sized-fiber spectroscopy system consisting of two fibers with diameters of 200 and 600 μm and tested the system in the μ_a range of 0.1-2.0 cm^{-1} and μ_s' range of 5-50 cm^{-1} . Each fiber emitted and collected its own backscattered light. Sun *et al.*⁶⁷ developed a diffusion-theory-based inversion method for the extraction of tissue optical properties from *in vivo* spectral measurement ranging from 350 nm to 650 nm with a cylindrical optical fiber probe. The probe was composed of a central collection fiber surrounded by six hexagonally close-packed illumination fibers. The tissue optical properties used in their study were $\mu_s=40-100 \text{ cm}^{-1}$, $\mu_a=0.1-2.5 \text{ mm}^{-1}$, and $g=0.84$. Thueler *et al.*¹⁰⁹ described a fast spectroscopic system for superficial and local determination of the absorption and scattering properties of a tissue with a probe composed of eleven linearly arranged optical fibers, one for illumination and ten for detection. Palmer *et al.*¹¹⁰ identified an optimal probe geometry which consisted of a single illumination and two collection fibers. They found that μ_a ranging from 0 to 80 cm^{-1} and μ_s' ranging from 3 to 40 cm^{-1} could be extracted from reflectance with root-mean-square (RMS) errors of 0.30 cm^{-1} and 0.41 cm^{-1} respectively

using this probe geometry in conjunction with a neural network algorithm. This was only a purely theoretical study without any experiments.

In prior studies by our group, Pfefer *et al.*³⁹ developed a neural network algorithm for the extraction of μ_a and μ_s' from spatially resolved diffuse reflectance. Reflectance datasets for development of the neural network were generated by direct measurement of Intralipid-dye tissue phantoms at 675 nm and Monte Carlo simulation of light propagation with μ_a 1-25 cm^{-1} and μ_s' 5-25 cm^{-1} . The algorithm was able to extract μ_a and μ_s' of the phantoms to within RMS errors of ± 2 and ± 3 cm^{-1} , respectively. Sharma *et al.*¹¹¹ improved on this system by implementing an imaging spectrograph, high sensitivity CCD camera and in-line neutral density filters to maximize dynamic range and signal to noise ratio. With a similar algorithm the new system estimated μ_a and μ_s' values with average errors of 4.0% and 5.5%, respectively.

Fiberoptic-based systems for tissue optical property measurement often combine reflectance spectroscopy hardware with software for forward and inverse modeling. The hardware includes laser^{105, 108, 112, 113} or broadband^{36, 67, 107, 114} light sources, a probe with multiple optical fibers, one or more detectors, and a computer. The design of the probe – a bundle of illumination and detection fibers arranged in a well-defined geometry – is a key issue during system construction. Forward models can be categorized as analytical or numerical. An analytical model is usually an approximation of the radiative transport equation. Light propagation in a tissue can be described by an integrodifferential equation of radiative transport whose general analytic solution does not exist¹¹⁵. A diffusion approximation of radiative transport is often applied to obtain a closed-form analytical solution^{116, 117}. Analytical models are more elegant in principle since reflectance/transmittance can be expressed in a closed-form in terms of optical properties. However, the specific experimental conditions for which they apply are often simplified and the modeling equations are sometimes difficult to solve. Numerical models, however, enable incorporation of any source-tissue-detector geometry. Monte Carlo modeling,

which uses random numbers and statistics to find solutions to mathematical problems that cannot be easily solved, is a common numerical model for estimating light propagation in a tissue. The Monte Carlo method has long been recognized as a powerful tool to solve problems that are too complicated for an analytical solution. Since the first paper that introduced Monte Carlo simulation of laser-tissue interaction¹¹⁸, numerous improvements have been made¹¹⁹⁻¹²². Published works that provide a detailed description of the Monte Carlo approach as applied to light transport are available in the literature^{45, 123}. Because the Monte Carlo method is computationally intensive, various techniques have been developed to improve its efficiency^{124, 125}. The condensed Monte Carlo simulation introduced by Graaff *et al.*¹²⁵ is theoretically transparent and relatively easy to implement. Palmer and Ramanujam¹²⁶ extended Graaff *et al.*'s condensed Monte Carlo method from a ray source to a beam source by convolution.

By training an inverse model on the relationship between optical properties of a sample and its reflectance distribution, it is possible to develop a model that can readily calculate the optical properties of any sample based on the spatially-resolved reflectance distribution measured from that sample. Neural network is an empirical method that is commonly used to develop inverse models for optical property determination^{39, 111, 127}. While primarily used as an inverse model, it can also be used as a forward model to quickly determine reflectance distributions for arbitrary optical properties. Inverse neural network models for optical property determination require calibration with datasets that establish the relationship between sample optical properties and reflectance distribution. These datasets can come from phantom measurements³⁹, Monte Carlo simulations¹¹¹, or analytical models like diffusion theory¹²⁷.

Chapter 3. OPTICAL PROPERTY MEASUREMENT OF SINGLE-LAYER TISSUES WITH A FIBEROPTIC REFLECTANCE SYSTEM

3.1 Introduction

In order to quantitatively understand light-tissue interaction, accurate information on tissue optical properties is essential. To perform an *in vivo* measurement, minimally-invasive systems based on fiberoptic probe measurements have been developed¹⁰⁵. Previous fiberoptic-based approaches to optical property measurement have typically involved wavelengths from visible to near-infrared. Due to the low levels of attenuation in this spectral range, measuring reflectance was relatively easy compared to highly attenuating at short ultraviolet A (UVA) and visible (VIS) wavelengths. However, since most commercialized instruments for cancer detection work in UVA and VIS regions where the optical properties such as μ_a and μ_s of tissues are limited, further understanding of the μ_a and μ_s values of tissues in the UVA and VIS regions is crucial for the clinical instruments to achieve their full potential.

The focus in this investigation was on the *in vitro* determination of tissue optical properties, especially μ_a and μ_s' . A forward Monte Carlo simulation was run, followed by condensed Monte Carlo simulations to extend the datasets. With the datasets from condensed Monte Carlo simulations, inverse neural network models were developed. Then a fiberoptic reflectance system was constructed and calibrated with phantoms. A Matlab® (The MathWorks, Inc.) routine, which would call the inverse neural networks and was coupled into the LabView virtual instrument software, was applied to extract μ_a and μ_s' from the measured reflectance with the system. The whole system including the developed models was *in vitro* validated with phantoms and was finally used to measure porcine tissues *ex vivo*. Fig. 12 shows the flow chart of this investigation.

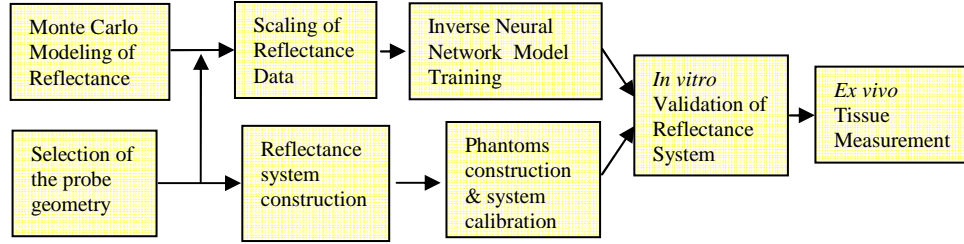


Fig. 12 Flow chart of the investigation

3.2 Monte Carlo modeling of light transport in single-layer tissues

Monte Carlo methods are based on the use of random numbers and probability statistics to find solutions to solve problems that are too complicated for a more classical approach. They are a class of nondeterministic algorithms being widely used. Because of the large number of calculations involved, Monte Carlo methods highly depend on computers. Since high-speed computers became widespread in the 1950s, published papers about Monte Carlo method explore. Monte Carlo methods have been used in many different fields and a great deal of theoretical as well as practical investigations have been undertaken. In general, most Monte Carlo models are used to simulate the propagation of electron, photon, and neutron.¹²⁸⁻¹³⁰ Gauvin *et al* developed a new Monte Carlo program to compute the X-ray spectra obtained with a scanning electron microscope.¹³¹ Similar simulations were also carried out by many other groups.¹³²⁻¹³⁶

Monte Carlo simulation of photon propagation simulates the “random walk” of photons in a medium. The movement of a photon from one absorption/scattering event to another is called one step. As shown in Fig. 13, the main parameters in a Monte Carlo simulation include step size s , deflection angle θ , and azimuthal angle Ψ . For every step, these parameters are chosen by statistically sampling the probability distribution as following equations, where ζ is a random number between [0,1] generated by a computer.⁴⁵

$$s = \frac{-\ln(\zeta)}{\mu_t} \quad (8)$$

$$\cos \theta = \frac{1}{2g} \left[1 + g^2 - \left(\frac{1-g^2}{1-g+2g\zeta} \right)^2 \right] \quad \text{for } g \neq 0 \quad (9)$$

$$\cos \theta = 2\zeta - 1 \quad \text{for } g=0 \quad (10)$$

$$\Psi = 2\pi\zeta \quad (11)$$

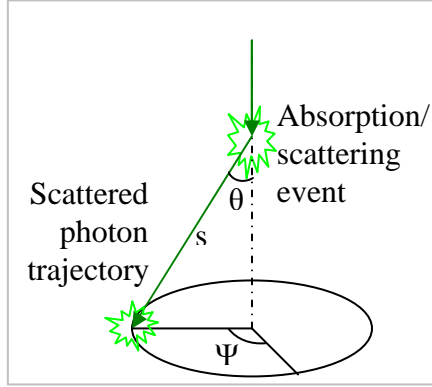


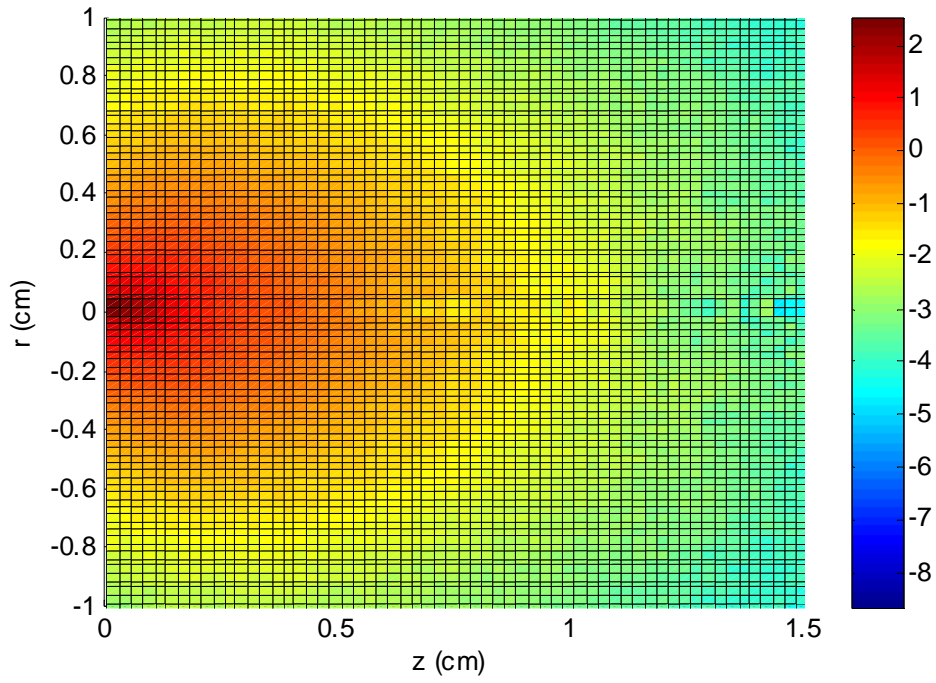
Fig. 13 Deflection of a photon by scattering event

Once a photon begins its travel in the media, its weight will be attenuated due to absorption by the media. If the photon weight is W , W is updated after each step according to the following equation.

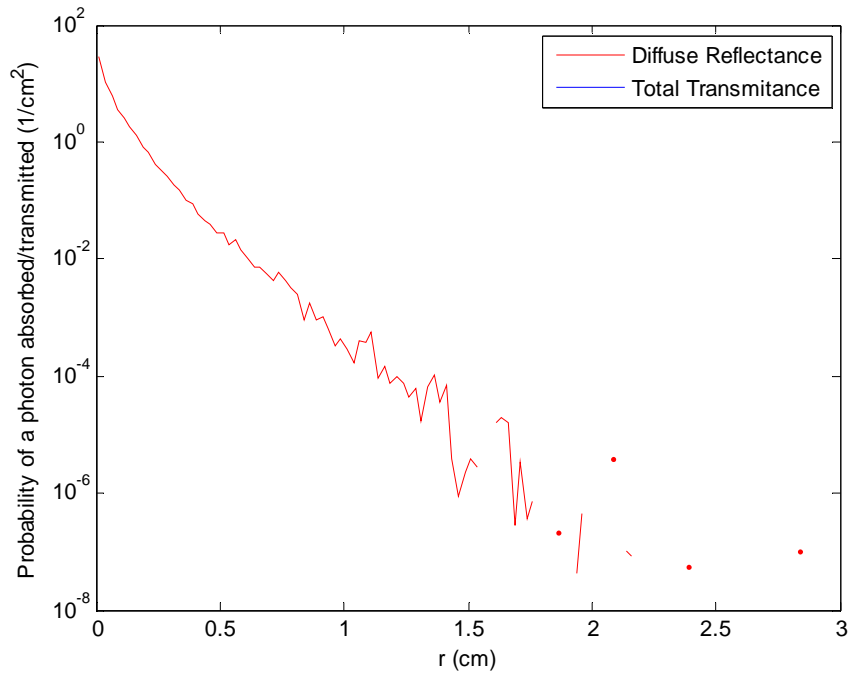
$$W \leftarrow W * (1 - \mu_a / \mu_t) \quad (12)$$

Of course, the internal reflectance or escape at the boundary as well as the termination of a photon should also be considered.⁴⁵ Although my focus is on the diffuse reflectance signals, the Monte Carlo simulation can also generate transmittance signals as well as internal fluence.

Based on above algorithm, a Matlab program was constructed to do the Monte Carlo simulations. Fig. 14 and Fig. 15 show results of two simulations. In each simulation, 50,000 photons were launched vertically from a ray source into a tissue with μ_a value of 0.5 cm^{-1} , μ_s' value of 20 cm^{-1} , g of 0.9, and n of 1.37. The Henyey-Greenstein phase function was used to mimic the scattering angle. The tissue thickness in Fig. 14 and Fig. 15 was 10 cm and 0.3 cm respectively.

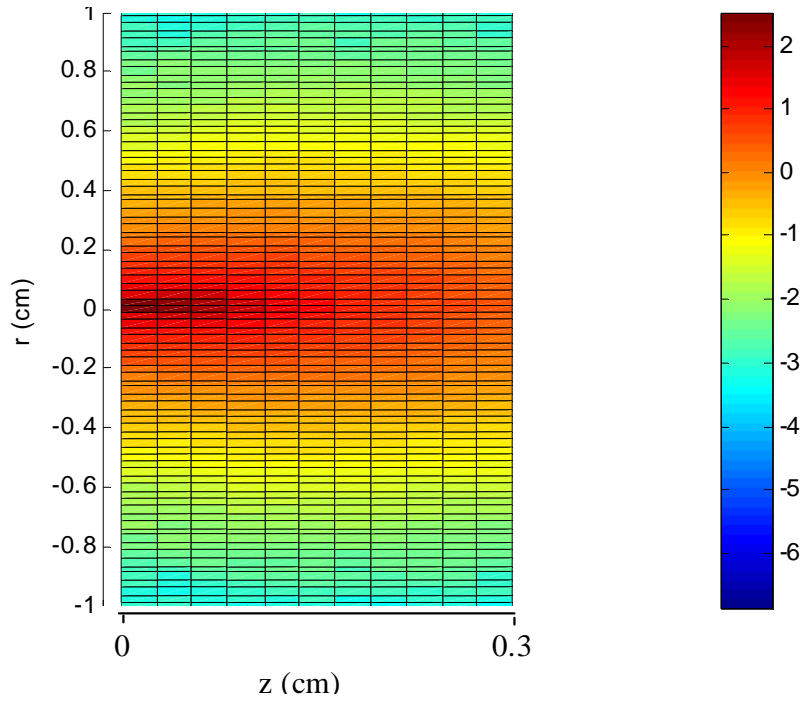


(a) Absorbance in the tissue

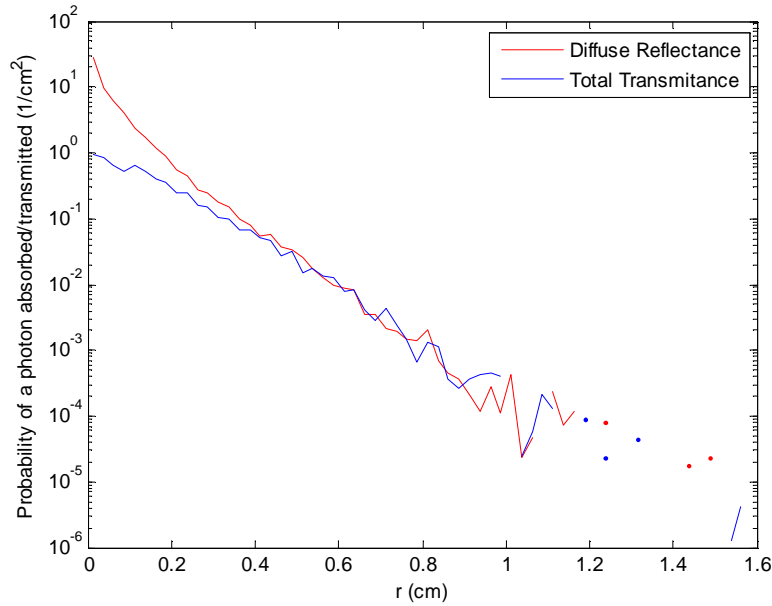


(b) Diffuse reflectance on the tissue surface

Fig. 14 Simulation results of a semi-infinite homogeneous tissue
 $(\mu_a=0.5 \text{ cm}^{-1}, \mu_s'=20 \text{ cm}^{-1}, g=0.9, n=1.37, \text{thickness } 10 \text{ cm})$



(a) Absorbance in the tissue



(b) Diffuse reflectance on the tissue surface

Fig. 15 Simulation results of a homogeneous bulk tissue
 $(\mu_a=0.5 \text{ cm}^{-1}, \mu_s'=20 \text{ cm}^{-1}, g=0.9, n=1.37, \text{thickness } 0.3 \text{ cm})$

To verify the accuracy of my Monte Carlo program, simulation results was compared with literature¹³⁷. Two simulations were run to obtain radially resolved

reflectance of two semi-infinite media. The two media had same μ_a (0.1 cm^{-1}) and μ_s' (10 cm^{-1}) but different g (0.9 and 0 respectively). The Henyey-Greenstein phase function was used to mimic the scattering angle. The reflective index of the fibers and media were 1. The incident light was a collimated pencil beam from which 500,000 photons were launched. All the escaped photons were detected. Fig. 16 shows my MC simulation results compared with results from literature. From this figure, both simulation curves overlap the curves from literature, which mean the Monte Carlo program is accurate.

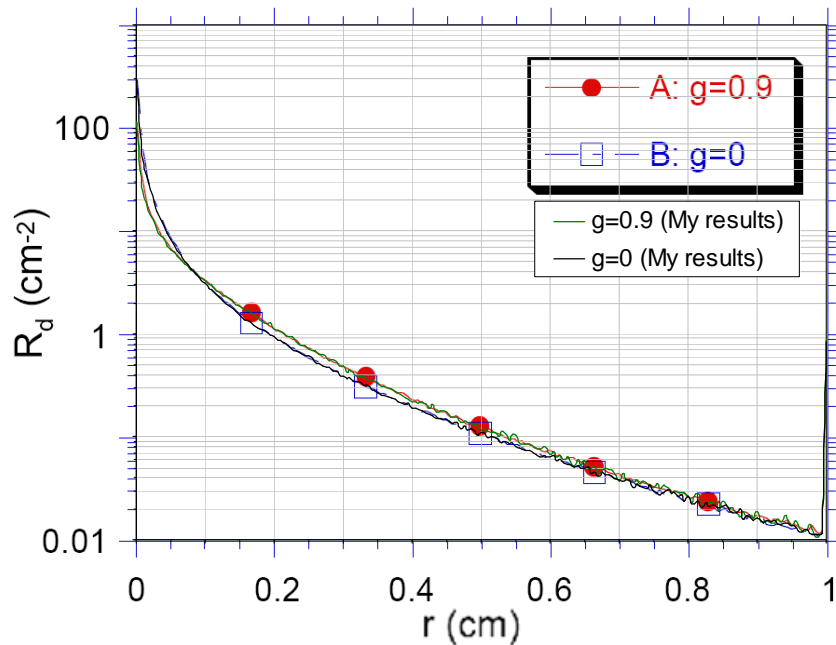


Fig. 16 Diffuse reflectance as a function of radius (r) - Comparison of MC simulation results with results from literature

3.3 Condensed Monte Carlo modeling of single-layer tissues

Because the Monte Carlo method is computationally intensive, various techniques have been developed to improve its efficiency^{124, 125}. The condensed Monte Carlo simulation introduced by Graaff *et al.*¹²⁵ is theoretically transparent and relatively easy to implement. Palmer and Ramanujam¹²⁶ extended Graaff *et al.*'s condensed Monte Carlo method from a ray source to a beam source by convolution. They derived a

convolution equation for the condition that the illumination fiber and the detection fiber are different ones.

Spatially resolved diffuse reflectance was calculated with a condensed Monte Carlo approach^{125, 126} mentioned above. Light propagation in a medium with absorption coefficient of $0 \text{ cm}^{-1}(\mu_{a,sim})$, scattering coefficient of $150 \text{ cm}^{-1} (\mu_{s,sim})$, and $g=0.9$ was simulated with a primary Monte Carlo model at first. It should be noted that non-zero $\mu_{a,sim}$ values can also be used in this simulation. The Henyey-Greenstein phase function was used to mimic the scattering angle. The index of refraction (n) of fibers was 1.45 and $n=1.37$ for tissues. The numerical aperture (NA) for both the illumination and collection fibers was 0.22. The incident light was a ray of “pencil beam” source from which 40,000,000 photons were launched in a uniform distribution over all angles within the cone specified by $NA=n \cdot \sin\theta$, where θ is the incident/acceptance angle measured from the normal to the tissue surface. For each detected photon which was governed by the acceptance angle, the number of interactions with scatterers (N), the distance from entrance to exit (r_{sim}), and the weight of the remitted photon (W_{sim}) were recorded. The value of W_{sim} was determined according to standard Monte Carlo approaches including weight reduction due to specular reflectance and absorption (in my case, the latter was minimal)^{45, 123}. In order to simulate a medium with new absorption coefficient ($\mu_{a,new}$) and scattering coefficient ($\mu_{s,new}$), scaling was performed for each photon to obtain the new distance from entrance to exit (r_{new}) and the new weight of the remitted photon (W_{new}) according to following equations (note that the following represent the general forms, whereas in my specific case, $\mu_{a,sim}$ is zero)^{125, 126}:

$$r_{new} = r_{sim} \cdot \left(\frac{\mu_{s,sim} + \mu_{a,sim}}{\mu_{s,new} + \mu_{a,new}} \right) \quad (13)$$

$$W_{new} = W_{sim} \cdot \left(\frac{\mu_{s,new}}{\mu_{s,new} + \mu_{a,new}} \cdot \frac{\mu_{s,sim} + \mu_{a,sim}}{\mu_{s,sim}} \right)^N \quad (14)$$

Since the probe’s illumination fiber was not a ray source, the following convolution equation¹²⁶ was used to calculate the probability (p) of a photon being collected by a

collection fiber with radius r_c after traveling a distance of r_{new} from an illumination fiber with radius r_i .

$$p = \frac{2}{\pi^2 r_i^2} \int_{\max(-r_i, s-r_{new}-r_c)}^{\min(r_i, s-r_{new}+r_c)} (s-x) \cdot \cos^{-1} \left[\frac{s^2 + (s-x)^2 - r_i^2}{2(s-x)s} \right] \cdot \cos^{-1} \left[\frac{r_{new}^2 + (s-x)^2 - r_c^2}{2(s-x)r_{new}} \right] \cdot dx \quad (15)$$

where s was the center to center distance between illumination fiber and detection fiber. This convolution equation was only used if $s \geq r_i+r_c$ and $s-r_i-r_c < r_{new} < s+r_i+r_c$, otherwise, $p=0$. Therefore, the collected weight ($W_{collect}$) of a photon by the detection fiber was calculated by the following equation.

$$W_{collect} = W_{new} \cdot p \quad (16)$$

The reflectance from a collection fiber was obtained by dividing the sum of total collected weight by the total number of launched photon.

By applying above condensed Monte Carlo technique, reflectance datasets within a wide range of optical properties in μ_a (0.1-85 cm^{-1}) and μ_s' (0.1-118 cm^{-1}) were generated. In total, 2805 datasets with even spacing of 2.5 cm^{-1} for both μ_a and μ_s' while $\mu_a > 30 \text{ cm}^{-1}$ and $\mu_s' > 5 \text{ cm}^{-1}$ and smaller spacing while $\mu_a < 30 \text{ cm}^{-1}$ or $\mu_s' < 5 \text{ cm}^{-1}$ were obtained, as well as 220 random datasets.

The geometry used in the condensed Monte Carlo simulations replicated the design of my fiberoptic probe. A diagram of the probe face is shown in Fig. 17. The probe contains linearly arranged fibers, a single illumination fiber and five detection fibers, spaced at consecutive center-to-center distances of 0.5 mm. The core diameter of each fiber is 0.2 mm with a NA of 0.22.

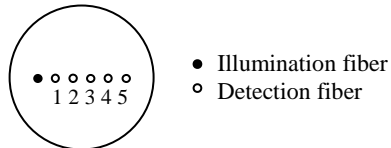
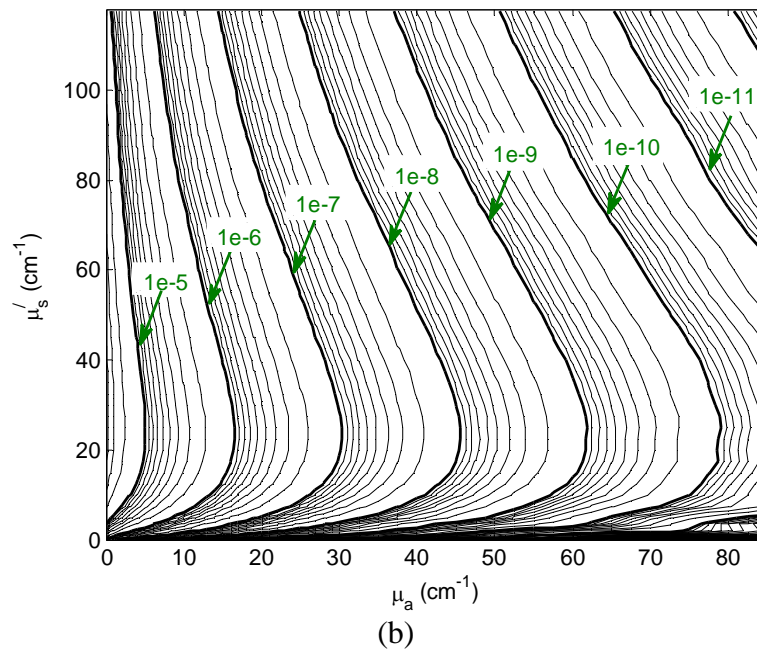
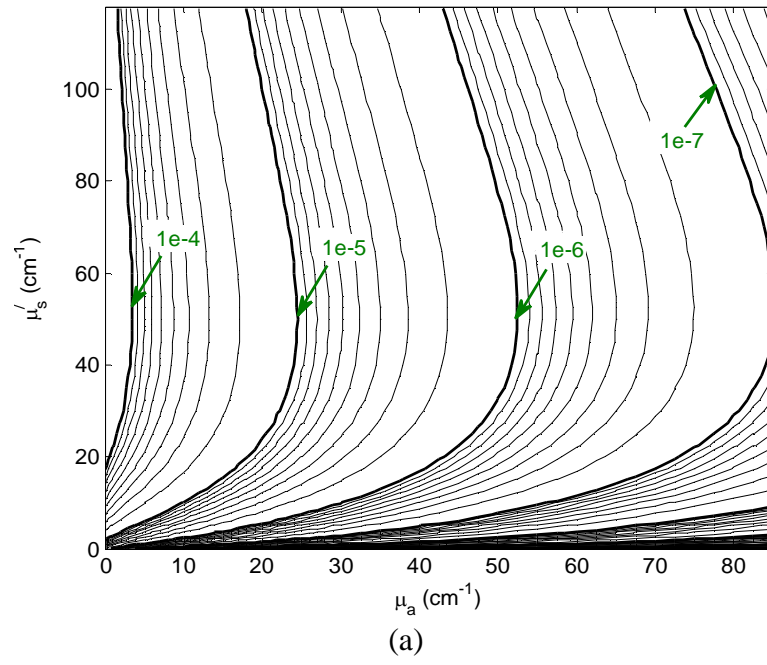
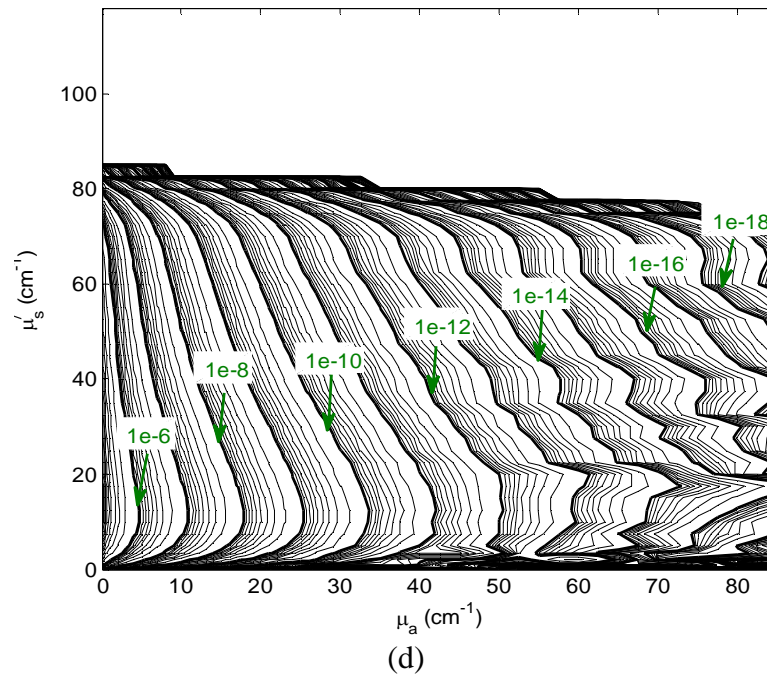
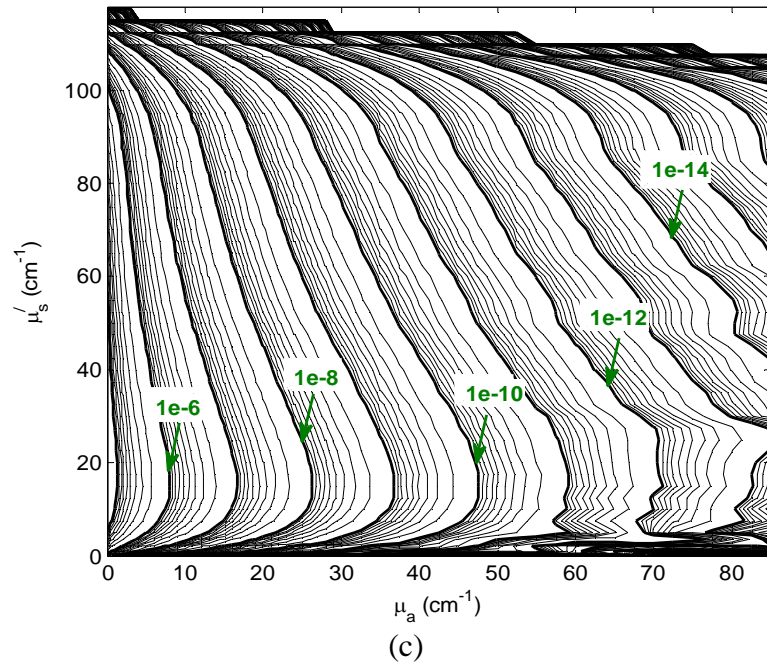


Fig. 17 The 4 mm diameter face of the fiberoptic probe

Fig. 18 shows the contour curves of dimensionless reflectance from five detection fibers from condensed Monte Carlo simulations. Reflectance per unit area can be obtained by dividing the dimensionless values by the cross section area of each detection fiber. These contour curves indicate that the sensitivity of reflectance to optical properties varies with μ_a and μ_s' . For each curve, its slope changes continuously. A steeper slope at a point means that the reflectance is less sensitive to μ_s' there. On the other hand, a shallower slope at a point means that the reflectance is less sensitive to μ_a . For example, reflectance is more sensitive to μ_s' than to μ_a when μ_s' is less than 5 cm^{-1} . This may affect the accuracy of neural networks in different μ_a and μ_s' ranges. For a fixed μ_a , reflectance increases to a maximum value and then decreases with increasing μ_s' . This trend seems to be related to prior findings that for a source-detector separation of 1.7 mm both the average photon path length and reflectance intensity are relatively insensitive to scattering properties (over a μ_s' range of 7.5 to 22 cm^{-1})¹³⁸. A similar insensitivity to scattering was also seen in reflectance data presented in my prior study³⁹. Although I do not show the results for source-detector separation of 1.7 mm here, a similar conclusion can still be obtained from Fig. 18 (c) which shows the reflectance for source-detector separation of 1.5 mm. From this graph, the contours are roughly vertical when μ_s' ranges from 7.5 to 22 cm^{-1} , which means the reflectance is insensitive to changes in μ_s' . Furthermore, it is possible to identify similar μ_s' range for other source-detector separation distance from similar contours in Fig. 18 (a), (b), (d) and (e).





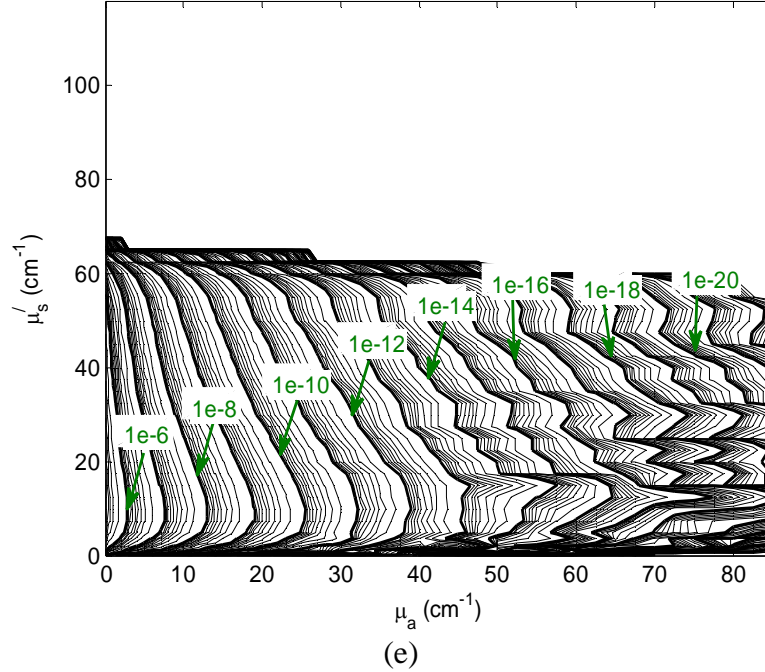


Fig. 18 Contours of dimensionless reflectance from each detection fiber with radius of 0.1 mm, where graphs a, b, c, d and e correspond to center-to-center distances of 0.5, 1.0, 1.5, 2.0 and 2.5 mm, respectively, between the illumination and collection fibers.

Overall, the plots for each fiber are similar. The contours of a nearer fiber resemble a close-up of those of a further fiber, except that the absolute values are higher. This shows the scaling theory of the condensed Monte Carlo method in another way. The irregular contour patterns at high μ_a and μ_s' for farther fibers originate from the fact that the quantity of launched photons is insufficient for convergence to an accurate solution for reflectance in these regions. Therefore, neural networks trained with these datasets may be prone to larger errors. For Fig. 18 (c), (d) and (e), it should be noted that the blank areas at the top of each graph indicate regions for which almost no photon were collected.

3.4 Development and evaluation of neural network models for single-layer tissues

Traditionally, neural network means a network or circuit of biological neurons. Mathematically, neural networks involve a network of simple processing elements (artificial neurons or commonly just neurons) which can exhibit complex global behavior, determined by the connections between the processing elements and element parameters.

A neural network can be trained by adjusting the values of the connections (weights) between neurons so that a particular input leads to a specific target output.

Reflectance datasets generated with the condensed Monte Carlo simulations were used to train and evaluate feed-forward back-propagation neural network models with the Neural Network Toolbox in Matlab[®]. The input vector for each network (sometimes referred to as an “input layer”) consisted of 2-5 reflectance values corresponding to the number of detection fibers used. The network also contained two hidden layers of seven neurons each with logarithmic sigmoid transfer functions, and an output layer of two neurons with linear transfer functions. The output vector consisted of the absorption and reduced scattering values. A Levenberg-Marquardt backpropagation training function was used. The number of neurons came from my optimization results. The reflectance datasets used for training included 2805 optical property combinations determined from the condensed Monte Carlo model. Two-thirds of these datasets were used for training and one-third of them were used for evaluation during training.

In order to identify appropriate model designs for performing optical property estimations, I evaluated the influence of detection fiber quantity (*i.e.*, the size of the input vector). This analysis was performed using simulation datasets both with and without the addition of artificially generated noise. A set of four neural network models, based on 2, 3, 4 and 5 detection fibers was generated and trained within the optical property range of 0.1-85 cm⁻¹ for μ_a and 0.1-118 cm⁻¹ for μ_s' .

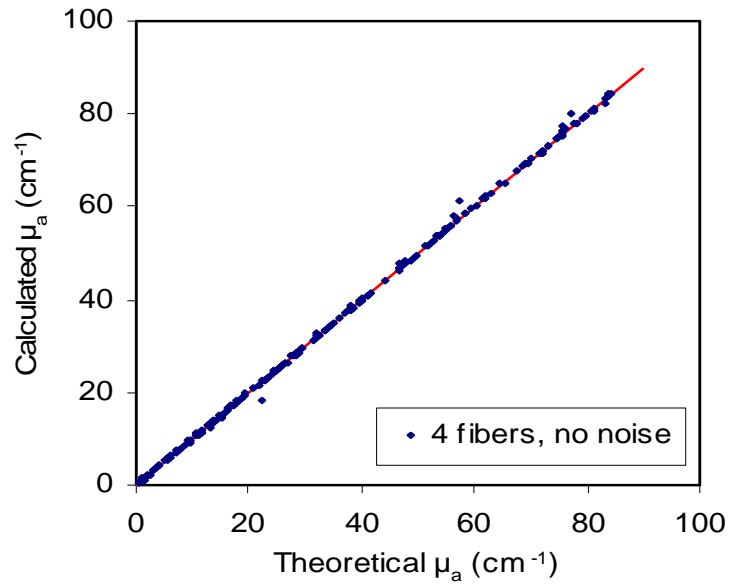
During initial measurements of highly attenuating tissues, it was found that under highly attenuating conditions (tissues, wavelengths) larger separation distance fibers did not collect sufficient signal. In order to assess the accuracy and robustness of my inverse modeling approach when fewer than five detection fibers were implemented, I performed the following theoretical analysis. Four neural networks based on 2, 3, 4, and 5 detection fibers were evaluated with the 220 random datasets generated with condensed Monte Carlo simulations. This evaluation was performed both without added noise and with 5%

random noise added to the reflectance values at all fibers. The noise level of 5% was based on measured variations in *ex vivo* tissues, which was likely dominated by spatial inhomogeneity. Table 1 summarizes the average values of absolute errors from the evaluations. The results for 5% noise are the average of three evaluations.

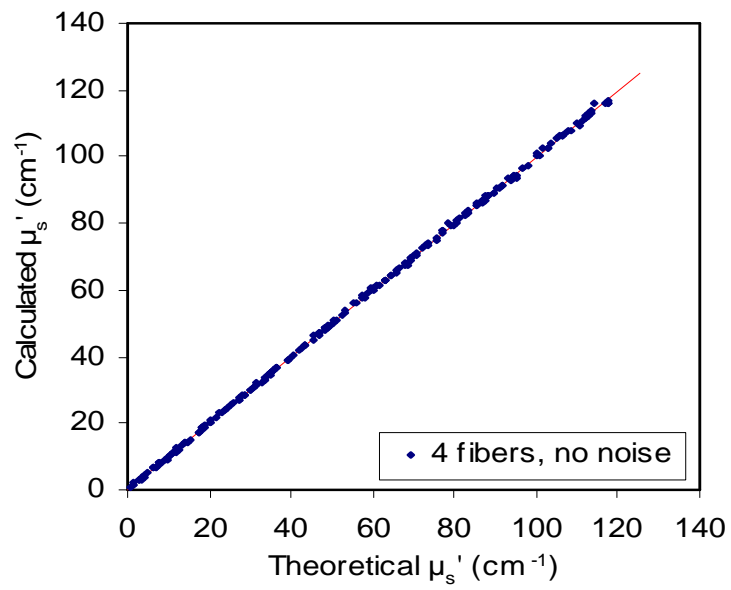
Table 1. Absolute errors of four neural networks (cm⁻¹)

No. of Fiber	2		3		4		5	
OP	μ_a	μ_s'	μ_a	μ_s'	μ_a	μ_s'	μ_a	μ_s'
No noise	0.32	0.41	0.39	0.38	0.22	0.28	0.24	0.25
5% noise	0.70	3.13	0.62	2.36	0.52	1.91	0.57	2.12

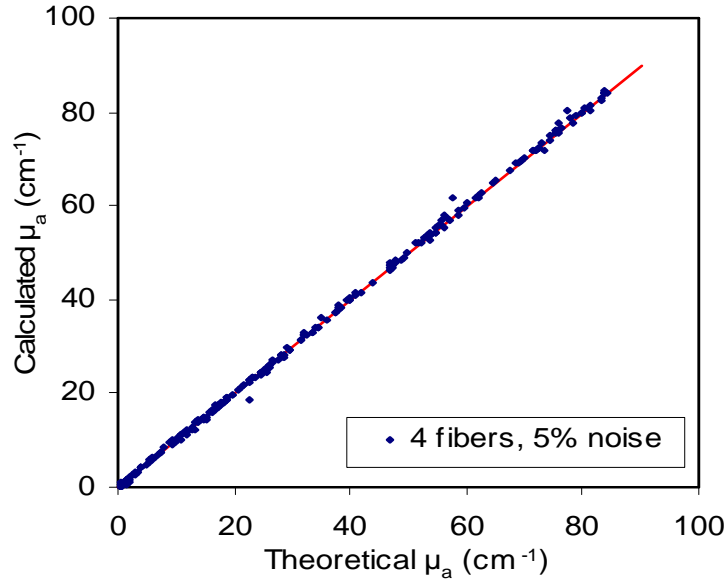
From Table 1, the absolute errors of optical properties from the neural networks decrease with an increasing number of detection fibers except for the five-fiber network which shows similar accuracy with the four-fiber network. This is likely because the greater noise in reflectance at high μ_a and μ_s' for fiber No.5 (Fig.4 (e)) render the reflectance from detection fiber No.5 of little use. In general, the errors of μ_s' are larger than the errors of μ_a , particularly for the 5% noise cases. Although noise increases error, the accuracy is still quite good in all cases and compares favorably with peer research to date¹¹⁰. Figure 5 shows the calculated μ_a and μ_s' from the neural network based on 4 detection fibers versus their theoretical values when no noise was added as well as 5% noise was added to reflectance. From Fig. 19 (d), the calculated values match the theoretical values well even with noise added to the reflectance.



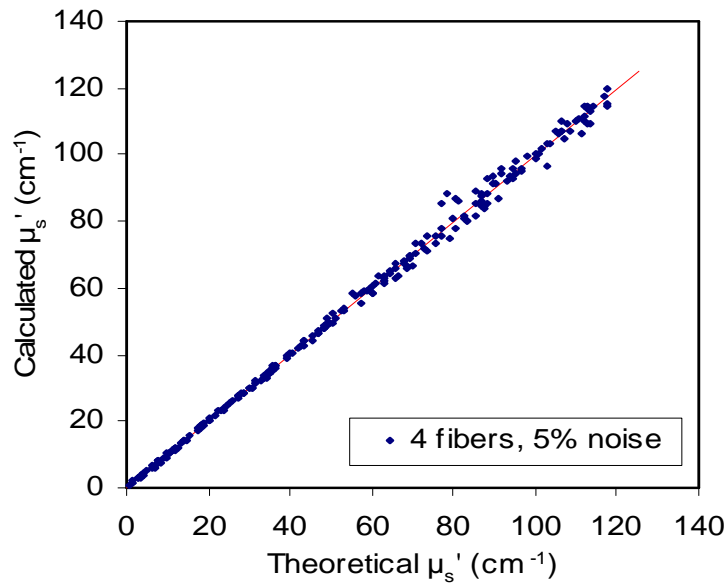
(a)



(b)



(c)

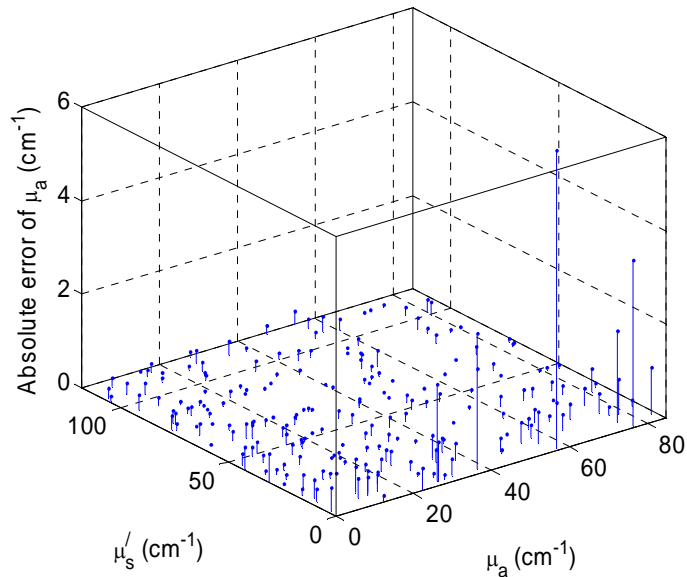


(d)

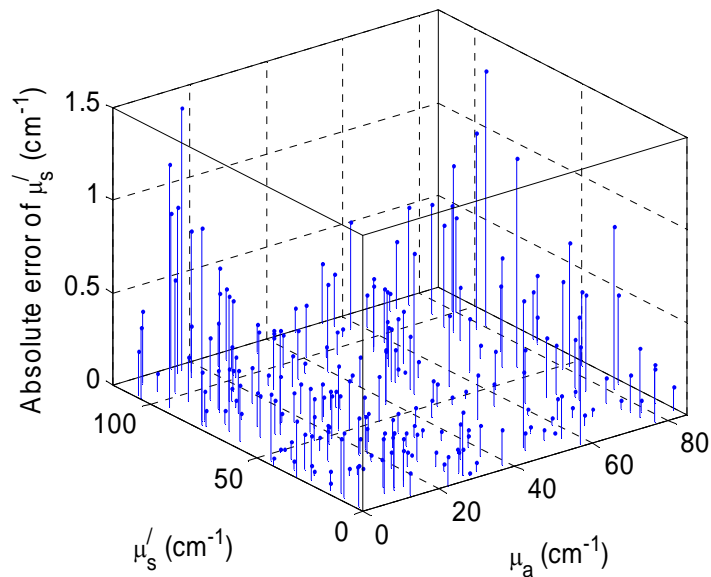
Fig. 19 The calculated μ_a and μ_s' from the neural network based on four detection fibers versus their theoretical values (straight lines indicate where the calculated values are equal to the theoretical values).

To study the sensitivity of neural networks at different optical property ranges, 3D plots of absolute errors (from the neural network with 4 detection fibers) of μ_a and μ_s' of each evaluation dataset are shown in Fig. 20. When no noise is added to the reflectance for evaluation, the error of μ_a is larger when μ_s' is less than 10 cm^{-1} (Fig. 20a). This

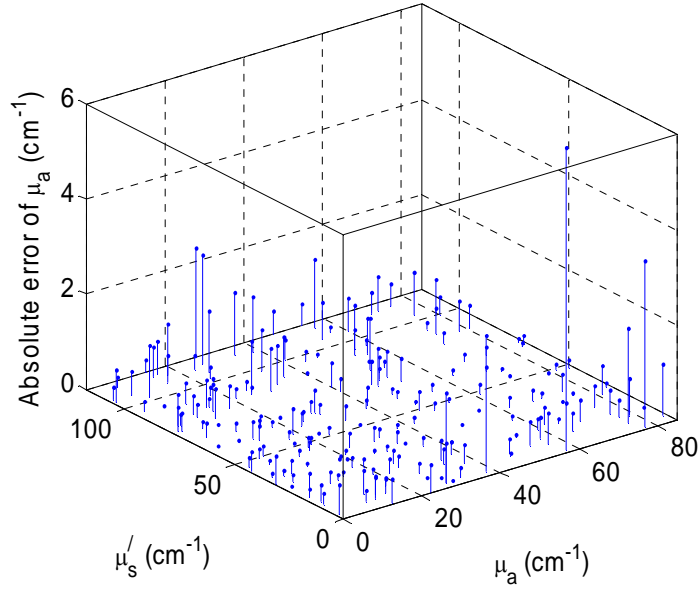
agrees with Fig. 18 which shows that reflectance is not sensitive to μ_a at low μ_s' . In general, μ_s' is rather accurate when no noise is added to the reflectance (Fig. 20b). When 5% noise is added to the reflectance for evaluation, the error of μ_a is larger at regions of lower- μ_a -higher- μ_s' and higher- μ_a -lower- μ_s' (Fig. 20c). From Fig. 20d, the errors of μ_s' are larger at lower- μ_a -higher- μ_s' region with 5% noise added. All these conclusions can also be obtained according to reflectance contours for each μ_a and μ_s' set (Fig. 18)



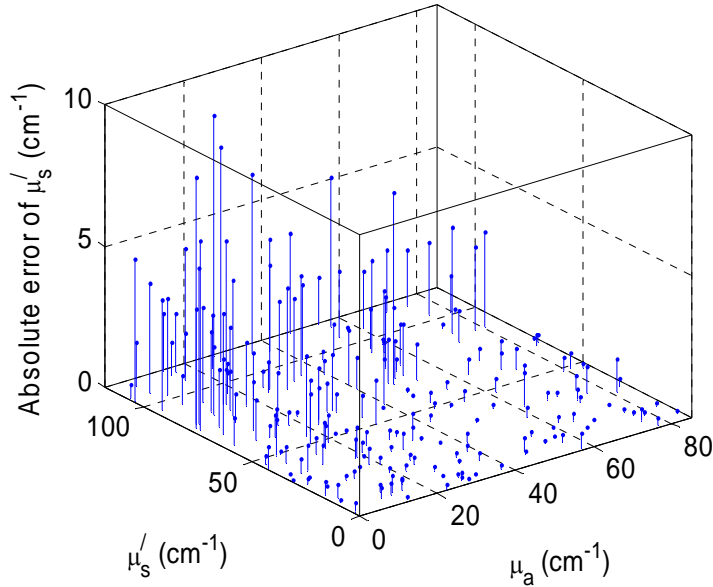
(a) No noise



(b) No noise



(c) 5% noise



(d) 5% noise

Fig. 20 Absolute errors of μ_a and μ_s' of each evaluation dataset from neural network based on 4 detection fibers

3.5 Construction of single-layer phantoms

During the developing of the fiberoptic diffuse reflectance system, phantoms with known optical properties are necessary for calibrating and optimizing the instrument

and providing a qualitative means of testing the parameters and assumptions made in mathematical models and simulations. Since aqueous suspension phantoms are easy to make, they are used as my single-layer phantoms.

Both nigrosine and hemoglobin A₀ (Ferrous stabilized human, Sigma H0267) were used as absorbers in phantoms. The former is cheaper and more stable while the later provides realistic tissue spectra. Their spectrums were measured with a spectrophotometer as shown in Fig. 21 and Fig. 23.

As observed from figures Fig. 22 and Fig. 24 of μ_a versus concentration, both nigrosine and hemoglobin show a linear relation between μ_a and concentrations. At wavelength 415 nm, the absorption coefficient has a minimum value for nigrosine while a peak value for hemoglobin. On average, the absorption coefficient of nigrosine is much higher than that of hemoglobin with wavelength ranges from 300 nm to 700 nm.

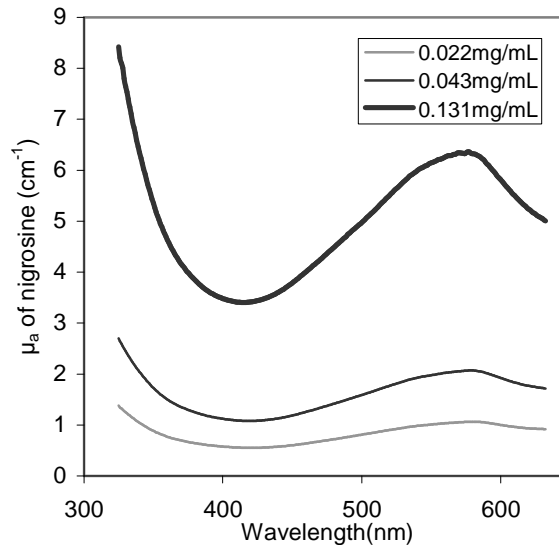


Fig. 21 μ_a of nigrosine as a function of wavelength at different concentrations

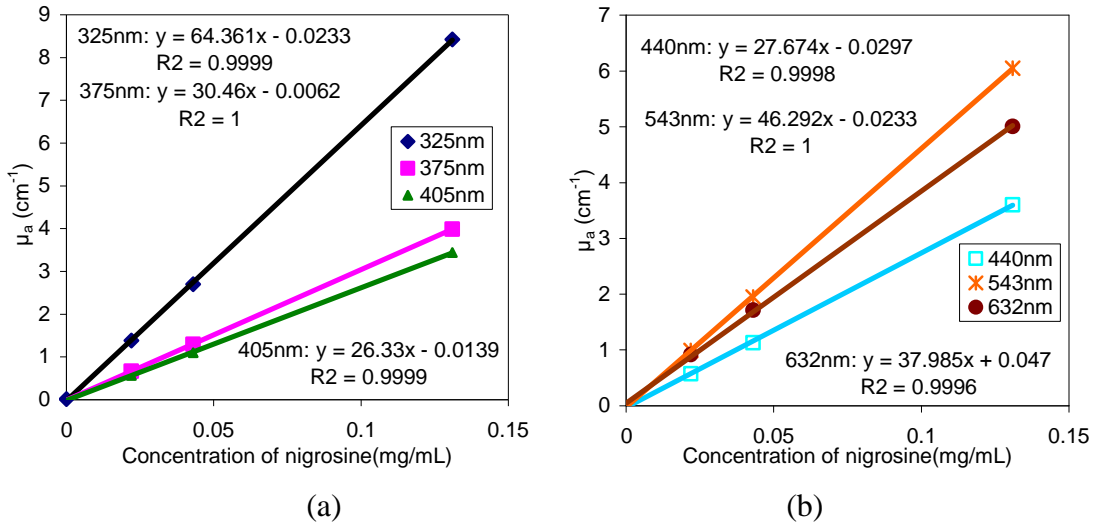


Fig. 22 μ_a of nigrosine as a function of concentration at different wavelengths

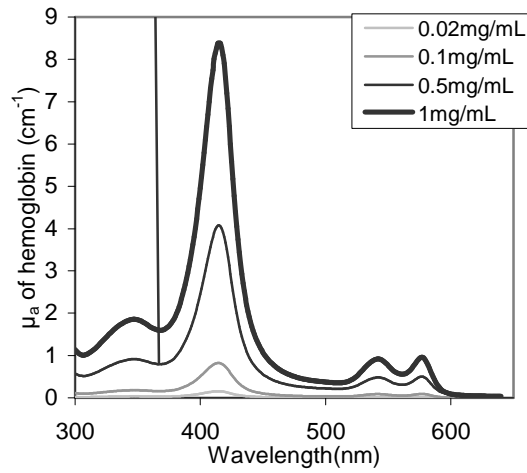


Fig. 23 μ_a of hemoglobin as a function of wavelength at different concentrations

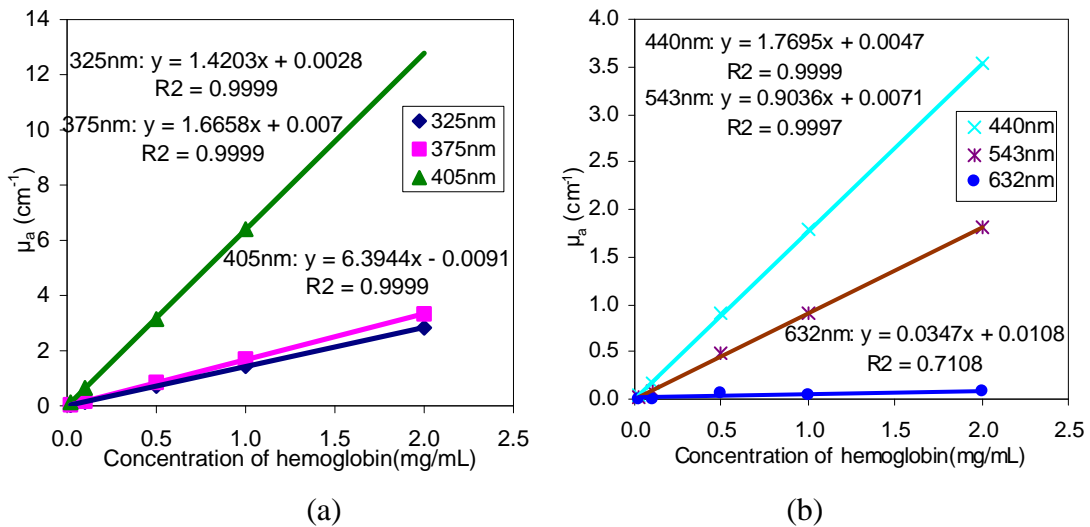


Fig. 24 μ_a of hemoglobin as a function of concentration at different wavelengths

As mentioned before, polystyrene microsphere is an excellent scatterer for a standard phantom because 1) it is produced with good quality control over the size and index of reflection, 2) it is less fluorescent and less absorbing compared with other microspheres, and 3) it has similar density with water. Therefore, polystyrene microsphere was chosen for phantom construction. The anisotropy factor of polystyrene microsphere is controlled by the sphere diameter, wavelength, refractive index of medium (water), and refractive index of sphere (polystyrene). Table 2 shows the refractive index of water and polystyrene from Fig. 10. The anisotropy factors of polystyrene microsphere with different diameters in water at different wavelengths are shown in Table 3.

Table 2. Refractive indexes of water and polystyrene at different wavelengths

Wavelength (nm)	325	375	405	445	543
Refractive index of water	1.3521	1.3446	1.3417	1.3387	1.3344
Refractive index of polystyrene	1.6706	1.6390	1.6266	1.6145	1.5968

Table 3. The anisotropy factors of polystyrene microspheres in water

Wavelength (nm)	325	375	405	445	543	
Diameter (μm)	1.0	0.8305	0.9011	0.9148	0.9207	0.9283
	1.5	0.8347	0.7870	0.8274	0.8485	0.8753
	2.0	0.8331	0.8676	0.8344	0.8275	0.8182
	2.5	0.8844	0.8452	0.8837	0.8761	0.8732
	3.0	0.8953	0.8634	0.8480	0.8454	0.8826

In order to best approximate biological tissues and satisfy the similarity relationship, a scatterer with an anisotropy factor bigger than 0.9 should be used.¹³⁹ Therefore, polystyrene microsphere with diameter of 1.0 μm was employed.

The scattering coefficient of a phantom can be calculated by Mie theory. There are many Mie theory programs available. The program used in my research was based on a Fortran language program for homogeneous sphere.¹⁴⁰ This program was initially translated and modified to a Matlab program by Anant Agrawal in our lab. Since the program could only calculate one group of input parameters every time, I then wrote another one to deal with the data input and output, which called the initial one as a

subroutine. The whole program can now input as many data as you want from an Excel worksheet simultaneously and output the results to another worksheet in the same file after calculation. Fig. 25 and (a) (b)

Fig. 26 show the results from these two Mie scattering programs at different wavelengths and sphere densities.

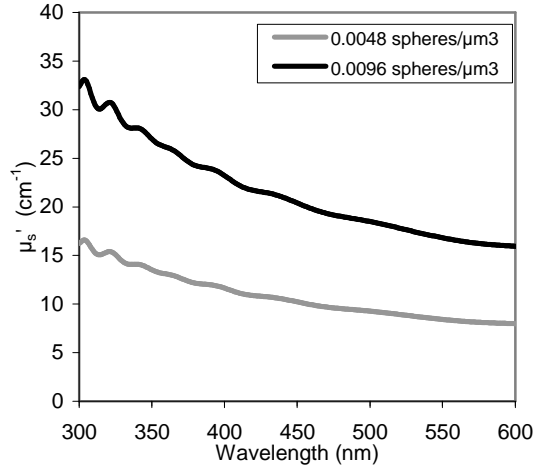
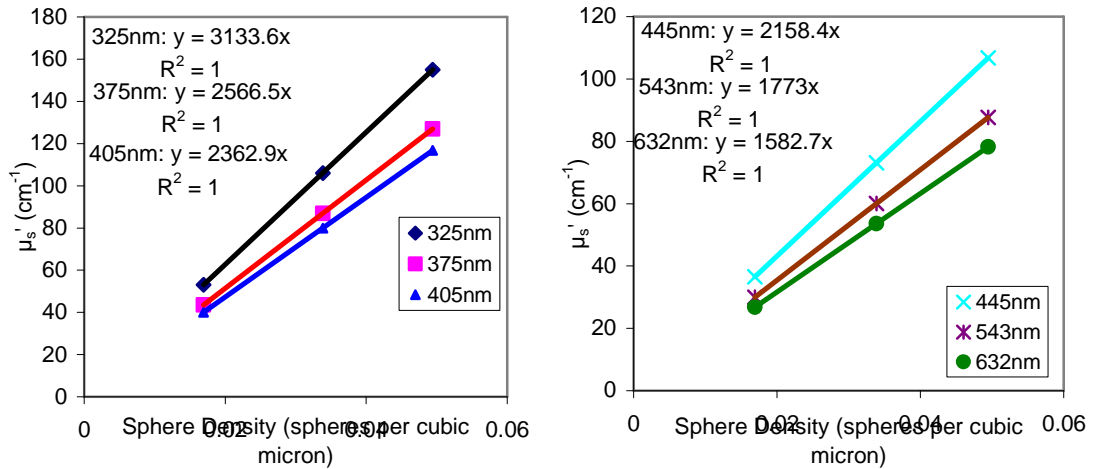


Fig. 25 μ_s' of polystyrene microsphere (0.989 micron diameter) as a function of wavelength



(a)

(b)

Fig. 26 μ_s' of polystyrene microsphere (0.989 micron diameter) as a function of density

Fig. 25 shows the monotonic decrease of μ_s' with wavelength except the lobe patterns between 300 nm and 350 nm. The lobe patterns come from the similar patterns of phase function by Mie theory in this range. (a) (b)

Fig. 26 shows that μ_s' increases linearly with sphere density.

Once the relations between the absorption coefficient/reduced scattering coefficient and the concentration/wavelength are known, phantoms with accurate optical properties can be constructed from deionized water, polystyrene microspheres, and nigrosine or hemoglobin at any desired property values. Fig. 27 shows a series of phantoms with polystyrene microspheres as scatterer and nigrosine as absorber.



Fig. 27 Phantoms with increasing μ_a and μ_s' held constant (nigrosine as absorber)

3.6 Construction and calibration of the fiberoptic diffuse reflectance system

3.6.1 Light source

The light source of the fiberoptic diffuse reflectance system can be either a lamp or a laser. A lamp emits incoherent photons in almost all directions, usually over a wide spectrum of wavelengths. A laser light, however, is typically near-monochromatic and emitted as a narrow beam in a specific direction. Besides, the light from a laser source is coherent. This means the waves of the laser light are in phase.

Since μ_a and μ_s' are functions of wavelength, their values are meaningful only at given wavelength. When a lamp is used as light source, it is usually used together with a spectrometer or a filter to get the desired wavelength, which makes the system clumsy and inefficient. Besides, it is difficult to couple the light into a fiber efficiently. On the other side, a laser source with a small volume can be used as a light source independently. And because of its directional property, laser can be coupled into a fiber easily. Therefore, laser sources were chosen in my system.

The spectral region below 600 nm (the UVA-VIS region) is essential for *in vivo* fiberoptic diagnostics especially for the fluorescence study. Besides, it is possible to study a smaller area on tissue with light in this region than with light of longer wavelength.

Shorter wavelength also means shorter source-detector (SD) separation. Only photons experiencing multiple scattering events can provide useful information about the scattering coefficient. Since the scattering coefficient of a tissue is higher at shorter wavelength, a photon with shorter wavelength will experience a given number of scattering events within a shorter SD separation. Since the data about the reflectance study in the UVA and VIS regions are limited, I want to fill up this blank. The laser wavelengths in our systems are 325 nm, 375 nm, 405 nm, 445 nm, and 543 nm.

3.6.2 Construction of the fiberoptic diffuse reflectance system

A multi-wavelength, fiberoptic diffuse reflectance system was developed as illustrated in Fig. 28. The system included five laser sources with wavelengths of 325 nm, 375 nm, 405 nm, 445 nm and 543 nm. The power output of the lasers was approximately one milliwatt except the 543 nm laser whose power output was about 50 μ W. The laser sources were coupled via a fiber switch to a linear array fiberoptic probe (Fig. 17). The diffuse reflected light was collected via five detection fibers at different distances from the illumination center and recorded as a spectrogram with a high-sensitivity charge-coupled device (CCD) camera (Princeton Instruments, Inc.). In-line neutral density (ND) filters were applied to attenuate signals in some fibers and thus maximize the dynamic range. A LabView (National Instruments Corporation) routine was developed to control the instrumentation, acquire data and calculate the reflectance based on calibration results described below.

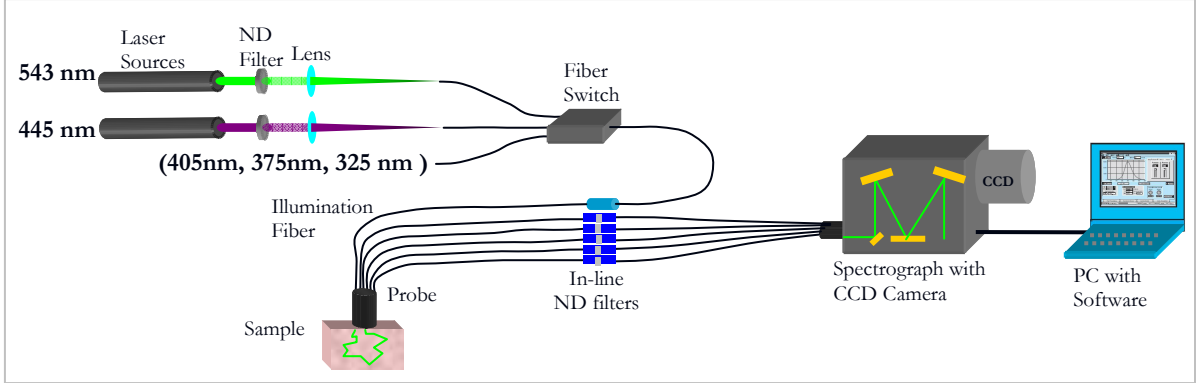


Fig. 28 Multi-wavelength, fiberoptic diffuse reflectance system for optical property measurement

3.6.3 Measurement of absolute reflectance intensity

Fig. 29 shows the light propagation in a turbid media and the detection of scattered light with a fiber probe. The intensity of scattered lights at the tissue surface decreases exponentially with distance from the illumination point (Fig. 30). The light intensity at positions with different distances from the illumination point is collected by five detection fibers and transferred to a spectrograph with a high-sensitivity CCD camera. CCD is the abbreviation of charge-coupled device which is an image sensor containing an array of coupled light-sensitive capacitors.

The intensity of light collected by each detection fiber could be three to six orders of magnitude difference if no filters are installed in the system. Since the intensity from each pixel on CCD is recorded by a 2 bytes (16 bits) number, the maximum intensity value is $2^{16}-1=65,535$. Therefore, the intensity from the highest detection fiber may have saturated the camera while the intensity from the lowest one is still too low. By applying the in-line neutral density (ND) filters to attenuate signals in several fibers with higher intensity, the light intensity levels through all the detection fibers are homogenized and the dynamic range of the CCD camera is broadened. The in-line ND filters in my system are optimized in such a way that the system can measure phantoms or tissues with

a wide optical property range. Fig. 31 shows a photo of light intensity obtained by a CCD camera from five detection fibers.

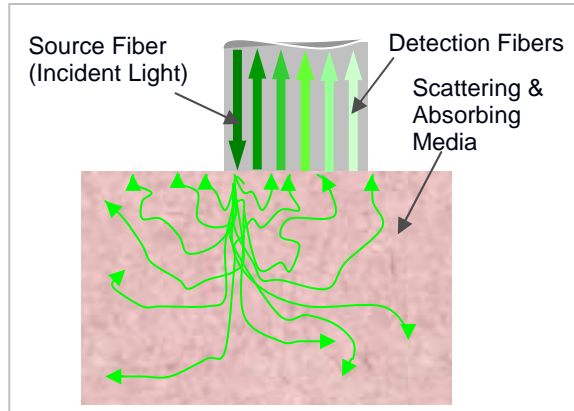


Fig. 29 Light propagation and the detection of scattered light by a fiber probe

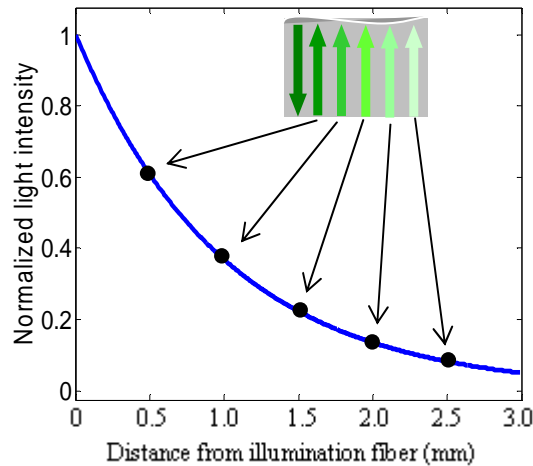


Fig. 30 Light intensity at tissue surface as a function of distance from an illumination fiber



Fig. 31 CCD camera image of light intensity obtained by the five detection fibers

3.6.4 System calibration - Converting intensity to reflectance

As shown in Fig. 31, data from the CCD camera is a 2-D matrix that represents light intensity in each pixel. Since the intensity of light from each detection fiber is attenuated differently by the ND filters, the intensity matrix cannot tell us the direct

information of the reflectance. The intensity matrix from each fiber should be converted to reflectance which is defined as the fraction of incident light from the illumination fiber that is collected by this fiber. It is proportional to the ratio of intensity per unit time from this fiber to the incident power (measured with a power meter) or the ratio of intensity within the exposure time from this fiber to the incident energy within the exposure time.

These relations can be expressed by the following equations:

$$R = \frac{P}{P_0} \propto \frac{I/t}{P_0} = \frac{I}{P_0 * t} = \frac{I}{E_0} \quad (17)$$

where P is the power of light collected through a detection fiber in watts, P_0 the incident power from the illumination fiber in watts, I the dimensionless intensity from CCD camera, t the exposure time in seconds, and E_0 the incident energy within the exposure time in joules. Therefore, there is a linear relation between the reflectance and the intensity per unit energy of illumination light for each detection fiber as shown below:

$$R = k \cdot \frac{I}{E_0} \quad (18)$$

where k is a constant for a given detection fiber at a given wavelength in joules.

The value of k for each detection fiber and at each wavelength was obtained during calibration. For a phantom with known μ_a and μ_s' , R from each detection fiber and at each wavelength was calculated from the condensed Monte Carlo simulation and I was measured by the CCD camera. E_0 was the product of the incident power P_0 and the exposure time t . Then, k was calculated according to equation 6 and should remain constant for samples with different μ_a and μ_s' . During calibration, a series of phantoms were constructed as described in section 2.4 and measured to determine I for each phantom and fiber. For each fiber, a graph of R versus I/E_0 was constructed and used to determine a linear best fit. The slope of this line was k . In all cases, the r^2 values were above 0.99. Once k for each detection fiber at each wavelength was obtained, the reflectance of a phantom with unknown optical properties could be calculated according to equation 6. This process was performed with a Matlab[®] routine coupled into the

LabView virtual instrument software. The k values were calculated once and occasionally verified using phantoms. Drift of k from its original value was not significant. Fig. 32~Fig. 36 show the relation between R and I / E_0 . The slopes of each trendline in these figures are the k values. The whole process of dealing with data was achieved by a Matlab routine coupled in the LabView control program.

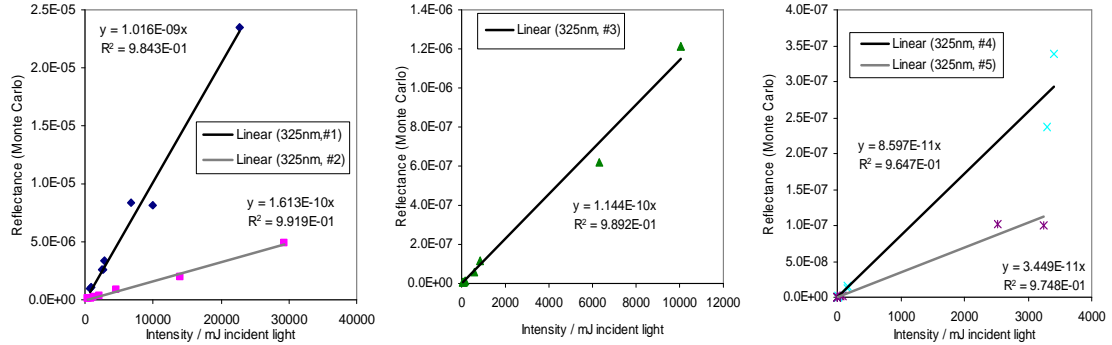


Fig. 32 Reflectance versus intensity per mJ of illumination light at 325 nm

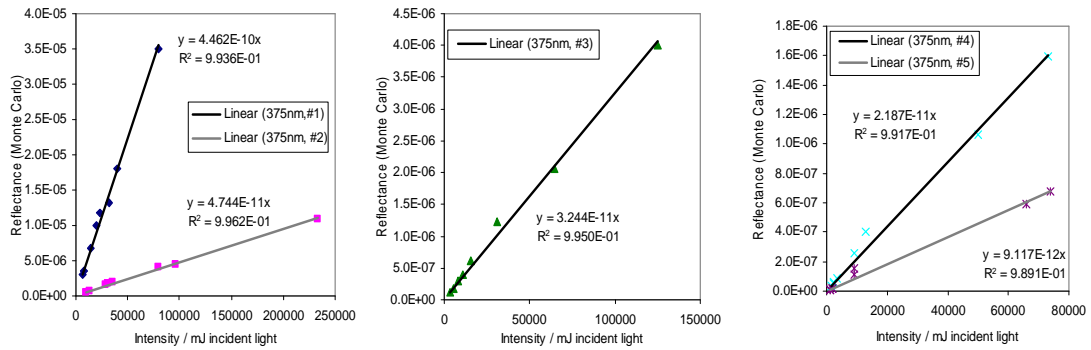


Fig. 33 Reflectance versus intensity per mJ of illumination light at 375 nm

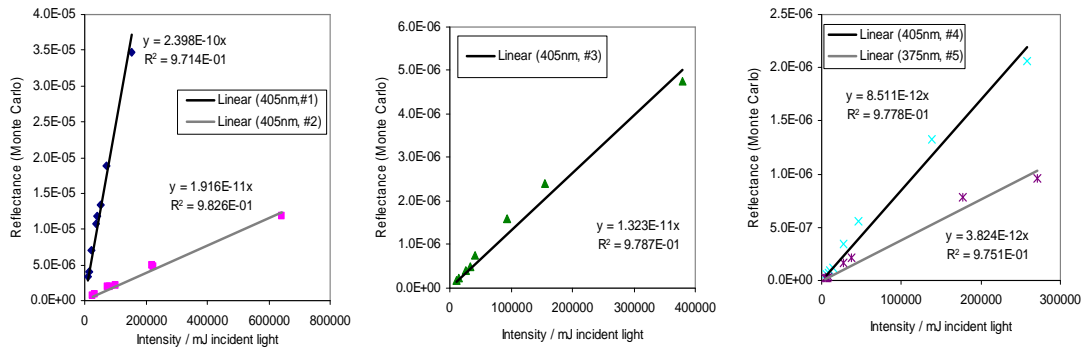


Fig. 34 Reflectance versus intensity per mJ of illumination light at 405 nm

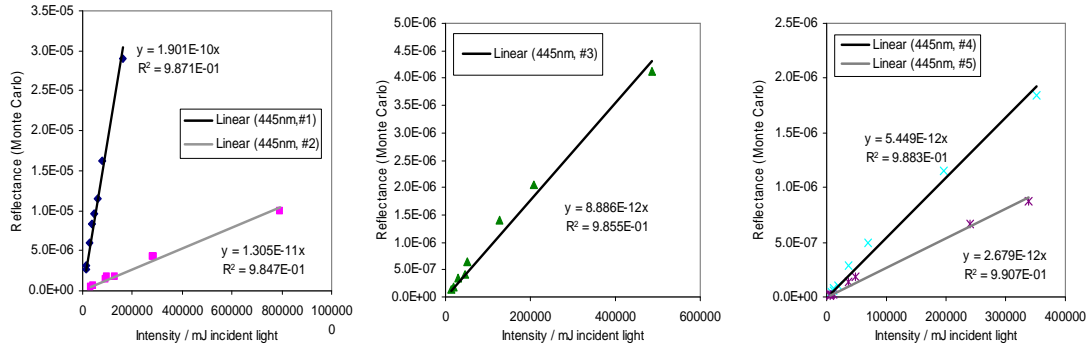


Fig. 35 Reflectance versus intensity per mJ of illumination light at 445 nm

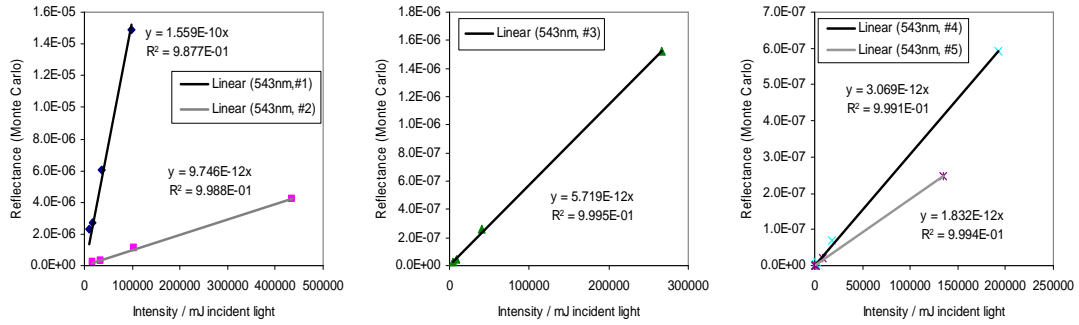


Fig. 36 Reflectance versus intensity per mJ of illumination light at 543 nm

3.7 *In vitro* validation of the reflectance system

To evaluate the performance of the fiber optic reflectance system and the mathematical models, tissue phantoms were constructed from deionized water, polystyrene microspheres (Polybead[®] Microspheres 1.00 μm , Polysciences, Inc.) and hemoglobin (Hb) (hemoglobin A0, ferrous stabilized human, Sigma H0267). Microspheres and Hb were chosen for their optical similarity to tissue scatterers and chromophores within the UVA-VIS spectral range. Microspheres of 1 μm diameter have commonly been used to simulate the cellular and structural protein scatterers in tissue¹⁴¹. Theoretical estimates of phantom μ_a and μ_s' were determined according to Beer's law and Mie theory. From the spatially-resolved reflectance, μ_a and μ_s' were calculated by the developed neural network based on 4 collection fibers. System accuracy was evaluated by comparing the theoretical μ_a and μ_s' with the values predicted from diffuse reflectance measurements.

Results for four tissue phantoms measured at all five wavelengths are shown in Fig. 37. The phantoms included two levels of absorption and scattering, as indicated in the graphs by Hb and polystyrene sphere concentrations. Figures 7 (a) and 7 (b) came from the neural network based on two detection fibers. Figures 7 (c) and 7 (d) came from the neural network based on four detection fibers. In general, these graphs show good agreement between theoretical and measured data, especially for μ_a . Absorption coefficient data display the well-known absorption signature of oxyhemoglobin, including a strong peak at 415 nm. While the 405 nm wavelength used in my measurements does not coincide with the peak of the oxyhemoglobin absorption curve, the phantom μ_a values at this wavelength are more than 3 times greater than at any of the other four wavelengths studied. The average error in predicting μ_a is 1.0 cm^{-1} for both Fig. 37 (a) and Fig. 37 (c). Figures 7 (b) and 7 (d) display the expected monotonic decrease in μ_s' with wavelength. It is worth noting that the greatest errors in μ_s' occur at 325 nm – where μ_a is low and μ_s' is high, which agrees with Fig. 20. The average error for μ_s' estimates are 3.0 cm^{-1} for Fig. 37 (b) and 2.7 cm^{-1} for Fig. 37 (d). Data points in Fig. 37 (a) and Fig. 37 (c) appear in pairs due to the fact that for each μ_a , two different μ_s' were investigated, and vice versa in Fig. 37 (b) and Fig. 37 (d).

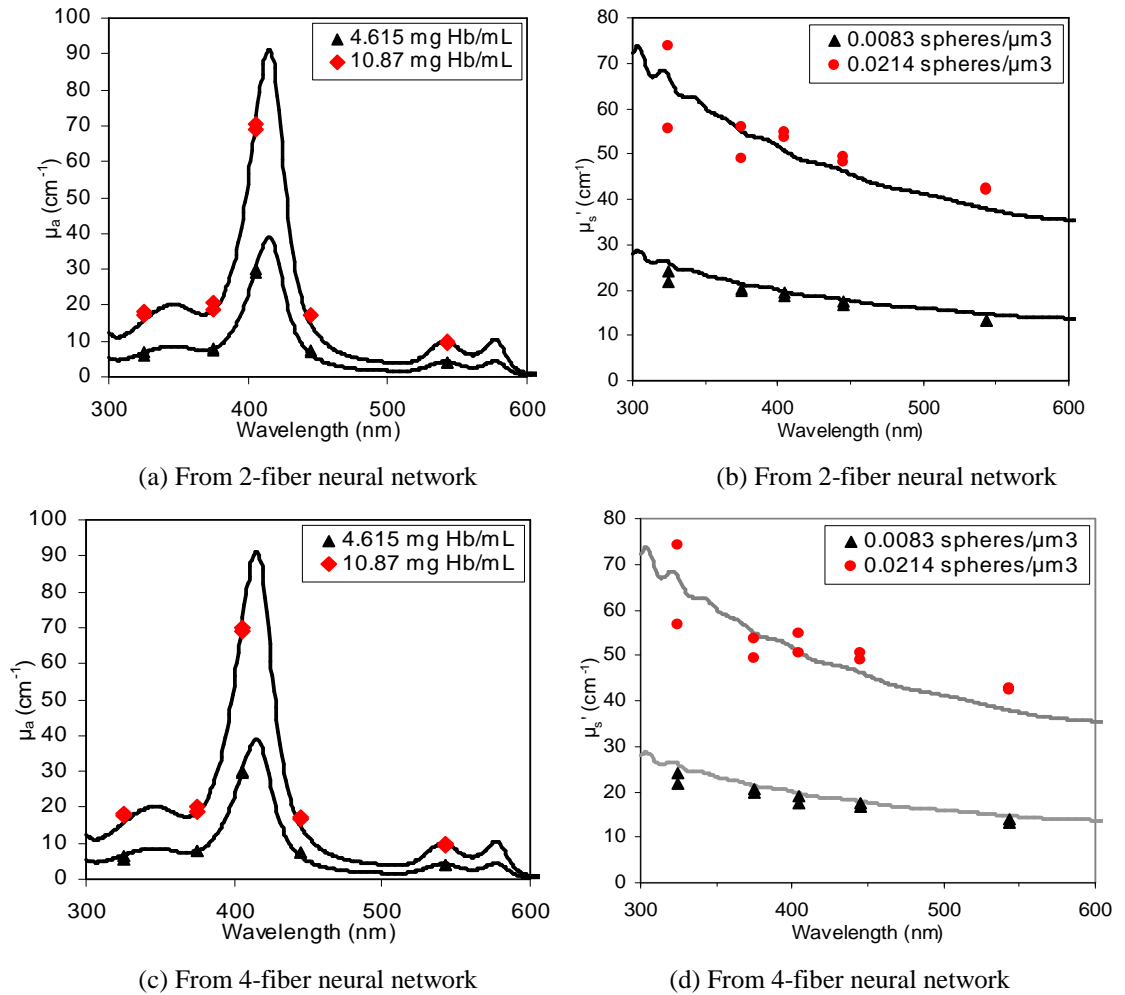


Fig. 37 Comparison of theoretical optical properties (curves in the graphs) with estimates based on reflectance measured with the fiberoptic system

3.8 *Ex vivo* tissue measurements

Fresh porcine esophagus, bladder, colon, oral mucosa, and liver tissues were brought back to my lab in a cooler filled with ice immediately after animals were sacrificed. The colon, esophagus, and bladder were dissected longitudinally. All tissues were placed in a Petri dish and covered with gauze moistened with saline to prevent desiccation after they were flushed with saline to remove excess materials on the surface. The time between sacrifice and commencement of measurements was approximately three hours. According to a recent study¹⁴², these tissue handling procedures should have been sufficient to avoid significant changes in reflectance, which can be altered by

processes such as freezing and thawing. To perform a measurement, the fiber-optic probe was placed gently on a tissue such that the tip was flush with the tissue surface. Reflectance data were collected at three different sites on each tissue. At each site, three measurements were taken followed by a background measurement with the light source blocked. Each site was moistened with saline before measurements. All tissue samples were measured within four hours of sacrifice. Typical measurement-to-measurement variation at a single site was approximately 1%. The tissue optical properties were determined from reflectance datasets with inverse neural network models (based on 2 collection fibers for liver and 4 collection fibers for other tissues). To evaluate the optical property results, forward condensed Monte Carlo simulations were run with the optical properties obtained from neural networks. The generated reflectance values for tissues at different wavelengths were then compared with the measured values.

Average μ_a and μ_s' values measured in porcine liver and mucosal tissues of the bladder, colon, esophagus and oral cavity from three swine are displayed in Fig. 38. Data in these graphs were calculated by the neural network based on reflectance from four detection fibers, except for the liver data which was based on two detection fibers because of its high absorption. When the two fiber approach and four fiber approach were compared during mucosal tissue measurements, the former was shown to have 7% greater variability. However, very highly attenuating tissue measurements are limited by the detector noise floor and the potential for thermal damage due to higher irradiation levels.

The *ex vivo* tissues show relatively consistent spectral trends in μ_a and μ_s' , specifically, a decrease in μ_a from 325 nm to 375 nm, followed by an increase to 405 nm and consecutive decreases to 445 and 543 nm. Estimates of μ_s' showed a monotonic decrease with wavelength, although the magnitude of this decrease varied from tissue to tissue.

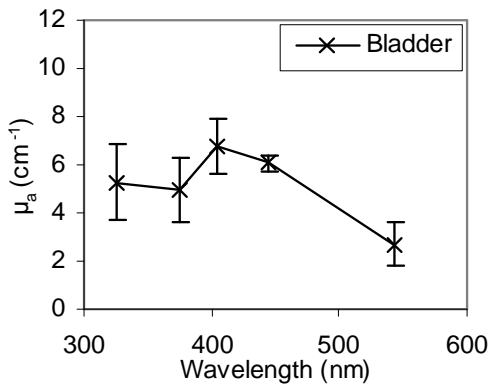
Exceptions to these trends are also evident, most notably, the minimal decrease in μ_s' with wavelength for colon tissue (Fig. 8 (d)) and a higher than expected μ_a value at

543 nm for esophageal tissue (Fig. 8 (e)). These results may be due to significant tissue inhomogeneities, irregularities in placement of the probe (e.g., an air bubble between the probe and tissue), variations in laser power or some combination of these issues.

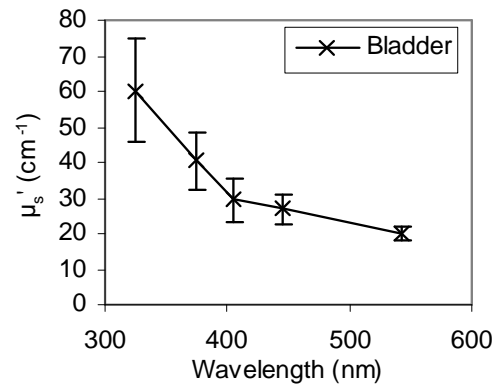
The similarities in results are even greater for the epithelial tissue samples: bladder, colon, esophagus, and oral mucosa. These tissues show similar optical property magnitudes as well, with μ_a ranging from 1 cm^{-1} to 15 cm^{-1} and μ_s' ranging from 15 cm^{-1} to 65 cm^{-1} . In general, μ_a of bladder and colon is higher than μ_a of esophagus and oral mucosa, μ_s' of bladder is higher than μ_s' of other tissues at 325 nm. While the μ_s' level of the one non-epithelial tissue – liver – is similar to other tissues, its μ_a is significantly higher, likely due to high blood content.

The error bars in Fig. 8 demonstrate the significant variation in optical properties found in this study. It is worth noting that these error levels are approximately equal to or less than the levels documented in the literature¹⁴³⁻¹⁴⁵. For example, Zonios *et al.* showed that the typical standard deviation of optical properties of colons from different animals were in the $\pm 30\text{-}50\%$ range¹⁴⁵. This level of standard deviation helps to explain the wide variations in the optical properties reported in different papers, such as μ_a values of human colons at 475 nm measured as 12 cm^{-1} and 2 cm^{-1} in two different papers^{112, 143}. Our preliminary findings in comparing repeat measurements at a single location to measurements at different sites and in different animals indicate that a significant portion of this variation may be due to local, regional or animal-to-animal variations (e.g. collagen fibers, animal growth stage). One possible source of error is discrete blood vessels which it may be possible to account for using correction factors¹⁴⁶. Another variable may be the presence, thickness and optical properties of mucosal epithelia.^{13, 147} While several techniques for measuring the optical properties of multi-layer tissues have been proposed, there is no consensus in the literature as to the best way to accomplish this task, nor is there significant tissue data using these proposed methods.

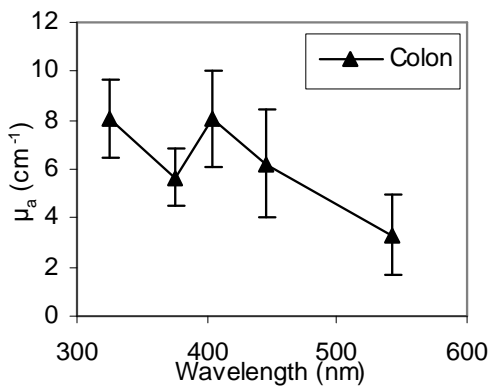
52, 148



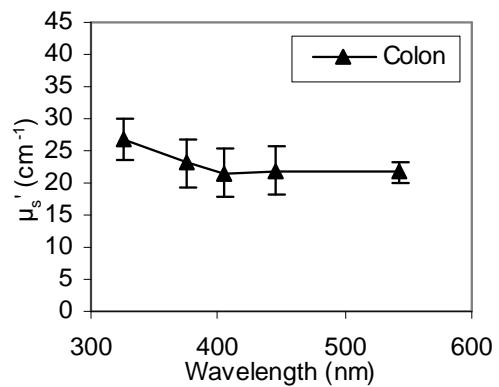
(a)



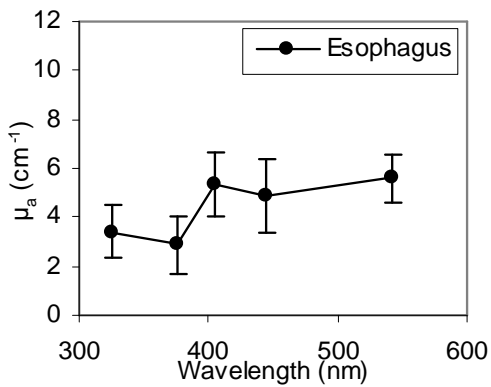
(b)



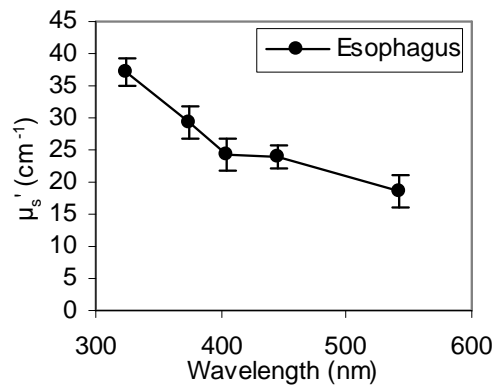
(c)



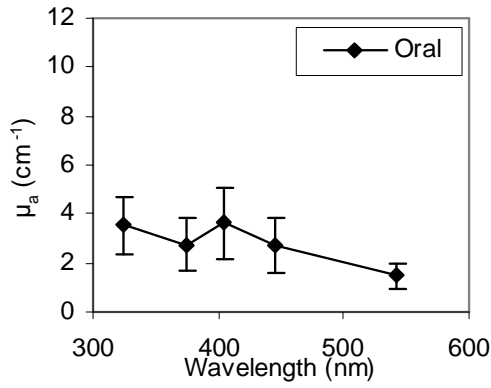
(d)



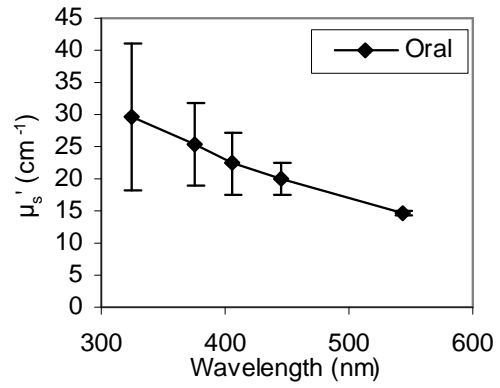
(e)



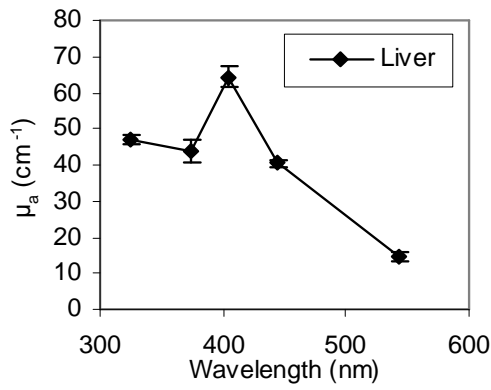
(f)



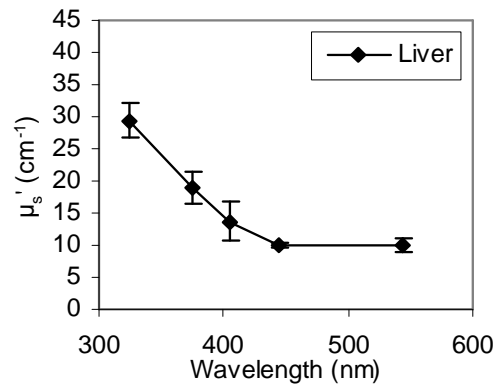
(g)



(h)



(i)



(j)

Fig. 38 Optical properties of porcine tissues (average values of three animals)

To evaluate the optical property results in Fig. 38 in a direct way, forward condensed Monte Carlo simulations were run with the optical properties obtained from tissues using neural networks. The generated reflectance values were then compared with the measured ones. Data on oral mucosa and liver are presented in Fig. 39. In general, the reflectance values from Monte Carlo simulation matched very well with the measured values, providing further validation of my approach in nonhomogeneous tissue.

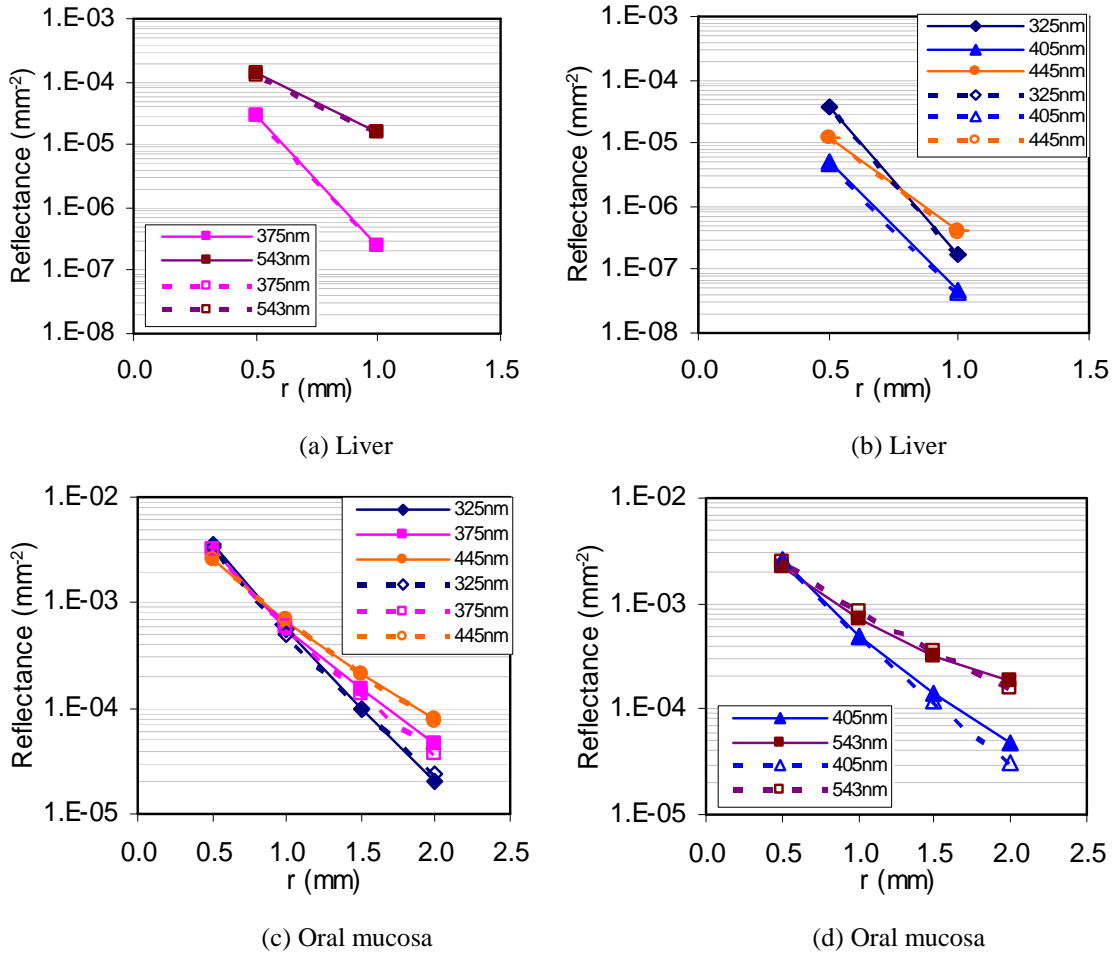


Fig. 39 Reflectance as a function of distance from center of illumination fiber (r) (Hollow symbols indicate the values from forward condensed Monte Carlo simulations. Solid symbols indicate the measured values.)

Table 4 provides a summary of relevant published data on tissue optical properties. Some data in this table were estimated from printed graphs. The μ_s' of human esophagus in Holmer *et al.*'s paper¹⁴⁴ roughly matches my value at 325 nm. However, the μ_a is about six times higher than my value. The results of human esophagus by Georgakoudi *et al.*¹² agree with my porcine results. The μ_a and μ_s' of human colon in Wei *et al.*'s paper¹¹² match my results of porcine colon, while the μ_a values of human colon in Zonios *et al.*'s paper¹⁴⁵ are higher than my porcine colon results and their μ_s' values are lower. From Ritz *et al.*'s paper¹⁴⁹, their μ_a values of porcine liver are lower than mine and μ_s' values are higher. The μ_a values in Parsa *et al.*'s paper¹⁵⁰ is consistent

with my porcine results. Their μ_s' values are higher than mine. When comparing these results, it is important to note that the optical properties may change during tissue preparation¹⁴².

As noted previously, the curves in Fig. 8 have several features in common. The peak in μ_a at 405 nm is consistent with the established concept that Hb is the dominant chromophore for most tissues in the visible range. However, the intensity of this peak relative to values at nearby wavelengths is much less than shown in tissue phantoms, and the decrease in μ_a from 325 nm to 375 nm is not consistent with the Hb-dominated phantom results. These findings support the idea that at short visible wavelengths other chromophores become increasingly significant. According to the literature, tissue constituents such as collagen, elastin, DNA and some other proteins (especially those with high aromatic amino acid content such as tryptophan and tyrosine) also contribute to the absorption of UVA light¹⁵¹⁻¹⁵³.

Table 4. Optical properties from literature

Tissue	Wavelength h (nm)	μ_a (cm^{-1})	μ_s' (cm^{-1})	Tissue preparation	Reference
Human esophagus	330	24.7	30.5	Frozen, homogenized	Holmer <i>et al.</i> ¹⁴⁴
Human esophagus	405 445 543		23 21 20	Fresh, bulk, <i>ex vivo</i>	Georgakoudi <i>et al.</i> ¹²
Human colon	476-532	2.3-3.3	24.6- 19.1	Fresh, sliced, <i>ex vivo</i>	Wei <i>et al.</i> ¹¹²
Human colon	325 375 405 445 543	13 9 21 7 4	22 15 14 10 8	Frozen, sliced	Zonios <i>et al.</i> ¹⁴⁵
Porcine liver	405 445 543	45 20 13	30 18 12	Frozen, homogenized	Ritz <i>et al.</i> ¹⁴⁹
Rat liver	375 405 445 543	57 60 42 20	23 20 19 15	Fresh, sliced, <i>ex vivo</i>	Parsa <i>et al.</i> ¹⁵⁰

In order to clarify the role of structural proteins such as collagen, I have performed preliminary spectrophotometric measurements of collagen (type I, bovine, BD Biosciences 354231) absorption. These data are graphed in Fig. 40 along with the μ_a of Hb (hemoglobin A0, ferrous stabilized human, Sigma H0267). The μ_a of collagen increases exponentially with decreasing wavelength within the UVA range. Although the absolute value of collagen μ_a is two magnitudes less than that of Hb, the contribution of other chromophores such as collagen and elastin to μ_a of tissues can still be remarkable considering the higher concentration of these chromophores relative to Hb. Therefore, it is likely that the μ_a distributions in Fig. 38 are due to the superposition of Hb and other chromophores such as collagen and elastin. In the future, it may be possible to determine the concentrations of these chromophores through fitting algorithms.

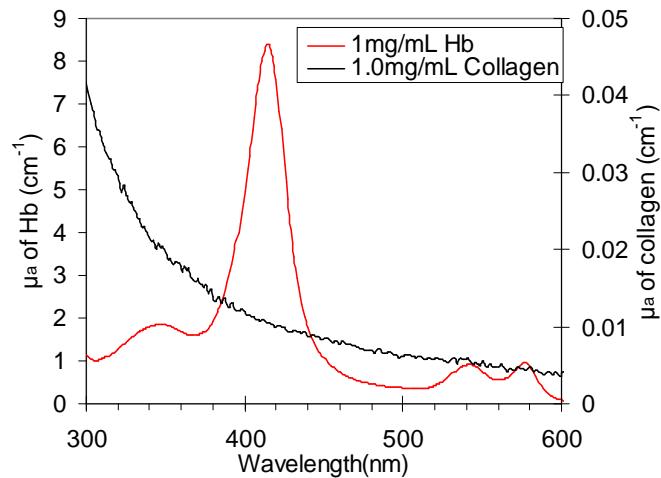


Fig. 40 Absorption coefficient of Hb and type I collagen

3.9 Conclusion

Towards the goal of accurate *in vivo* measurements of tissue optical properties, I have constructed and evaluated a novel fiberoptic-based system for optical property measurement within the UVA-VIS wavelength range. My approach involves a neural network-based inverse model calibrated with reflectance datasets simulated using a condensed Monte Carlo approach with μ_a up to 85 cm^{-1} and μ_s' up to 118 cm^{-1} .

Theoretical evaluation of the inverse model showed good agreement between calculated and theoretical values. Experimental evaluation on tissue phantoms showed average errors in predicting μ_a and μ_s' of 1.0 cm^{-1} and 2.7 cm^{-1} .

Optical property data collected in unprocessed mucosal and liver tissues *ex vivo* provide evidence that the current approach can produce useful data on tissue optical properties over a wide range of optical characteristics. Significant tissue-specific variations in scattering and absorption were found. Scattering coefficients decreased monotonically with wavelength. Variations in absorption with wavelength indicate a shift in primary chromophore from hemoglobin at visible wavelengths to other components, likely other proteins, in the ultraviolet. While significant variability in optical properties was found for individual tissue types, this variability tended to be less than in prior studies. However, additional research is needed to investigate their origin.

Chapter 4. OPTICAL STUDY OF SINGLE-LAYER TISSUES WITH AN ILLUMINATION-DETECTION FIBER

4.1 Introduction

Reflectance spectroscopy has been demonstrated to be useful for providing biochemical and morphological information for minimally-invasive detection of cancer in mucosal tissues such as the cervix^{7,8}, esophagus^{9,11}, colon^{13,14}, as well as breast tissue^{154,155}. It has also been used for monitoring of tissue oxygenation^{17,20} and analytes such as bilirubin^{25,29} and glucose^{32,35}. Furthermore, reflectance-based approaches are critical for providing fundamental optical property data on biological tissues which are used in theoretical models and to extract intrinsic optical signals for disease diagnosis³⁶⁻³⁹. These tasks can be accomplished using imaging techniques or fiberoptic probes. Non-imaging systems based on fiberoptic probes can be categorized into two groups: those with separate fibers for illumination and detection^{39,67,110} and those in which the illumination and detection regions overlap, such as with a single fiber^{107,108,156,157}. In this dissertation I use the term “illumination-detection fiber” to denote this latter geometry. While my study in Chapter 3 mainly focuses on the first group of fibers, I will focus on illumination-detection fibers in this chapter.

Illumination-detection fiber geometries have been implemented in clinical¹⁵⁸⁻¹⁶¹ and theoretical¹⁶²⁻¹⁶⁴ studies of fluorescence spectroscopy, as well as a variety of studies involving reflectance measurement from tissue. Moffitt *et al.* developed a sized-fiber probe for measuring local optical properties. The probe included two fibers with different diameters. Each fiber illuminated and detected its own backscattered light at 632.8 nm.¹⁰⁸ Bargo *et al.* studied how the collection efficiency of a single optical fiber depended on the optical properties of turbid media¹⁵⁷. Amelink *et al.* measured the local optical properties of tissue with an approach that included an illumination-detection fiber and a

detection fiber¹⁰⁷. Papaioannou *et al.* investigated effects of fiber-optic probe design and probe-to-target distance on diffuse reflectance measurement of turbid media with a single fiber probe¹⁵⁶.

Calculation of light propagation and reflectance distribution in a tissue is commonly performed using Monte Carlo modeling. While accurate, this approach can be computationally inefficient. Various techniques have been developed to improve its efficiency^{124,125}. The condensed Monte Carlo simulation introduced by Graaff *et al.*¹²⁵ is theoretically transparent and relatively easy to implement. Palmer and Ramanujam¹²⁶ extended Graaff *et al.*'s condensed Monte Carlo method from a ray source to a beam source and from the total reflectance to the reflectance with a detection fiber by convolution. This condensed Monte Carlo method has been applied to accelerate the simulation of reflectance by detection fibers⁴⁰. However, these prior studies did not address the single fiber approach.

In Chapter 3, I implemented a condensed MC method to accelerate the simulation of reflectance measured by detection fibers. In this chapter, I have derived and validated two convolution equations for the condensed Monte Carlo simulation to calculate the reflectance from an illumination-detection fiber. I also developed a scaling equation to scale the maximum penetration depth of a photon. These equations, together with those described in earlier paper^{125,126} extend the simulation capability of condensed Monte Carlo method and can generate theoretical reflectance of media with different optical properties from both an illumination-detection fiber and several detection fibers based on one primary Monte Carlo simulation. With the extended Monte Carlo method, I studied the influence of illumination-detection fiber size on the reflectance in a wide μ_a and μ_s' range. The method was then implemented to study the effect of illumination-collection fiber diameter on the ability to distinguish between normal and cancerous breast tissues using reflectance spectra. The method was also used to evaluate the additive benefit of illumination-detection fiber data to improve the accuracy of diffuse-reflectance

based tissue optical property measurements. Finally, effect of optical properties, detection distance from the illumination point, and size of an illumination-detection fiber on detection depth were studied.

4.2 Condensed Monte Carlo simulation for an illumination-detection fiber

4.2.1 Convolution equations for an illumination-detection fiber

I have derived two convolution equations for an illumination-detection fiber . They can be used to convert data from a primary MC simulation of a ray source illumination in a tissue with absorption coefficient of $\mu_{a,sim}$ and scattering coefficient of $\mu_{s,sim}$ to a new set of data for a beam source in tissue with absorption coefficient of $\mu_{a,new}$ and scattering coefficient of $\mu_{s,new}$. I assume that the system is circularly symmetric, *i.e.*, the illumination-detection fiber is normal to a homogeneous medium and the system is symmetric about the central axis of the fiber. Let the fiber be centered at the origin with radius r_i . Because the system is symmetric, a photon launched at $(x,0)$ with a net travel distance of r_t may exit the surface anywhere along the circle centered at $(x,0)$ with radius r_t (blue circle in Fig. 41) with equal probability. All photons launched from the circle centered at origin with radius x (red circle in Fig. 41) have the same p_0 value. Therefore, the probability that a photon launched from a circular fiber will be collected by the same fiber after traveling a net distance r_t can be calculated by

$$p = \frac{1}{\pi \cdot r_i^2} \int_0^{r_i} p_0 \cdot (2\pi x) \cdot dx \quad (19)$$

where p_0 is the probability that the photon launched at $(x,0)$ (blue point) is collected by the fiber and $(2\pi x) \cdot dx$ is the differential element of a small area. Since p_0 is a function of r_t and x , p can be expressed in different ways under different conditions:

(1) $r_t \geq 2r_i$

In this case, the photon can not be detected by the fiber, $p = 0$.

(2) $0 < r_t \leq r_i$

If $0 \leq x \leq r_i - r_t$, $p_0 = 1$. Therefore,

$$p = \frac{1}{\pi \cdot r_i^2} \int_0^{r_i - r_t} 1 \cdot (2\pi x) \cdot dx$$

which can be simplified as

$$p = \left(\frac{r_i - r_t}{r_i} \right)^2 \quad (20)$$

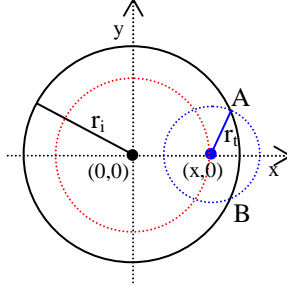


Fig. 41 Schematic of the fiber configuration ($0 < r_t \leq r_i$)

If $r_i - r_t < x \leq r_i$, probability of a photon launched at $(x,0)$ is collected by the fiber (Fig. 41) is

$$p_0 = 2 \cdot \cos^{-1} \left[\frac{r_t^2 + x^2 - r_i^2}{2 \cdot x \cdot r_t} \right] \cdot \frac{1}{2\pi} = \frac{1}{\pi} \cdot \cos^{-1} \left[\frac{r_t^2 + x^2 - r_i^2}{2 \cdot x \cdot r_t} \right] \quad (21)$$

Substitution of Eq. 21 into Eq. 19 yields

$$p = \frac{1}{\pi \cdot r_i^2} \int_{r_i - r_t}^{r_i} \frac{1}{\pi} \cdot \cos^{-1} \left[\frac{r_t^2 + x^2 - r_i^2}{2 \cdot x \cdot r_t} \right] \cdot (2\pi x) \cdot dx$$

which can be simplified as

$$p = \frac{2}{\pi \cdot r_i^2} \int_{r_i - r_t}^{r_i} \cos^{-1} \left[\frac{r_t^2 + x^2 - r_i^2}{2 \cdot x \cdot r_t} \right] \cdot x \cdot dx \quad (22)$$

Therefore, the probability that a photon launched from the circular fiber will be collected by the same fiber after traveling a net distance r_i , in the whole range of $0 \leq x \leq r_i$ and under the condition of $0 < r_t \leq r_i$, can be calculated by combining Eq.(20) and Eq.(22) as following:

$$p = \left(\frac{r_i - r_t}{r_i}\right)^2 + \frac{2}{\pi \cdot r_i^2} \int_{r_i - r_t}^{r_i} \cos^{-1}\left[\frac{r_t^2 + x^2 - r_i^2}{2 \cdot x \cdot r_t}\right] \cdot x \cdot dx \quad (23)$$

(3) $r_i < r_t \leq 2r_i$

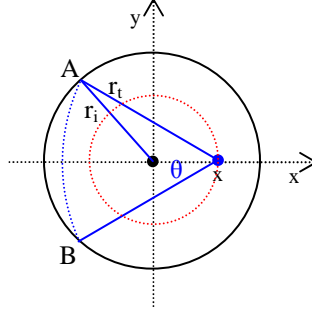


Fig. 42 Schematic of the fiber configuration ($r_i < r_t \leq 2r_i$)

Probability of the photon launched at $(x,0)$ is collected by the fiber is:

$$p_0 = 2 \cdot \cos^{-1}\left[\frac{r_t^2 + x^2 - r_i^2}{2 \cdot x \cdot r_t}\right] \cdot \frac{1}{2\pi} = \frac{1}{\pi} \cdot \cos^{-1}\left[\frac{r_t^2 + x^2 - r_i^2}{2 \cdot x \cdot r_t}\right]$$

If $x < r_t - r_i$, $p = 0$. To make sure a photon can be collected, the relations of $r_t - r_i < x < r_i$, $r_i + r_t > x$, $r_i + x > r_t$ and $r_t + x > r_i$ should be satisfied. In sum, the range of x should be $r_t - r_i < x < r_i$. Therefore,

$$p = \frac{1}{\pi \cdot r_i^2} \int_{r_i - r_t}^{r_i} \frac{1}{\pi} \cdot \cos^{-1}\left[\frac{r_t^2 + x^2 - r_i^2}{2 \cdot x \cdot r_t}\right] \cdot (2\pi x) \cdot dx$$

which can be simplified as

$$p = \frac{2}{\pi \cdot r_i^2} \int_{r_i - r_t}^{r_i} \cos^{-1}\left[\frac{r_t^2 + x^2 - r_i^2}{2 \cdot x \cdot r_t}\right] \cdot x \cdot dx \quad (24)$$

Eq. 23 and Eq. 24 can be used to convert data from a primary Monte Carlo simulation of a ray source illumination in a tissue to a new set of data for a beam source in the tissue.

4.2.2 Scaling equation for maximum penetration depth

Eq. 13 in Chapter 3 shows the scaling equation to calculate the distance from entrance to exit of a photon in a tissue with given optical properties according to data from a primary Monte Carlo simulation with optical properties of $\mu_{a,sim}$ and $\mu_{s,sim}$. In the

same way, the maximum depth that a photon penetrates into a tissue with optical properties of $\mu_{a,new}$ and $\mu_{s,new}$ can also be calculated with a similar equation as following

$$d_{new} = d_{sim} \cdot \left(\frac{\mu_{s,sim} + \mu_{a,sim}}{\mu_{s,new} + \mu_{a,new}} \right) \quad (25)$$

where d_{sim} is the maximum penetration depth of a photon from the primary Monte Carlo simulation and d_{new} is the maximum penetration depth of this photon in a tissue with different optical properties from the primary one.

4.2.3 Condensed Monte Carlo model

The principle of condensed Monte Carlo modeling has been described in Chapter 3. In this chapter, convolution equations of Eq. 23 and Eq. 24 were coupled into the condensed Monte Carlo model developed in Chapter 3 to calculate reflectance values from illumination-detection fibers. The parameter of r_i in these equations has the same meaning as r_{new} in Chapter 3. Besides, the scaling equation of Eq. 25 was also coupled into the model to calculate the maximum penetration depths of detected photons. The geometry used in the simulations replicated the design of my fiberoptic probe. A diagram of the probe face is shown in Fig. 43. The probe contains linearly arranged fibers, a single illumination-detection fiber and five detection fibers, spaced at consecutive center-to-center distances of 0.5 mm. The core diameter of each fiber is 0.2 mm with a numerical aperture (NA) of 0.22. This model was used throughout this chapter and parameters and details of this model are the same as those in Chapter 3 if not otherwise specified.

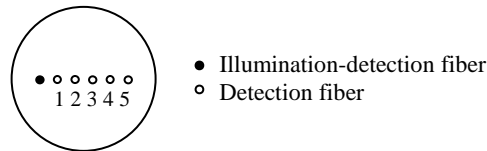


Fig. 43 The 4 mm diameter face of the fiberoptic probe

4.2.4 Evaluation of convolution equations for an illumination-detection fiber and the scaling equation for maximum penetration depth of a photon

The accuracy of Eq. 23 and Eq. 24 was evaluated by comparing the reflectance from condensed Monte Carlo simulations with that from standard Monte Carlo simulations. A series of optical properties with μ_a values as 1, 10, 20, 30, and 40 cm^{-1} and μ_s' values as 5, 15, 25, 37.5, 50, 62.5, 75, 87.5 and 100 cm^{-1} (Fig. 44) were employed to evaluate the equations for two illumination-detection fibers with radii of 0.1 mm and 0.5 mm respectively. Fig. 45 shows the evaluation results in the form of reflectance from condensed Monte Carlo simulations versus reflectance from standard Monte Carlo simulations. The dashed line in Fig. 45 is where the results from both methods are same (0% error). The average errors from the condensed Monte Carlo simulations were found to be 6.3% for the fiber with radius of 0.1 mm and 5.1% for the fiber with radius of 0.5 mm. In general, less reflectance signal will be detected with smaller μ_s' , larger μ_a , and smaller fiber radius, which in turn will bring larger error. The effect of small μ_s' on the average error of condensed Monte Carlo simulations is significant. If the evaluation results from μ_s' of 5 cm^{-1} (grey symbols in Fig. 44) are excluded, the average error will become 5.1% for the fiber with radius of 0.1 mm and 3.2% for the fiber with radius of 0.5 mm.

The condensed Monte Carlo simulations are not only accurate, but also fast. The calculation time of both standard and condensed Monte Carlo models is proportional to the number of photons. Fig. 46 shows the calculation time of both methods for 40 million photons using a computer with 2992 Mhz processor and 1 GB physical memory. For the standard Monte Carlo simulation, smaller μ_a and/or bigger μ_s' can significantly slow down the speed (Fig. 46a). For the condensed Monte Carlo simulation, however, the speed will be reduced mainly by bigger μ_s' (Fig. 46b) and bigger radius. For illumination-detection fibers with radii of 0.1 mm and 0.5 mm, condensed Monte Carlo reduced the

calculation time by three orders of magnitude and two orders of magnitude respectively, compared with the standard Monte Carlo model.

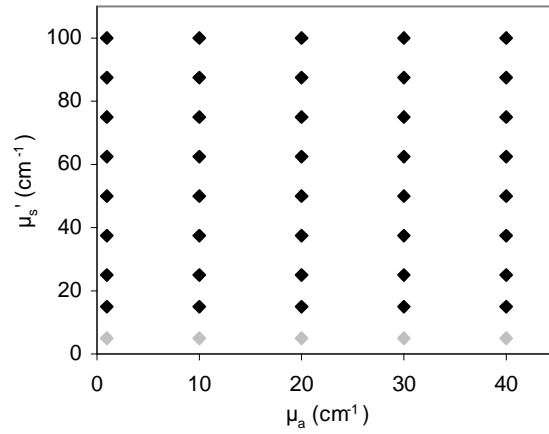
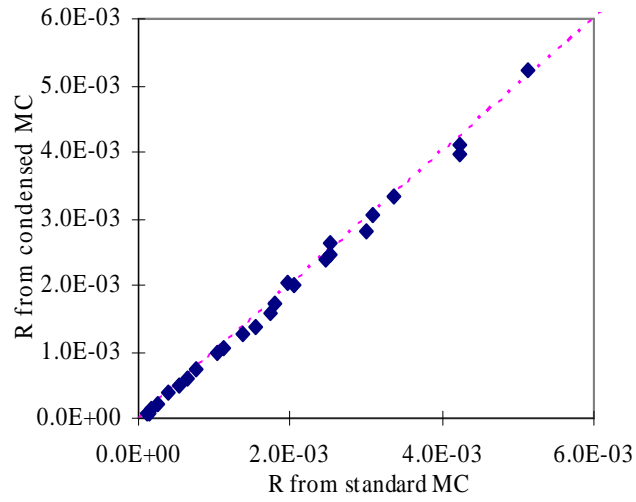
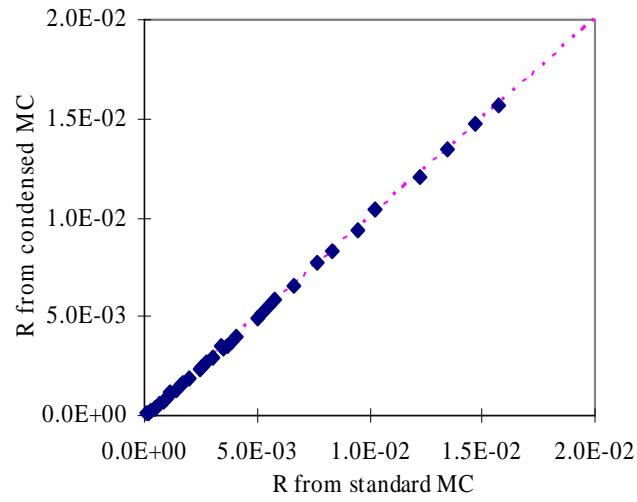


Fig. 44 Optical properties for evaluation of Eq. 23 and Eq. 24

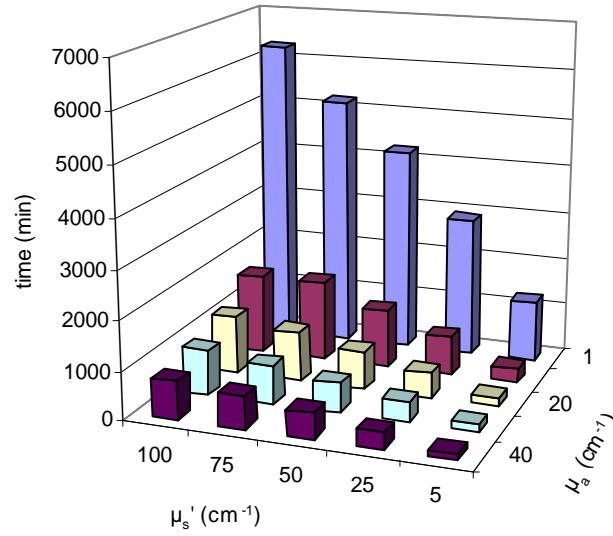


(a) radius = 0.1 mm

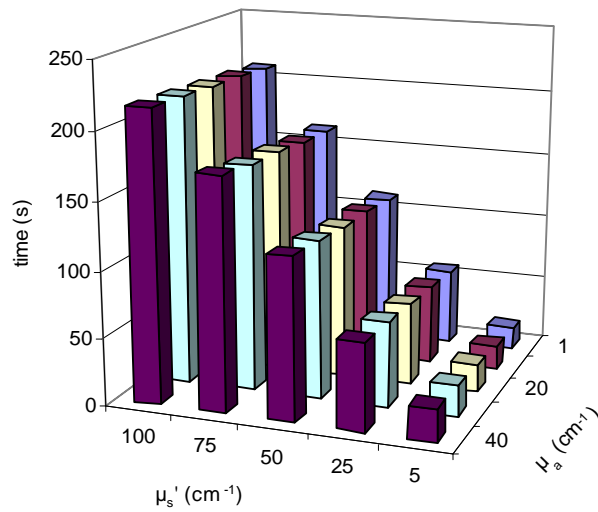


(b) radius = 0.5 mm

Fig. 45 Reflectance from condensed MC simulations versus reflectance from standard MC simulations



(a) standard Monte Carlo



(b) condensed Monte Carlo

Fig. 46 Simulation speeds of (a) standard Monte Carlo (in minutes) and (b) condensed Monte Carlo (in seconds) models for an illumination-detection fiber with radius of 0.1 mm

To evaluate Eq. 25, the average values of maximum penetration depths of detected photons from condensed Monte Carlo simulations were compared with those from standard Monte Carlo simulations. Maximum detection depths of twelve tissues with optical properties shown in Table 5 were simulated. The average maximum penetration depth of photons detected by the illumination-detection fiber and detection fibers (Fig. 43) were calculated with both condensed Monte Carlo simulations and

independent Monte Carlo Simulations (Fig. 47). Again, the line in Fig. 47 is where the standard Monte Carlo results are the same as condensed Monte Carlo results. The legend in the figure shows the fiber center distance from the illumination point. Since all points fall right on the line or close to the line, the scaling equation for maximum penetration depth of a photon is proven to be accurate. Also, from different symbols for each detection fiber, we can see that a fiber further from the illumination point usually detects photons that penetrate deeper into the tissue.

Table 5. Optical properties for evaluation of the scaling equation

μ_a (cm ⁻¹)	1	1	1	1	5	5	5	5	10	10	10	10
μ_s' (cm ⁻¹)	1	10	15	20	1	10	15	20	1	10	15	20

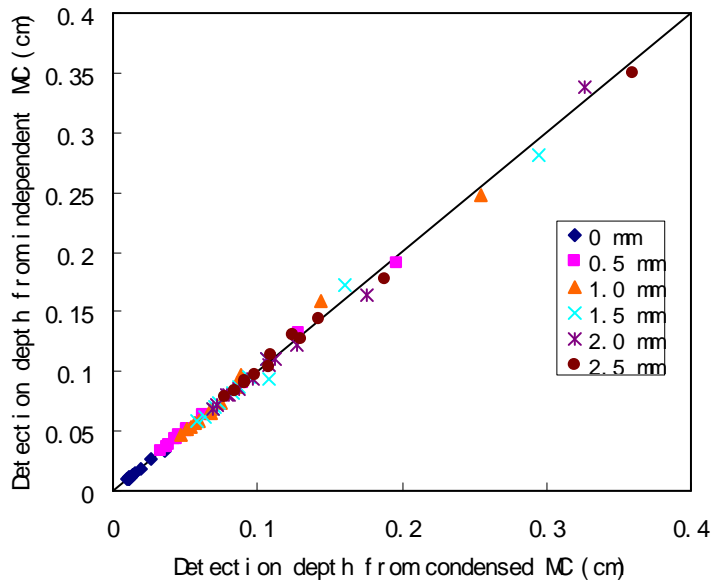
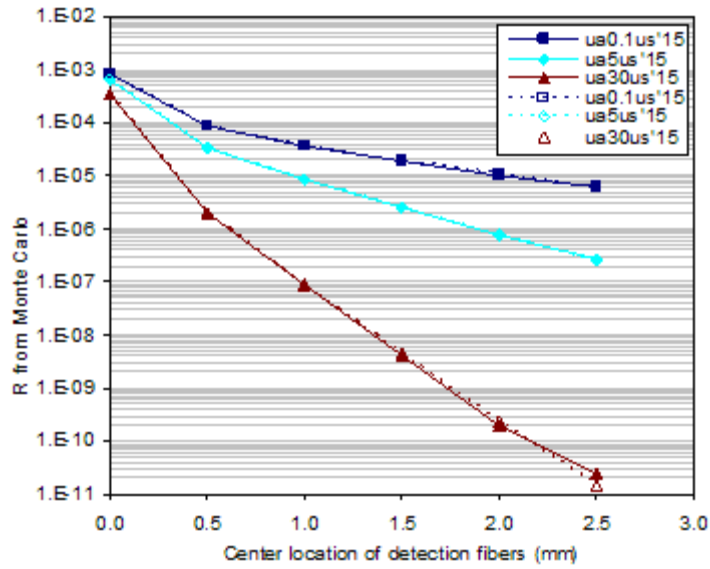


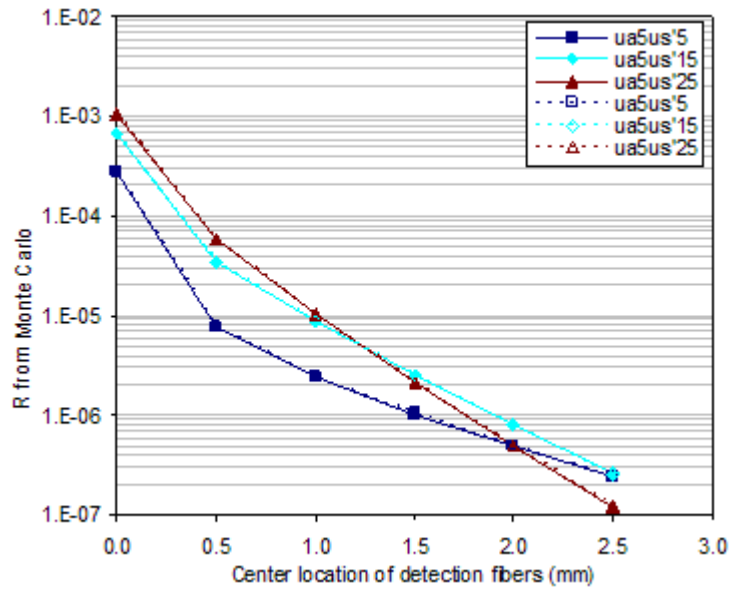
Fig. 47 Average values of maximum penetration depth from condensed MC simulations versus the values from standard MC simulations

Accuracy of the condensed Monte Carlo technique was further evaluated by simulating reflectance values of tissues with different optical properties from both the illumination-detection fiber and detection fibers. Fig. 48 shows the reflectance values from a fiber probe shown in Fig. 43. In this figure, hollow symbols are from condensed Monte Carlo simulations and solid symbols are from standard Monte Carlo simulations. The legend shows the different optical properties in simulations. From the figure, results

from the condensed Monte Carlo simulations almost overlap with those from the standard Monte Carlo simulations. Fig. 49 shows the reflectance from condensed Monte Carlo simulations versus that from standard Monte Carlo simulations, the same data as in Fig. 48 but shown in a different way. The dash line is where the values from condensed Monte Carlo simulations are equal to those from standard Monte Carlo simulations. There is only 1% difference in reflectance values between the condensed Monte Carlo simulations and the standard Monte Carlo simulations except the values from the fourth and fifth detection fibers when μ_a is 30 cm^{-1} and μ_s' is 15 cm^{-1} (There is 27% difference at these two points, which means the error in reflectance increases with distance from the illumination site and with absorption coefficient). Fig. 48a shows that the reflectance from the illumination-detection fiber is not sensitive to μ_a while μ_s' is smaller than 15 cm^{-1} .



(a) μ_s' is constant



(b) μ_a is constant

Fig. 48 Reflectance of the illumination-detection fiber and other detection fibers from condensed Monte Carlo simulations (hollow symbols) and standard Monte Carlo simulations (solid symbols) at different optical properties

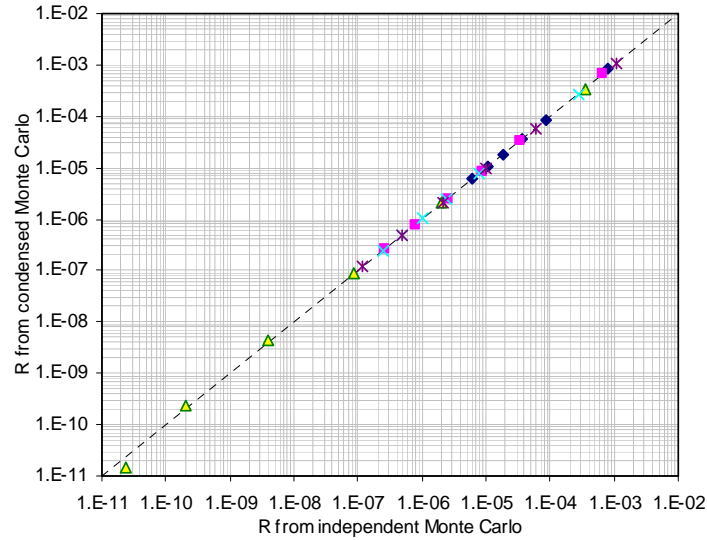


Fig. 49 Reflectance from condensed Monte Carlo simulations versus reflectance from standard Monte Carlo simulations

4.3 Effect of fiber diameter on reflectance from an illumination-detection fiber

Based on condensed Monte Carlo simulations, the logarithmic contour curves of reflectance values from illumination-detection fibers were obtained for fiber radii of 0.05, 0.1, 0.2, 0.3, 0.4, 0.5 and 5 mm. Totally 37 μ_a values ranged from 0.1 cm^{-1} to 40 cm^{-1} and 44 μ_s' values ranged from 0.1 cm^{-1} to 100 cm^{-1} were applied for each fiber size. In other words, 1628 simulations were performed for each contour graph. Fig. 50 shows the results for fiber radii of 0.05, 0.2, 0.5 and 5 mm respectively. Fig. 51 shows the reflectance of four optical property sets as a function of radius.

Fig. 50 indicates that the sensitivity of reflectance to optical properties varies with μ_a and μ_s' (similar contour figures for detection fibers as shown in Fig. 43 are available in Fig. 18). A steeper slope at a point implies that the reflectance is less sensitive to μ_s' at that point. On the other hand, a shallower slope at a point implies that the reflectance is less sensitive to μ_a . The figure shows that reflectance from an illumination-detection fiber is not sensitive to μ_a at low μ_s' values, especially for a fiber with small radius. The same conclusion can also be drawn from the fact that the difference between the two dashed lines is smaller than the difference between the two

solid lines in Fig. 51. Unlike the reflectance from other detection fibers which was not sensitive to μ_s' at all at certain optical ranges as shown in Fig. 18, the reflectance from the illumination-detection fiber is sensitive to μ_s' over the entire optical range of μ_a from 0.1 cm^{-1} to 40 cm^{-1} and μ_s' from 0.1 cm^{-1} to 100 cm^{-1} .

Graphs in Fig. 50 provide quantitative insight into the effect of fiber size on sensitivity of reflectance to optical properties. From Fig. 50, there is an increase in “slope” of the contour lines with fiber radius, which translates to an increase in sensitivity to changes in μ_a , likely due to the greater probability of detecting longer pathlength photons. For example, when μ_a is 10 cm^{-1} and μ_s' changes from 10 cm^{-1} to 30 cm^{-1} , the change in reflectance is 6.9×10^{-4} for the 0.1 mm radius fiber and 1.2×10^{-3} for the 0.2 mm radius fiber. Fig. 51 also shows that bigger fiber size can distinguish the reflectance difference more significantly.

Since the condensed model can be used to build up large data sets such as these, this approach may help to facilitate the development of rapid optical approaches based on extensive “lookup tables” such as that recently proposed by Rajaram et al.¹⁶⁵.

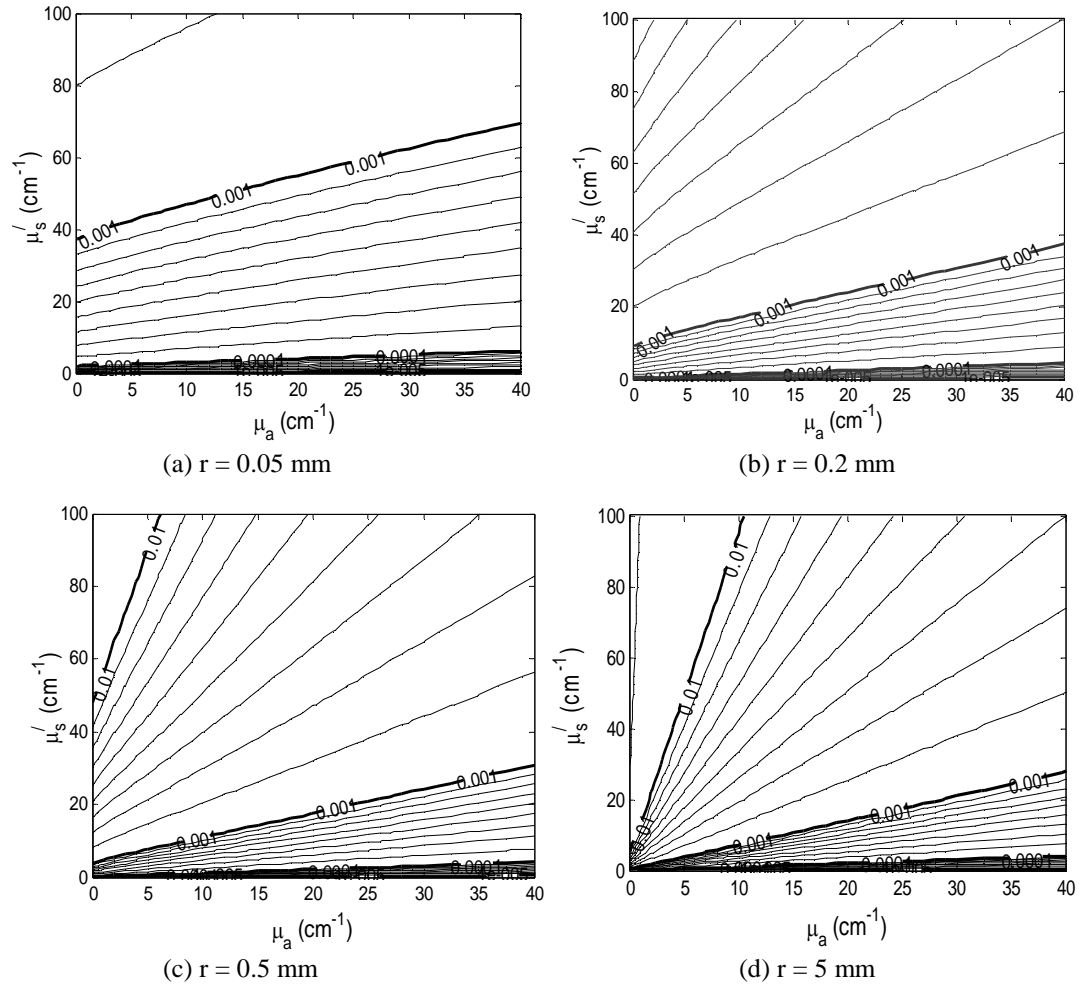


Fig. 50 Contours of dimensionless reflectance from illumination-detection fibers with different radii

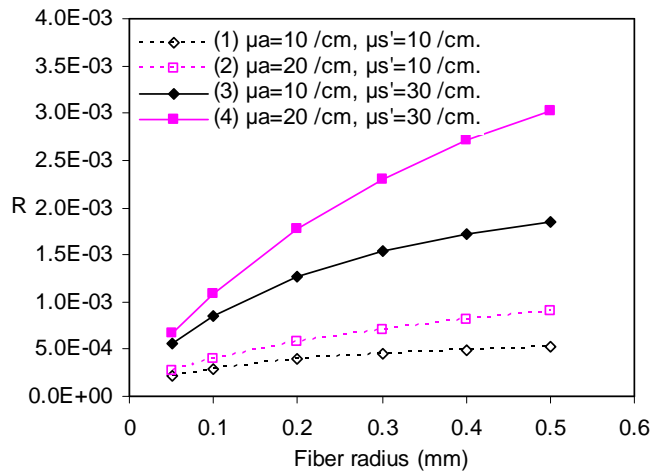


Fig. 51 Reflectance as a function of fiber radius

4.4 Reflectance from an illumination-detection fiber to improve the accuracy of neural network

By applying the condensed Monte Carlo technique, reflectance datasets within a wide range of optical properties in μ_a (0.1-85 cm^{-1}) and μ_s' (0.1-118 cm^{-1}) were generated. In total, 2805 datasets with an even 2.5 cm^{-1} spacing for both μ_a and μ_s' while $\mu_a > 30 \text{ cm}^{-1}$ and $\mu_s' > 5 \text{ cm}^{-1}$ and a smaller spacing while $\mu_a < 30 \text{ cm}^{-1}$ or $\mu_s' < 5 \text{ cm}^{-1}$ were obtained, as well as 220 random datasets. There were 8 values in each dataset - μ_a , μ_s' , reflectance values from five detection fibers, and the reflectance value from an illumination-detection fiber (There was no this value in Chapter 3). The 2805 datasets were used to train and evaluate feed-forward back-propagation neural network models. Each network consisted of an input layer, a hidden middle layer and an output layer. The input data were a matrix of reflectance values. Of the 2805 datasets generated from condensed Monte Carlo simulations, two-thirds were used for training and one-third was used for evaluation during training. The 220 random datasets were used to evaluate the trained neural networks.

In order to evaluate the influence of the illumination-detection fiber and quantity of other detection fibers (*i.e.*, the matrix size of the reflectance datasets as input) for performing optical property estimations with a neural network, two sets of neural network models (NNset1 & NNset2) were generated according to the 2805 datasets. Reflectance values from different fibers were used in different neural network models. NNset1 was based on reflectance values from the illumination-detection fiber and 1, 2, 3, 4 and 5 detection fibers respectively (In other words, there were respectively 2, 3, 4, 5 and 6 reflectance values in the feed in matrix to each neural networks.). NNset2 was based on reflectance values from 2, 3, 4 and 5 detection fibers respectively (In other words, there were respectively 2, 3, 4, and 5 reflectance values in the feed in matrix to each neural networks.). These neural network models were then evaluated with the 220 random datasets from condensed Monte Carlo simulations.

To test the robustness of these neural networks, noise was added to the reflectance values of the 220 random datasets. In Chapter 3, up to 5% random noise was added to the reflectance. For any reflectance R_0 , the feed value to a neural network will be $R = R_0 * (1 + 5\% * Rand)$, where $Rand$ was an evenly distributed random real number greater than -1 and less than 1. However, the noise from an actual optical system may not behave this way. To simulate the actual noise of my optical system, tissue phantoms were constructed from deionized water, polystyrene microspheres (Polybead® Microspheres 1.00 μm , Polysciences, Inc.) and hemoglobin (Hb) (hemoglobin A₀, ferrous stabilized human, Sigma H0267). The reflectance of each phantom was then measured three times with the system. The reflectance values from each detection fiber in each measurement were recorded and their standard deviations were calculated. By analyzing the relationship between the reflectance values and their standard deviations, the noise characteristics of the optical system can be determined. Fig. 52 shows the standard deviation characteristics of the optical system. The figure shows that the standard deviation has a power relation with the reflectance:

$$SD = 0.00027 * R_0^{0.85} \quad (26)$$

where SD is standard deviation and R_0 is reflectance. This standard deviation might be the results of noise from the CCD camera, shot noise and laser noise from the system. Therefore, noise can be added to the reflectance with following equation

$$R = R_0 + SD * RandN \quad (27)$$

where R is the reflectance with noise and $RandN$ is a random number drawn from a normal distribution with mean zero and deviation one.

Table 6 summarizes the absolute errors from the evaluations. From this table, the absolute errors of optical properties from NNset2 decrease with an increasing number of detection fibers except for the five-fiber network which shows similar accuracy with the four-fiber network. This is likely because the greater noise in reflectance at high μ_a and μ_s' for fiber No.5 renders the reflectance from detection fiber No.5 of little use. On the

other hand, the absolute errors of optical properties from NNset1 have almost the same level of error for all the neural networks and the level is significantly less than that from NNset2, which means accurate optical properties can be extracted just from the reflectance of the illumination fiber and one separate detection fiber. However, at least three fibers (one illumination and two detection fibers) are needed to measure optical properties if the illumination fiber does not measure reflectance signal. Probe with less optical fibers could be coupled into an endoscope easier.

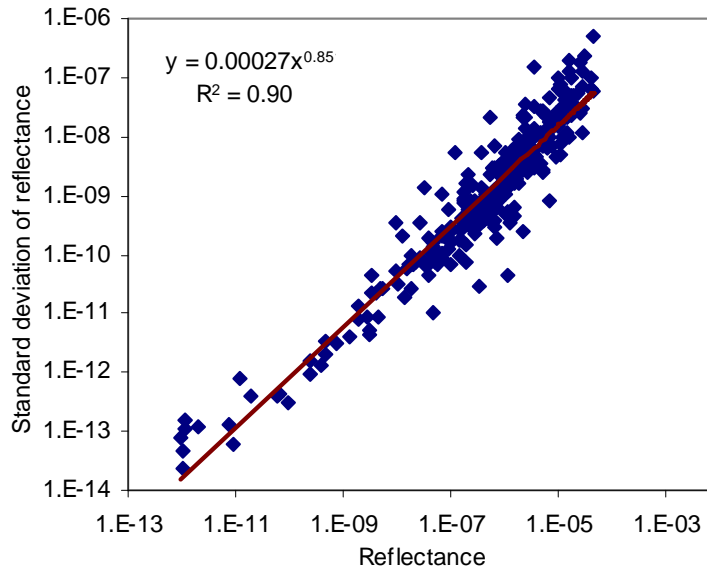


Fig. 52 Standard deviation of reflectance with trend line

Table 6. Absolute errors of neural networks (cm^{-1})

Illumination fiber used for detection?	Number of detection fibers except the illumination fiber									
	1		2		3		4		5	
	μ_a	μ_s'	μ_a	μ_s'	μ_a	μ_s'	μ_a	μ_s'	μ_a	μ_s'
Yes (NNset1)	0.03	0.06	0.03	0.06	0.03	0.06	0.03	0.06	0.03	0.06
No (NNset2)	-	-	0.32	0.41	0.39	0.38	0.22	0.28	0.24	0.25

4.5 Reflectance spectra of breast tissues from illumination-detection fibers

Any structural and biochemical changes associated with abnormal changes in a tissue will result in its optical property changes, which will in turn result in the changes of

reflectance spectroscopy. Because of its fast speed, the condensed Monte Carlo method I developed can help us to quantitatively understand the specific contributions of changes in optical properties by a pre-cancer to the overall spectral response. Parameters and details in the primary MC simulation were the same as those in our previous paper⁴⁰.

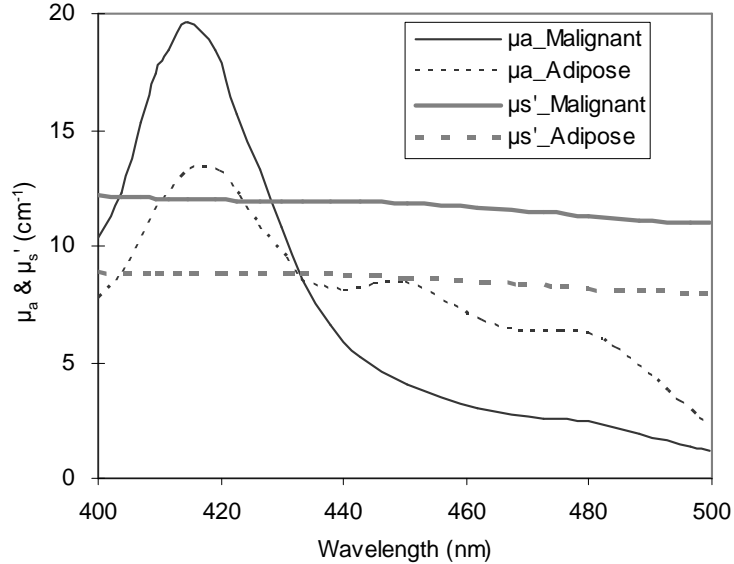
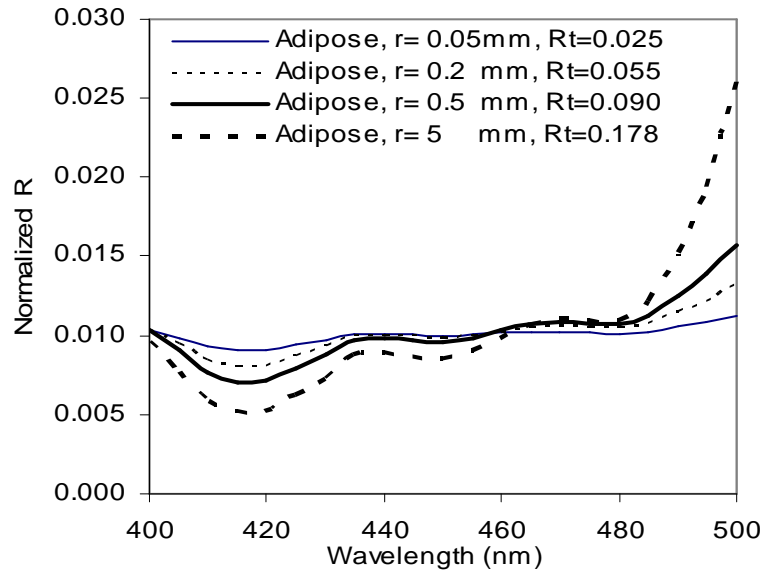


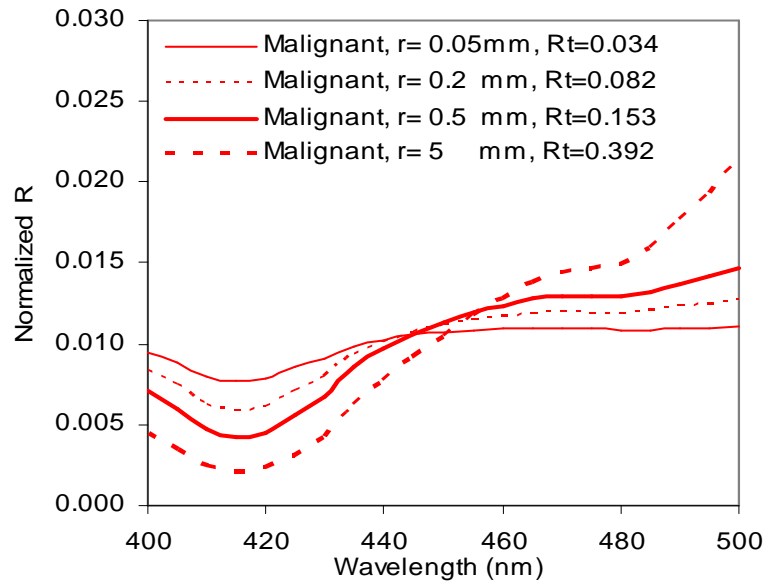
Fig. 53 Optical properties of breast tissue from literature

The reflectance spectra of adipose and malignant breast tissues were simulated with condensed Monte Carlo model according to the μ_a and μ_s' data as shown in Fig. 53 from a prior paper¹⁶⁶. The μ_a and μ_s' data were read every 5 nm from 400 nm to 500nm from the paper. The influence of fiber radius on reflectance spectra of the adipose tissue was also studied. Fig. 54 shows the reflectance spectra of adipose and malignant breast tissues for illumination-detection fibers with radii of 0.05, 0.2, 0.5 and 5 mm. The 5 mm radius fiber is to simulate an imaging probe which can collect more reflectance signal and detect deeper into tissues. Each reflectance spectrum was normalized to the total detected reflectance, Rt . Increasing fiber radius tended to exaggerate local maxima and minima and increase collection efficiency. The former effect is similar to that seen for multiple fiber probes at different separation distances and most likely due to increased sensitivity to longer photon trajectories, which are more strongly affected by absorption. While spectra calculated for adipose and malignant tissues both show the effects of strong HbO₂

absorption near 415 nm, significant differences exist between these tissue types. Fig. 55 shows the percentage change of reflectance of malignant breast tissue compared with that of adipose breast tissue. The figure shows that larger radius fibers increased the percentage change which may help to distinguish small changes in a tissue.



(a)



(b)

Fig. 54 Reflectance spectra of adipose and malignant breast tissues from illumination-detection fibers

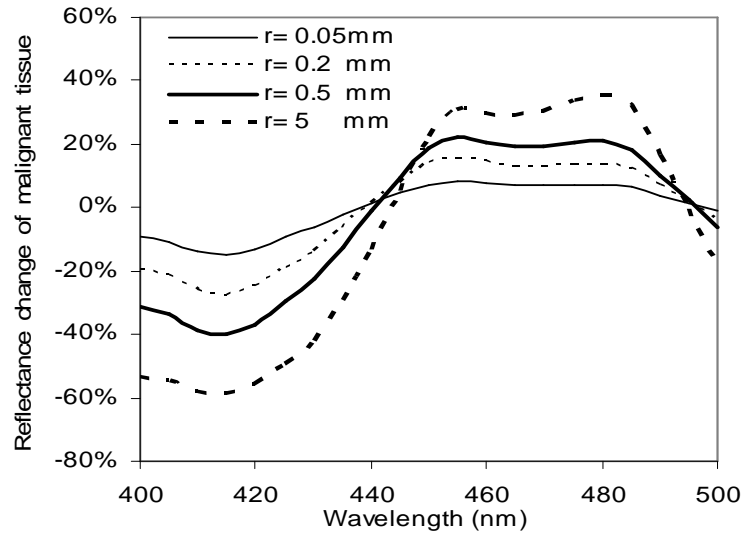


Fig. 55 Percentage change of reflectance of malignant breast tissue

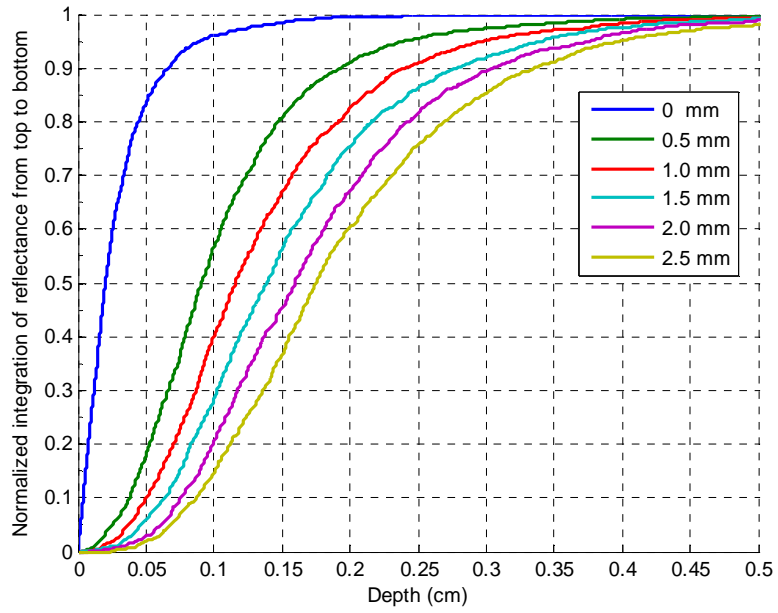
4.6 Maximum penetration depth of a photon and detection depth of a fiber

It is known that the signal detected at a location further from the illumination point usually travels a longer distance and penetrates deeper in the tissue. While some researchers have engaged in the depth-resolved fluorescence measurement with fiberoptic probes^{162, 163, 167}, the study about depth-resolved reflectance detection with a fiberoptic probe is insufficient. Papaioannou *et al.* have investigated effects of fiber-optic probe design and probe-to-target distance on diffuse reflectance measurements. They got the internal flux distributions of photons collected in the form of contours.¹⁵⁶ Amelink *et al.* developed a differential path-length spectroscopy which included an illumination-detection fiber and was sensitive to the optical properties in the most superficial layer of the tissue.¹⁰⁷ However, they did not study the probing depth. Moffitt *et al.* constructed a sized-fiber reflectometry for measuring local optical properties. They showed a few data about the depth where an absorbing plane embedding in a phantom absorbed 50% of the reflectance signal. However, these data only show a specific case and is not a profound study about probing depth.¹⁰⁸

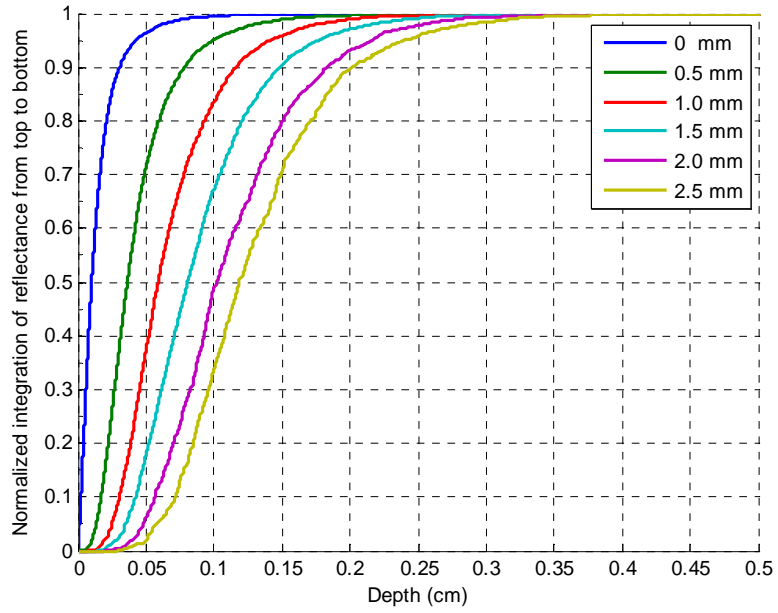
In this section, I systematically study the detection depth by both illumination-detection fibers and detection fibers. The method of expressing detection depth by the

maximum penetration depth of detected photons was investigated with the condensed Monte Carlo model. Weiss *et al.* introduced the idea of penetration depth with a statistical method on the basis of a lattice random-walk model¹⁶⁸. Their results showed that the average of the maximum depth probed by photons that exit the media at a distance r from the illumination point had a linear relationship with $r^{1/2}$ at sufficiently great r value. While being a pioneer study, this research only focus on the average of the maximum penetration depth and the so called ‘sufficiently great r value’ is not a precise definition. Besides, they did not prove that this conclusion held true for all optical ranges.

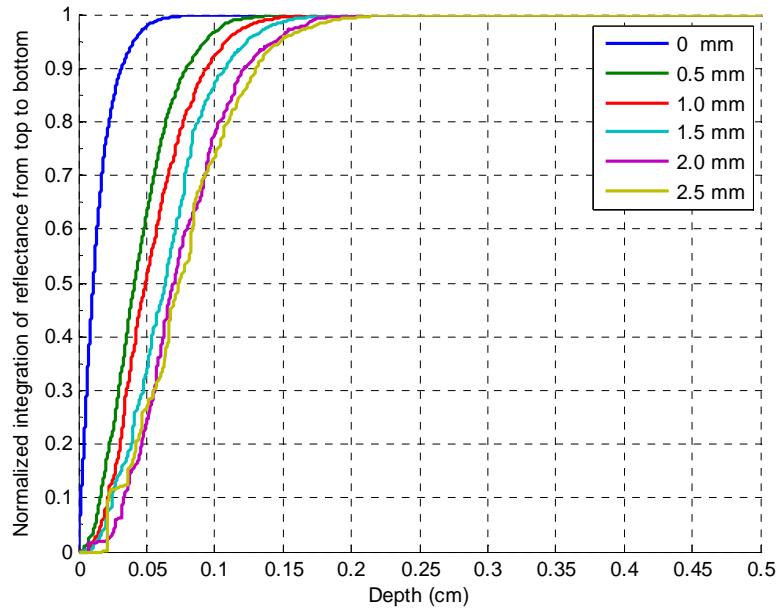
In my simulations, new convolution equations for the illumination-detection fiber (Eq. 23 and Eq. 24) and scaling equation for maximum probing depth (Eq. 25) were coupled with the condensed Monte Carlo simulation based on our initial study⁴⁰. The parameters in simulations are the same as those in Chapter 3 except those otherwise specified. For each escaping photon which was governed by the acceptance angle, its maximum penetration depth (d_{sim}) was recorded besides the number of interactions with scatterers (N), the distance from illumination point to exiting point (r_{sim}), and its weight (W_{sim}). To simulate a medium with new absorption coefficient ($\mu_{a,new}$) and scattering coefficient ($\mu_{s,new}$), scaling was performed for each photon to obtain new maximum penetration depth (d_{new}), new distance from illumination point to exiting point (r_{new}) and new weight of the remitted photon (W_{new}) according to scaling equations. Convolution equations were used to calculate the possibility that an escaping photon was detected by a fiber. The probe geometry was same as shown in Fig. 43. After scaling and convolution calculation, the new database was sorted based on d_{new} in ascending order. W_{new} was then numerically integrated with d_{new} and normalized to the maximum value and shown as a function of depth. Fig. 56 shows the simulation results in four different optical property ranges: low- μ_a -low- μ_s' , low- μ_a -high- μ_s' , high- μ_a -low- μ_s' and high- μ_a -high- μ_s' .



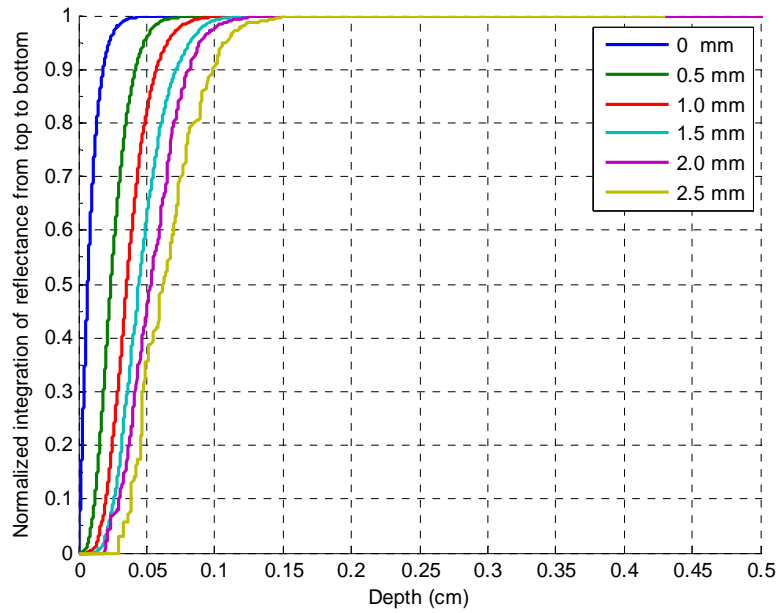
(1) $\mu_a=1 \text{ cm}^{-1}, \mu_s'=5 \text{ cm}^{-1}$



(2) $\mu_a=1 \text{ cm}^{-1}, \mu_s'=35 \text{ cm}^{-1}$



(3) $\mu_a=20 \text{ cm}^{-1}, \mu_s'=5 \text{ cm}^{-1}$



(4) $\mu_a=20 \text{ cm}^{-1}, \mu_s'=35 \text{ cm}^{-1}$

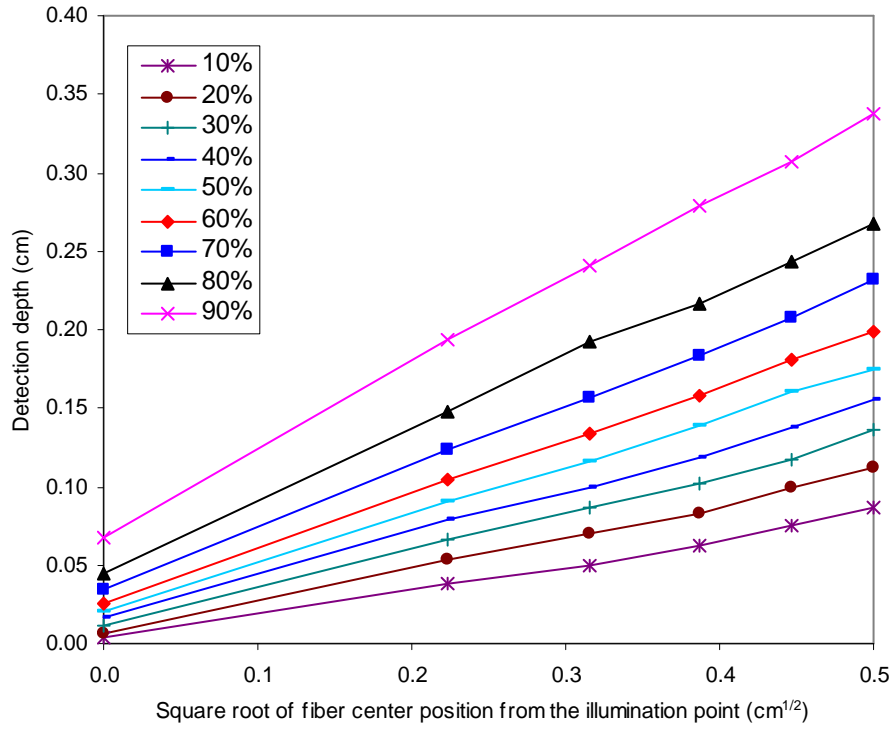
Fig. 56 Percentage detection depth of as a function of maximum penetration depth (Legends in graphs are the center positions of detection fibers from the illumination point. The radius of each fiber is 0.1 mm.)

Fig. 56 shows the normalized integration of reflectance from top to bottom as a function of maximum penetration depth. Similar with depth-resolved fluorescence

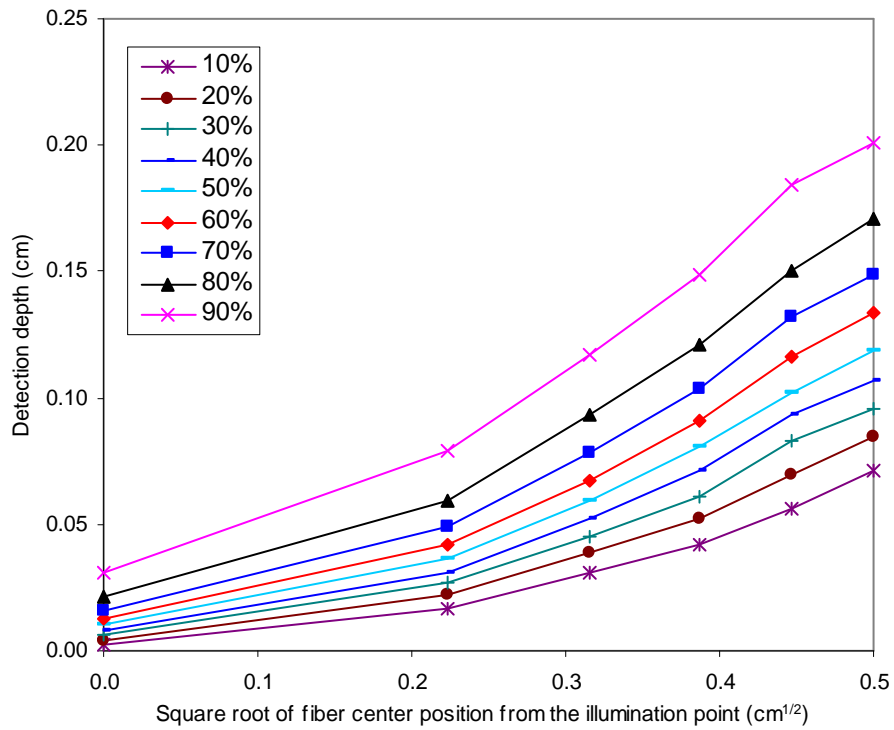
study^{163, 167, 169}, we defined a percentage detection depth of diffuse reflectance. A 90% detection depth was defined as the largest value of the maximum penetration depth that 90% of the total detected photon (in term of weight) can penetrate, *etc.* From Fig. 56, the detection depth of any percentage can be read. In general, the detection depth decreases with increasing μ_a or μ_s' value. Fig. 56(1) and (3) implies that the detection depth by the illumination-detection fiber is significant shallower than other detection fibers when μ_s' is low. Table 7 shows some data read from Fig. 56. Fig. 57 shows detection depth as a function of square root of center position of detection fibers according to Table 7. Weiss *et al.*'s conclusion of "the average of the maximum depth probed by photons that exit the media at a distance r from the illumination point have a linear relationship with $r^{1/2}$ "¹⁶⁸ can be drawn from the curve of 50% detection depth in Fig. 57 (1) which shows the case of low μ_a and low μ_s' values. Even more, this conclusion can be extended to other percentage detection depth. However, this conclusion is not true for other optical property ranges as show in Fig. 57 (2)-(4) since lines in these graphs are not straight.

Table 7. Detection depth of fibers into different tissues (cm)

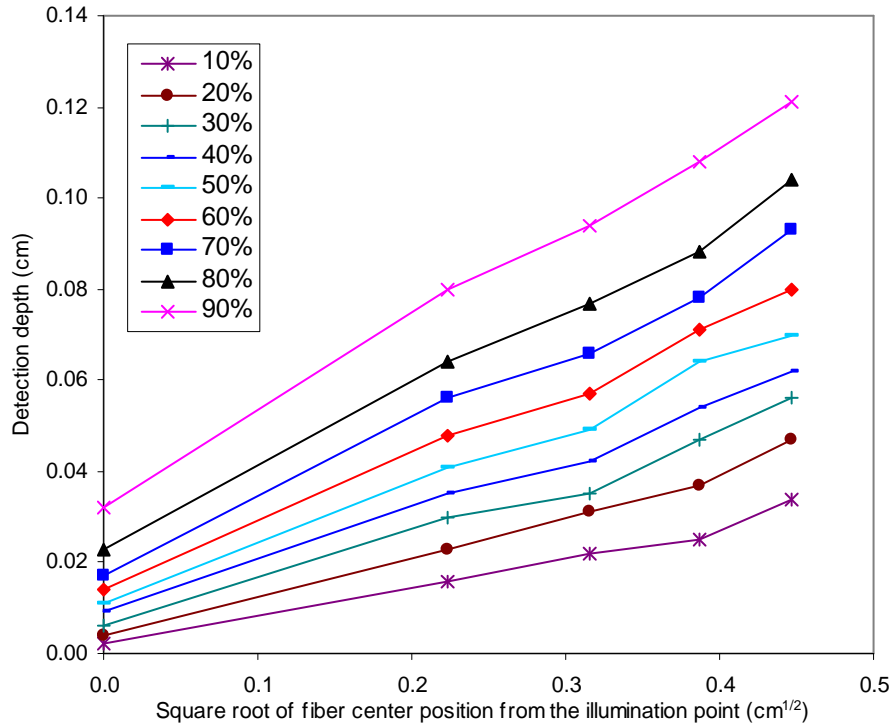
Tissue optical properties (cm ⁻¹)		Fiber center position (mm)	Percentage of detection signal from top to bottom								
			10%	20%	30%	40%	50%	60%	70%	80%	90%
μ_a	μ_s'										
1	5	0	0.004	0.007	0.012	0.016	0.020	0.025	0.034	0.045	0.067
		0.5	0.038	0.053	0.066	0.079	0.091	0.105	0.124	0.148	0.194
		1.0	0.050	0.070	0.087	0.100	0.116	0.134	0.157	0.192	0.241
		1.5	0.063	0.083	0.102	0.119	0.139	0.158	0.183	0.216	0.279
		2.0	0.075	0.099	0.117	0.137	0.160	0.181	0.208	0.243	0.307
		2.5	0.087	0.112	0.136	0.156	0.175	0.199	0.232	0.267	0.337
1	35	0	0.002	0.004	0.006	0.008	0.010	0.013	0.016	0.021	0.031
		0.5	0.017	0.022	0.027	0.031	0.036	0.042	0.049	0.059	0.079
		1.0	0.031	0.039	0.045	0.052	0.059	0.067	0.078	0.093	0.117
		1.5	0.042	0.052	0.061	0.071	0.081	0.091	0.104	0.121	0.149
		2.0	0.056	0.070	0.083	0.093	0.102	0.116	0.132	0.150	0.184
		2.5	0.071	0.085	0.096	0.107	0.119	0.134	0.149	0.171	0.201
20	5	0	0.002	0.004	0.006	0.009	0.011	0.014	0.017	0.023	0.032
		0.5	0.016	0.023	0.030	0.035	0.041	0.048	0.056	0.064	0.080
		1.0	0.022	0.031	0.035	0.042	0.049	0.057	0.066	0.077	0.094
		1.5	0.025	0.037	0.047	0.054	0.064	0.071	0.078	0.088	0.108
		2.0	0.034	0.047	0.056	0.062	0.070	0.080	0.093	0.104	0.121
		2.5	-	-	-	-	-	-	-	-	-
20	35	0	0.001	0.003	0.004	0.005	0.007	0.009	0.011	0.013	0.018
		0.5	0.012	0.015	0.018	0.021	0.024	0.027	0.030	0.035	0.042
		1.0	0.020	0.025	0.029	0.032	0.035	0.039	0.043	0.049	0.057
		1.5	0.026	0.032	0.036	0.040	0.044	0.049	0.054	0.061	0.072
		2.0	0.031	0.037	0.042	0.047	0.053	0.060	0.065	0.071	0.082
		2.5	0.038	0.046	0.047	0.055	0.062	0.069	0.076	0.087	0.099



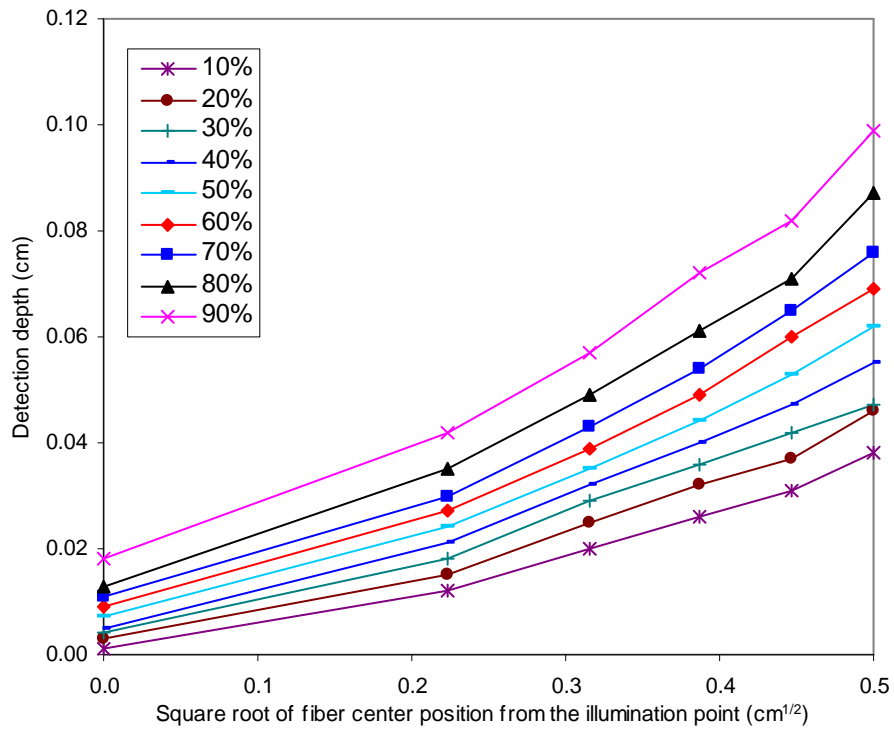
(1) $\mu_a=1 \text{ cm}^{-1}, \mu_s'=5 \text{ cm}^{-1}$



(2) $\mu_a=1 \text{ cm}^{-1}, \mu_s'=35 \text{ cm}^{-1}$



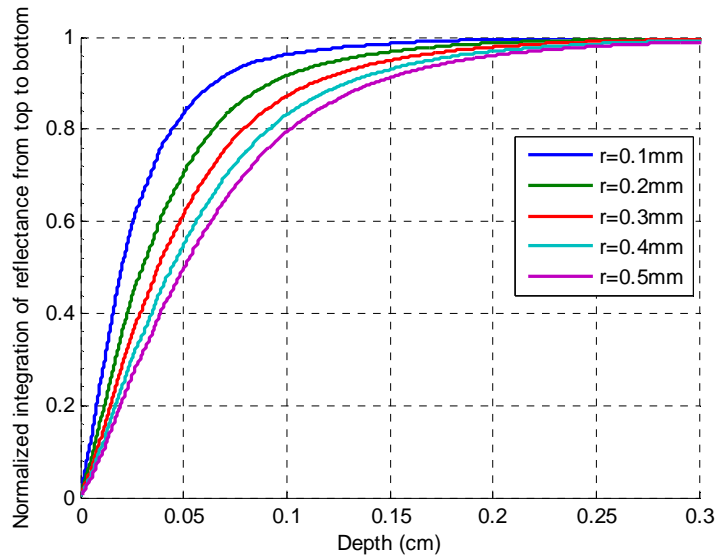
(3) $\mu_a=20 \text{ cm}^{-1}, \mu_s'=5 \text{ cm}^{-1}$



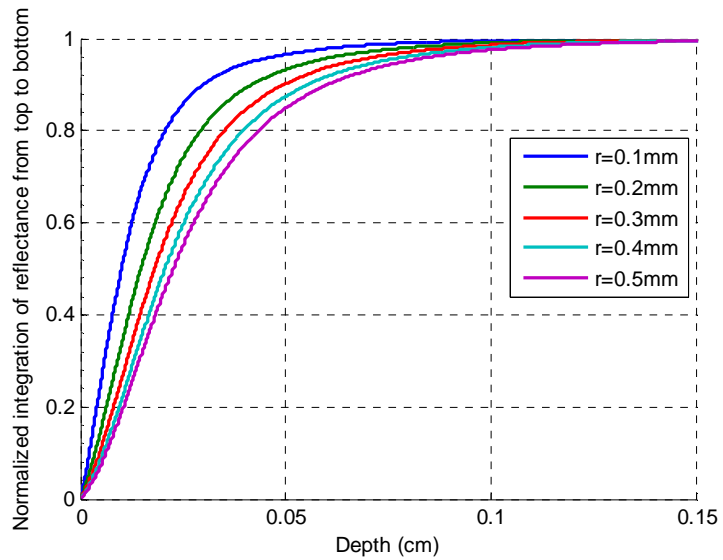
(4) $\mu_a=20 \text{ cm}^{-1}, \mu_s'=35 \text{ cm}^{-1}$

Fig. 57 Detection depth as a function of square root of center position of detection fibers (Center of the illumination fiber is origin.)

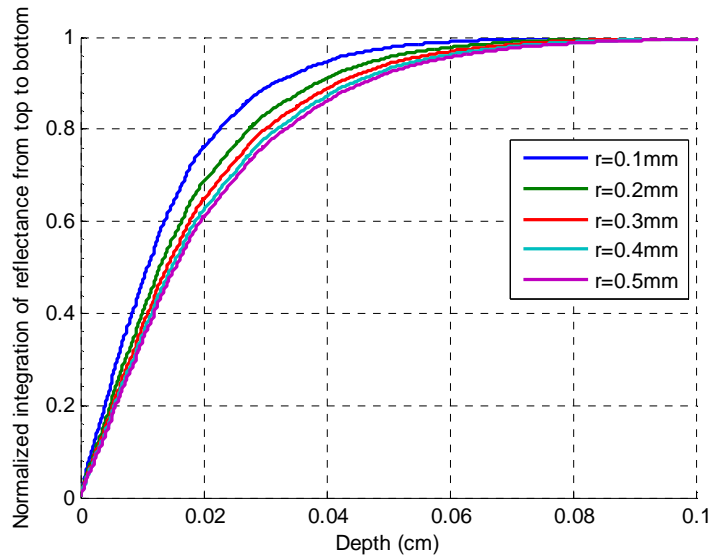
To study the influence of an illumination-detection fiber's size on detection depth, similar simulations as described above were carried out. The only different is that a series of illumination-detection fibers with different sizes were used instead of a fiber probe as shown in Fig. 43. A group of graphs similar with Fig. 56 were obtained as shown in Fig. 58. Again, the simulation results are in four different optical property ranges: low- μ_a -low- μ_s' , low- μ_a -high- μ_s' , high- μ_a -low- μ_s' and high- μ_a -high- μ_s' . From Fig. 58, the detection depth by an illumination-detection fiber increases with increasing fiber size. However, their relation is not linear. The increase of detection depth with increasing fiber size is more significant while the fiber size is smaller. In general, the detection depth by an illumination-detection fiber is small in all the optical ranges. Take the 80% detection depth by an illumination-detection fiber with radius of 0.5 mm as an example: the detection depths as shown in Fig. 58 are 0.104 cm, 0.044 cm, 0.034 cm and 0.021 cm respectively. These small numbers explains why an illumination-detection fiber is idea for optical property measurement of superficial tissues. Graphs in Fig. 58 also show that detection depth is sensitive to optical properties.



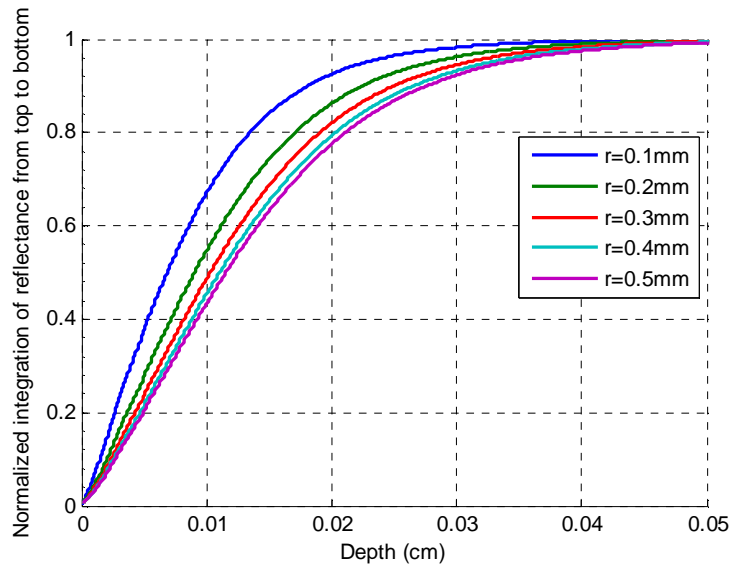
(1) $\mu_a=1\text{ cm}^{-1}$, $\mu_s'=5\text{ cm}^{-1}$



(2) $\mu_a=1\text{ cm}^{-1}$, $\mu_s'=35\text{ cm}^{-1}$



(3) $\mu_a=20 \text{ cm}^{-1}, \mu_s'=5 \text{ cm}^{-1}$



(4) $\mu_a=20 \text{ cm}^{-1}, \mu_s'=35 \text{ cm}^{-1}$

Fig. 58 Percentage detection depths of illumination-detection fibers with different sizes (Legends in graphs are the radii of illumination-detection fibers.)

4.7 Conclusions

In this study I have developed and evaluated two convolution equations for reflectance calculation of an illumination-detection fiber. Simulations with the condensed Monte Carlo model show that:

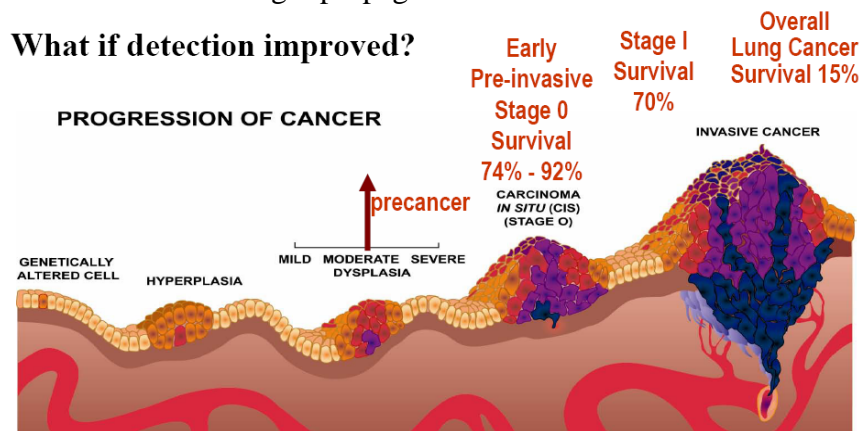
- (1) Reflectance from an illumination-detection fiber is not sensitive to μ_a at low μ_s' values. There is a relative increase in sensitivity to μ_a when the radius of an illumination-detection fiber increases, likely due to the greater probability of detecting longer pathlength photons.
- (2) Neural network results within the optical property range of μ_a up to 85 cm^{-1} and μ_s' up to 118 cm^{-1} show that more accurate optical property results can be obtained if the reflectance values from the illumination-detection fiber are added into the neural network.
- (3) Simulated reflectance spectra indicate that modifications in fiberoptic probe geometry may lead to enhanced discrimination between adipose and malignant breast tissue. Increasing fiber radius tended to exaggerate local maxima and minima and increase collection efficiency. The former effect is similar to that seen for multiple fiber probes at different separation distances and most likely due to increased sensitivity to longer photon trajectories, which are more strongly affected by absorption.
- (4) By introducing the maximum penetration depth into condensed Monte Carlo simulations, I developed the idea of percentage detection depth. For instance, 90% detection depth was defined as the largest value of the maximum depth that 90% of the total detected photon (in term of weight) can penetrate. For any tissue with given optical properties, the detection depth of any percentage number can be quantitatively determined with a condensed Monte Carlo simulation. In general, the detection depth decreases with increasing μ_a or μ_s' value. The detection depth by an illumination-detection fiber is significant shallower than other detection fibers.

- (5) The detection depth by a fiber with a distance r from the illumination point has a linear relationship with $r^{1/2}$ when μ_a and μ_s' are small.
- (6) The detection depth by an illumination-detection fiber increases with increasing fiber size. However, their relation is not linear. The increase of detection depth with increasing fiber size is more significant while the fiber size is smaller. In general, an illumination-detection fiber is idea for optical property measurement of superficial tissues since the detection depth by an illumination-detection fiber is small.

Chapter 5. OPTICAL PROPERTY MEASUREMENT OF LAYERED TISSUES

5.1 Introduction

In prior light-tissue interaction studies, it has often been assumed that the investigated tissue is homogeneous. However, many internal tissues such as esophagus, colon, and bladder consist of two or more layers (Fig. 59). Optical properties from a homogenous model for a layered tissue reflect some bulk or average values of the tissue.¹⁷⁰ However, these optical properties are not accurate values of any specific layer. Since neoplasia originates in the epithelial layer, studying light-tissue interaction in this layer will likely provide insights into early optical detection of neoplasia. On the other hand, complete optical isolation of the epithelial layer is nearly impossible. Therefore, techniques capable of determining the optical properties of multiple tissue layers are needed in order to elucidate light propagation in mucosal tissues.



**Early detection allows early intervention.
Both are key to improved lung cancer survival.**

Fig. 59 Cancer developed from superficial layer

Monte Carlo based models are the most accurate forward models for light propagation in tissues although they are computationally intensive. The methods to increase the efficiency of Monte Carlo modeling include two categories: the methods

accelerating a single Monte Carlo simulation and the methods taking advantage of information generated by a small set of Monte Carlo primary simulations (also called baseline simulations).¹²⁴ Of the two groups, the latter has the advantage of faster speed for a number of simulations. Two representative methods of the second group are perturbation method^{148, 171} and multi-layer scaling method¹²⁴.

The perturbation method begins with a primary Monte Carlo simulation of a multi-layer tissue and records the number of collisions and the total path length of each photon in each layer, from which the photon weight from tissues with different optical properties can be calculated through a perturbation equation. The limitation of perturbation method is that it is only effective over a range of absorption (50 - 400% of baseline values) and scattering (70-130% of baseline values) perturbations¹⁴⁸. When a neoplasia develops in a tissue, the scattering property change can be far beyond this range. Collier *et al.* reported that μ_s of normal cervical tissue was 22 cm^{-1} while μ_s of cervical intraepithelial neoplasia III was 117 cm^{-1} .⁴⁶ Therefore, the perturbation method may not be valid for many tissue conditions.

The multi-layer scaling method begins with a primary Monte Carlo simulation of a homogeneous tissue with tens of imaginary layers, in which the exit weight, the x and y offsets and the number of collisions of each photon in each layer were recorded. From the primary simulation data, the trajectory information of photons in multi-layer tissues is derived through several scaling equations. The computer requirement is high for the scaling method since huge amounts of data need to be processed and stored.

Optical properties of layered tissues such as mucosa at ultraviolet and visible wavelengths are needed to elucidate light propagation mechanisms involved in optical spectroscopy devices. Prior approaches to measuring this data have typically been based on spatially-resolved reflectance. However, these approaches have limitations, some of which are not well understood. Therefore, the objectives of this study were (1) to elucidate the relationship between spatially-resolved reflectance distributions and optical

properties in two-layer tissue and (2) introduce and assess an unconstrained approach to optical property measurement. The first part of this study involved calculating reflectance from two-layer tissue for a wide variety of optical property combinations ($\mu_a = 1-22.5$, $\mu_s' = 5-42.5 \text{ cm}^{-1}$) using a Monte Carlo scaling technique. Subsequently, a Neural Network inverse model trained with the aforementioned results was evaluated using simulated reflectance data. This relationship between optical properties and reflectance provides fundamental insights into the strengths, weaknesses and potential limitations of strategies for optical property measurement based on spatially-resolved reflectance.

5.2 Multi-layer Monte Carlo simulation

Multi-layer Monte Carlo model is similar with single layer Monte Carlo model. The main difference is that the program should judge whether a photon will cross the interface between two layers and calculate the new direction and step size when the crossing occurs. Although the simulation speed of multi-layer Monte Carlo is relative low, it is still essential to develop an accurate program to evaluate the simulation results of other methods. Also, such an accurate program is the fundament of Monte Carlo based fast simulation.

A Matlab program was constructed to do the multi-layer Monte Carlo simulations. The results of one simulation are shown in Fig. 60 and Fig. 61. Parameters of this simulation are shown in Table 8. In the simulation, 2,000,000 photons were launched vertically into the tissue. The Henyey-Greenstein phase function was used to mimic the scattering angle. All the escaped photons were detected.

Table 8. Monte Carlo simulation parameters of a 3-layer tissue

	Top layer	Middle layer	Bottom layer
n	1.37	1.37	1.37
$\mu_a \text{ (cm}^{-1}\text{)}$	1	1	2
$\mu_s \text{ (cm}^{-1}\text{)}$	100	10	10
g	0.9	0	0.7
Thickness (cm)	0.1	0.1	0.2

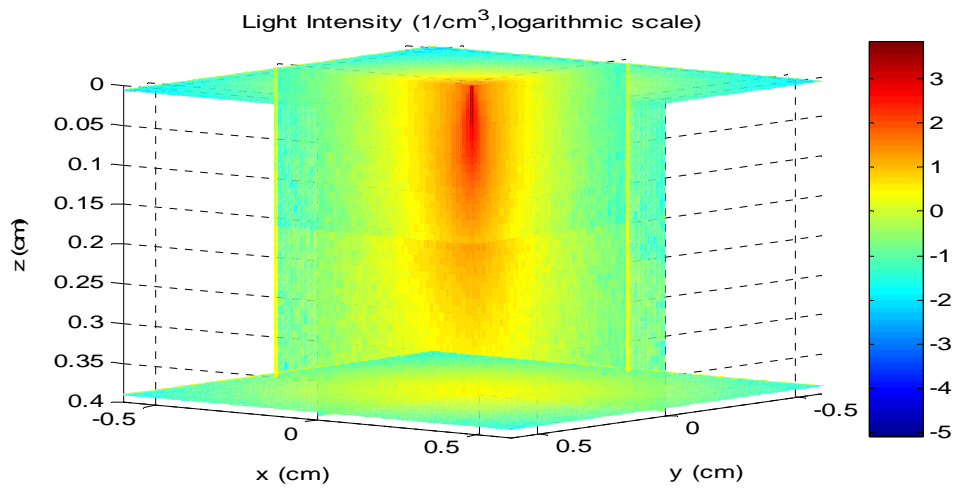


Fig. 60 3-D simulation results of a 3-layer tissue

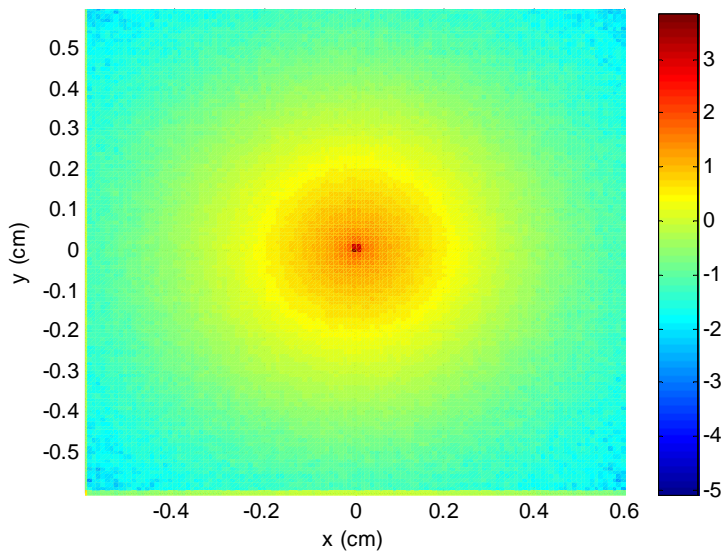


Fig. 61 Reflectance signal on top of a 3-layer tissue

To verify the accuracy of this multi-layer Monte Carlo model, a simulation was run with the same parameters as in literature^{137, 172} and their results were compared (Fig. 62 and Fig. 63). From these figures, both simulation curves overlap the curves from literatures, which imply the accuracy of the multi-layer Monte Carlo program.

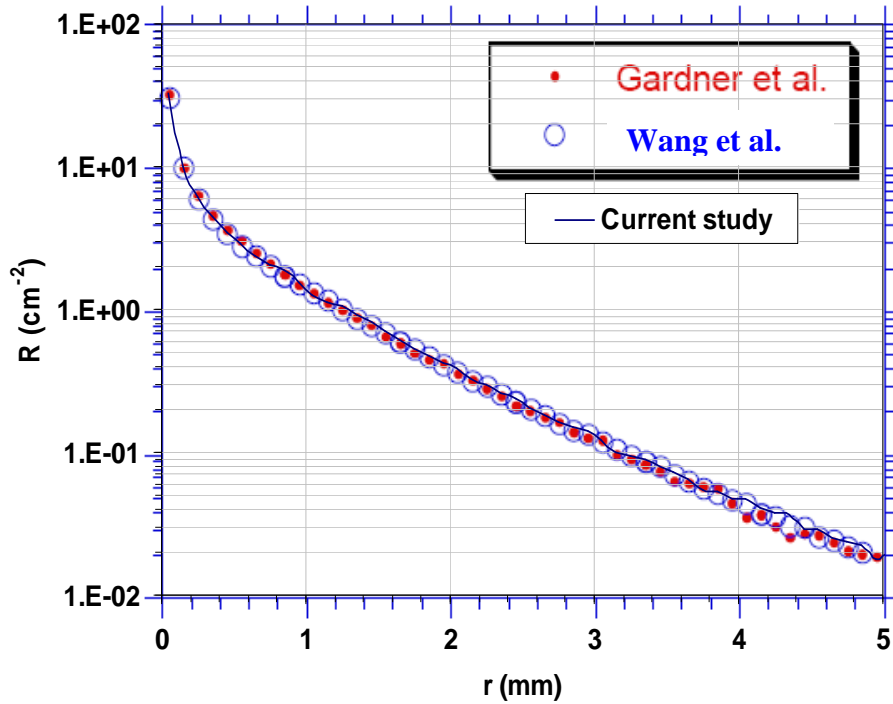


Fig. 62 Diffuse reflectance as a function of radius in a 3-layer Monte Carlo simulation

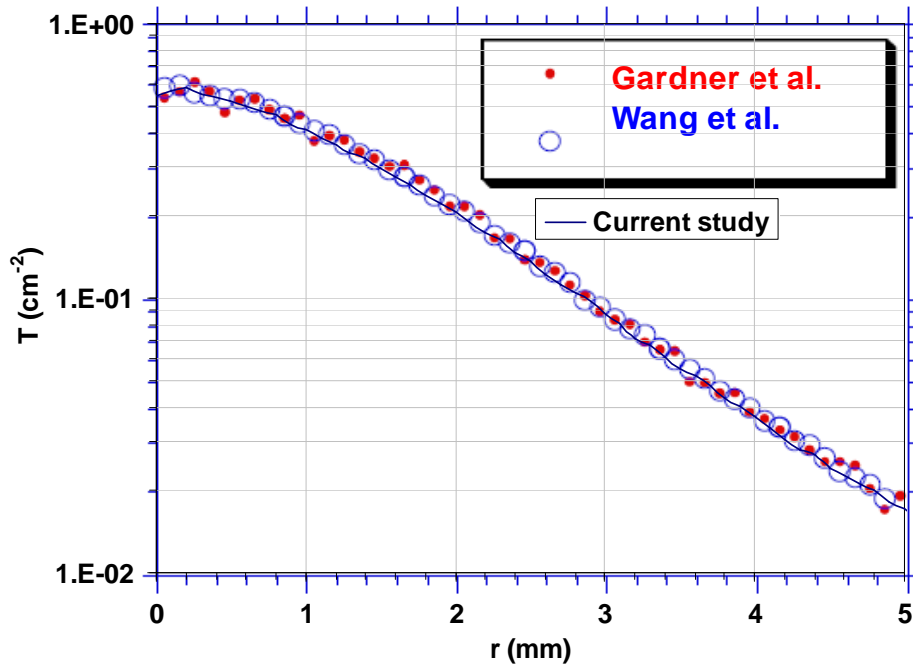


Fig. 63 Transmittance as a function of radius in a 3-layer Monte Carlo simulation

5.3 Multi-layer fast Monte Carlo simulation

The multi-layer fast Monte Carlo simulation¹²⁴ is similar with the scaling method for a single-layer tissue described in Section 3.3 of Chapter 3. The main

difference is that more data must be recorded in the primary Monte Carlo simulation and the scaling equation must be applied in each layer. In the current study, a primary simulation was run at first, in which the Henyey-Greenstein phase function was used to simulate the scattering angles. The baseline medium was homogeneous and semi-infinite with optical properties of μ_{a0} , μ_{s0} and g and was divided into N_{layer} fundamental layers as shown in Fig. 64. A total of N_{photon} photons were launched. For each photon, its exit weight (w_0), its x offset (x_a, x_b, \dots), y offset (y_a, y_b, \dots) and the number of collisions (N_a, N_b, \dots) within each fundamental layer were recorded. To calculate the exit position and exit weight of this photon out of an n-layer tissue with total attenuation coefficient of ($\mu_{t1}, \mu_{t2}, \dots, \mu_{tn}$), albedo of ($\alpha_1, \alpha_2, \dots, \alpha_n$), the thickness of each layer (d_1, d_2, \dots, d_n) should be converted to thicknesses of pseudolayers (d_1', d_2', \dots, d_n') corresponding to the baseline medium according to following equations:

$$\begin{aligned}
 d_1' &= d_1 \times \mu_{t1} / \mu_{t0} \\
 d_2' &= d_2 \times \mu_{t2} / \mu_{t0} \\
 &\dots \\
 d_n' &= d_n \times \mu_{tn} / \mu_{t0}
 \end{aligned} \tag{28}$$

Fundamental layers can then be classified into n groups, each corresponding to a pseudolayer layer thickness of the n-layer tissue (Fig. 64). The photon's x offset (x_1, x_2, \dots), y offset (y_1, y_2, \dots) and the number of collisions (N_1, N_2, \dots) within each pseudolayer are the sum of these values of each group of fundamental layers. The horizontal exit distance of the photon out the layered tissue (r) can be calculated according to following scaling equations:

$$\begin{aligned}
 x &= \sum_{i=1}^n (x_i \frac{\mu_{t0}}{\mu_{ti}}) \\
 y &= \sum_{i=1}^n (y_i \frac{\mu_{t0}}{\mu_{ti}}) \\
 r &= \sqrt{x^2 + y^2}
 \end{aligned} \tag{29}$$

The exit weight of the photon out of the layered tissue (w) can be calculated according to

$$w = w_0 \cdot \prod_{i=1}^n \left(\frac{\alpha_i}{\alpha_0} \right)^{N_i} \quad (30)$$

According to r and w values of all the exit photons, the reflectance values at different positions and by different fiber geometries can be calculated with the same convolution equation in Chapter 3 (Eq.15 and Eq.16) by substituting r_{new} with r and w_{new} with w . To calculate reflectance value from an illumination-detection fiber (*i.e.* the illumination fiber is also a detection fiber), I developed two new convolution equations to calculate the probability⁴⁰ that a photon launched from a fiber will be collected by the same fiber after traveling a net distance r_t (where r_i is the radius of the fiber):

$$p = \left(\frac{r_i - r_t}{r_i} \right)^2 + \frac{2}{\pi \cdot r_i^2} \int_{r_i - r_t}^{r_i} \cos^{-1} \left[\frac{r_t^2 + x^2 - r_i^2}{2 \cdot x \cdot r_t} \right] \cdot x \cdot dx, \quad \text{if } 0 < r_t \leq r_i \quad (31)$$

$$p = \frac{2}{\pi \cdot r_i^2} \int_{r_i - r_t}^{r_i} \cos^{-1} \left[\frac{r_t^2 + x^2 - r_i^2}{2 \cdot x \cdot r_t} \right] \cdot x \cdot dx, \quad \text{if } r_i < r_t \leq 2r_i \quad (32)$$

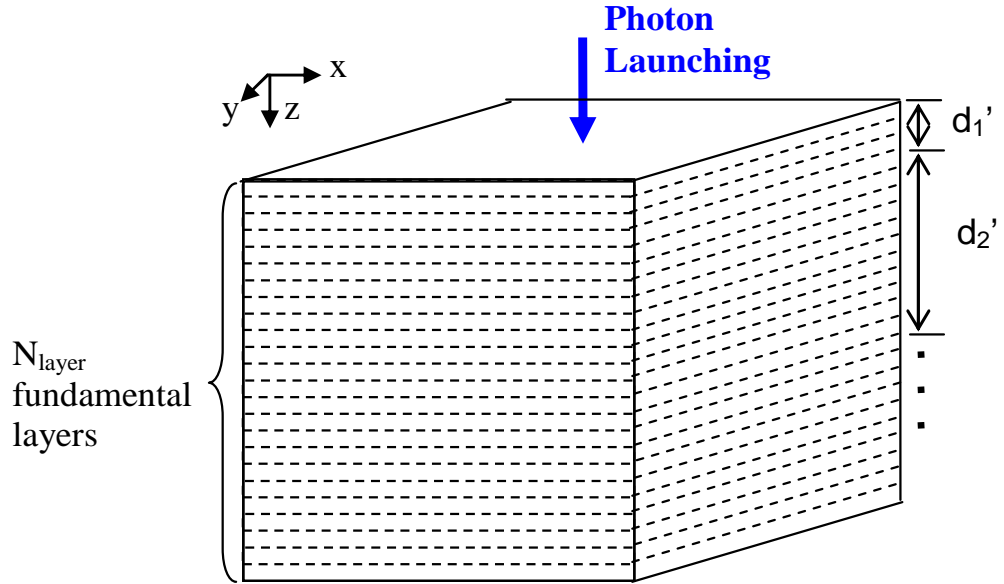


Fig. 64 Baseline simulation and number of fundamental layers corresponding to each layer in a layered tissue

In my study, the homogeneous baseline medium used for the primary Monte Carlo simulation had optical properties of $\mu_{a0}=1 \text{ cm}^{-1}$, $\mu_{s0}=100 \text{ cm}^{-1}$, and $g=0.9$. The index of refraction (n) of the fibers was 1.46 and $n=1.34$ for the tissue. The core diameter

for both the illumination and collection fibers was 0.2 mm. In the baseline simulation 6,000,000 photons were launched in a uniform distribution over angles within the cone specified by $NA=n\cdot\sin\theta$, where θ is the incident/acceptance angle measured from the normal to the tissue surface and NA is the numerical aperture of fiber. $NA=0.22$ in my simulations. The Henyey-Greenstein phase function was used to mimic the scattering angle. Fig. 65 shows the results comparison between an standard Monte Carlo simulation as described in Section 4.2 and a scaling Monte Carlo simulation of a 2-layer tissue. The tissue parameters are shown in Table 9. The well matched results in Fig. 65 provide evidence that the scaling Monte Carlo method is as accurate as the standard Monte Carlo method while the calculation speed is improved two orders of magnitude.

Table 9. Monte Carlo simulation parameters of a 2-layer tissue

	Top layer	Bottom layer
n	1.34	1.34
μ_a (cm^{-1})	2.3	7.0
μ_s (cm^{-1})	86.8	242.5
g	0.9	0.9
Thickness (cm)	0.05	50.1

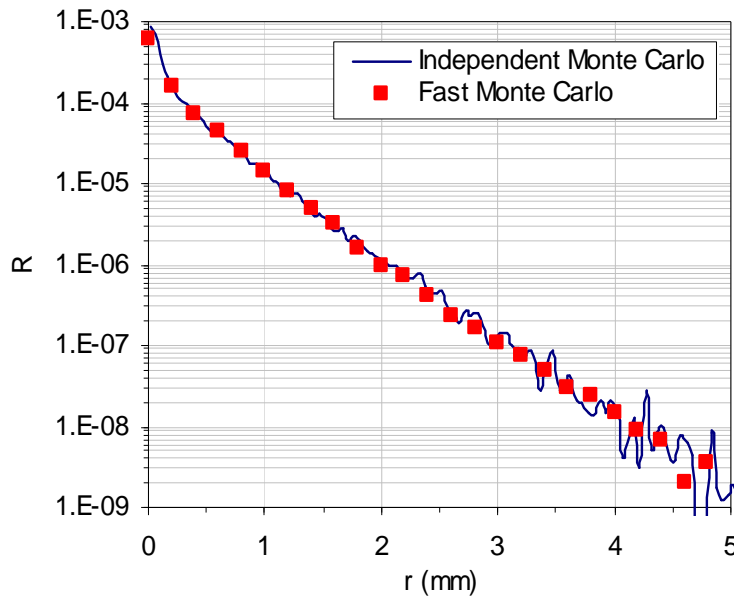


Fig. 65 Comparison of standard Monte Carlo results and scaling Monte Carlo results

5.4 Influence of optical properties of each layer on reflectance

Most mucosal tissues consist of two layers (e.g., epithelial and stromal layers in cervical tissue). Since most cancers originate in the epithelial layer, any change of reflectance signal may come from a tumor in this layer. Therefore, the multi-layer fast Monte Carlo model discussed above was employed to study the influence of top layer and bottom layer optical properties on reflectance. Since the thickness of the epithelial layer of a mucosal tissue ranges from 25 to 750 μm ^{52, 124, 173}, we used a top layer thickness of 0.2 mm. Reflectance from an illumination-detection fiber and twelve detection fibers was simulated with the multi-layer fast Monte Carlo model developed. Center-to-center distances of the twelve detection fibers from the illumination detection fiber were 0.25, 0.50, 0.75, 1.00, 1.25, 1.50, 1.75, 2.00, 2.25, 2.50, 2.75 and 3.00 mm respectively. Radius of all the fibers was 0.1 mm. Four sets of simulations were designed to isolate the effect of four parameters: top layer μ_a , top layer μ_s' , bottom layer μ_a and bottom layer μ_s' (designated as $T\mu_a$, $T\mu_s'$, $B\mu_a$ and $B\mu_s'$ in the following tables and graphs). In each set of simulations, the influence of each parameter on reflectance was investigated with eight simulations in different ranges of the other three parameters. Parameter details in each simulation are list in Table 10.

Table 10. Parameters of fast Monte Carlo simulations

		1	2	3	4	5	6	7	8		1	2	3	4	5	6	7	8
Change top μ_a	$T\mu_a$	V	V	V	V	V	V	V	V	Change top μ_s'	L	H	L	H	L	H	L	H
	$T\mu_s'$	L	H	L	H	L	H	L	H		V	V	V	V	V	V	V	V
	$B\mu_a$	H	H	L	L	H	H	L	L		H	H	L	L	H	H	L	L
	$B\mu_s'$	L	L	L	L	H	H	H	H		L	L	L	L	H	H	H	H
Change bottom μ_a	$T\mu_a$	H	H	L	L	H	H	L	L	Change bottom μ_s'	L	H	L	H	L	H	L	H
	$T\mu_s'$	L	H	L	H	L	H	L	H		L	L	L	L	H	H	H	H
	$B\mu_a$	V	V	V	V	V	V	V	V		H	H	L	L	H	H	L	L
	$B\mu_s'$	L	L	L	L	H	H	H	H		V	V	V	V	V	V	V	V

Note: 'V' means varying values. For $T\mu_a$ and $B\mu_a$, 'L' represents low value of 1 cm^{-1} and 'H' represents high value of 20 cm^{-1} . For $T\mu_s'$ and $B\mu_s'$, 'L' represents low value of 5 cm^{-1} and 'H' represents high value of 35 cm^{-1} .

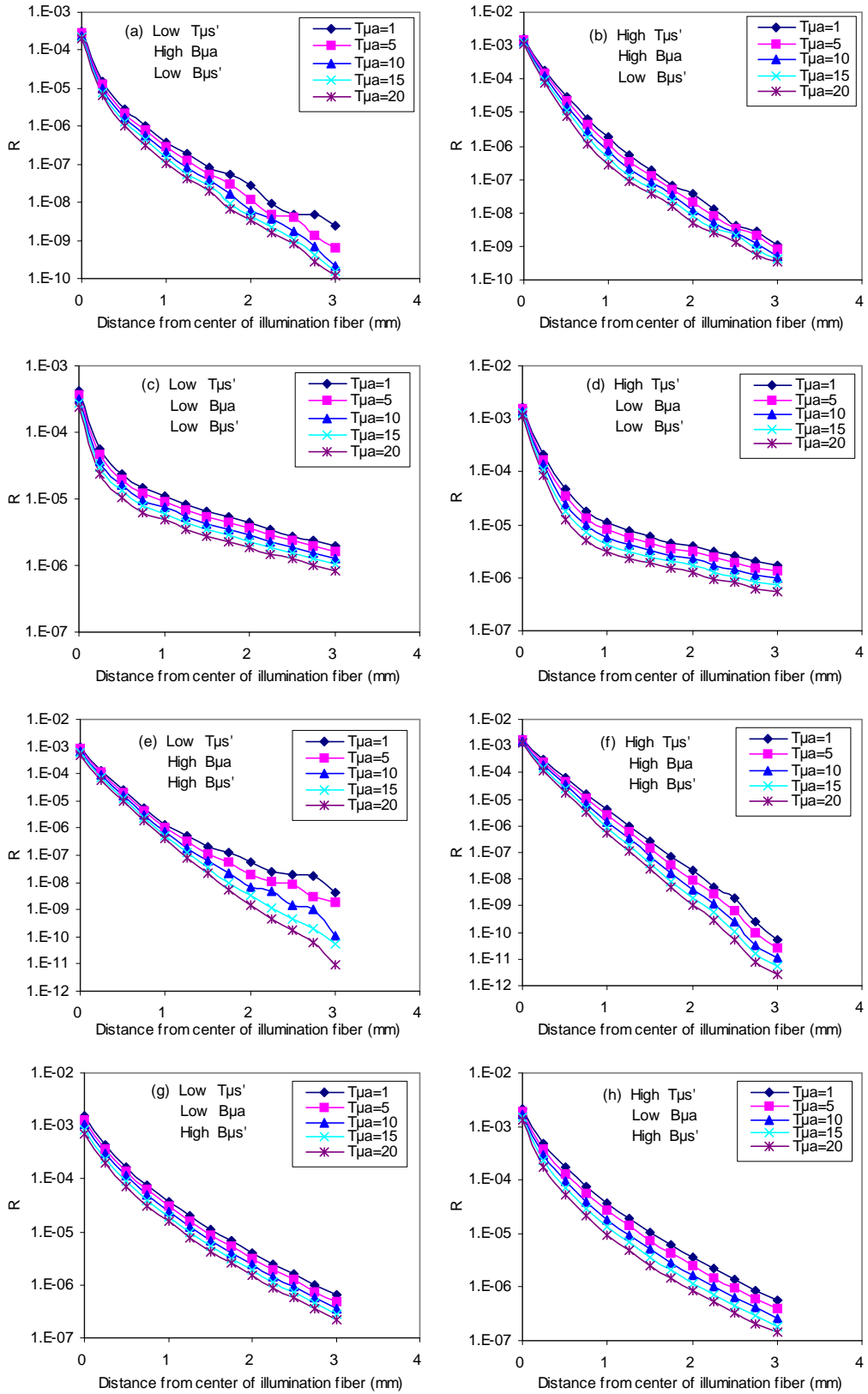


Fig. 66 Influence of top layer μ_a on reflectance

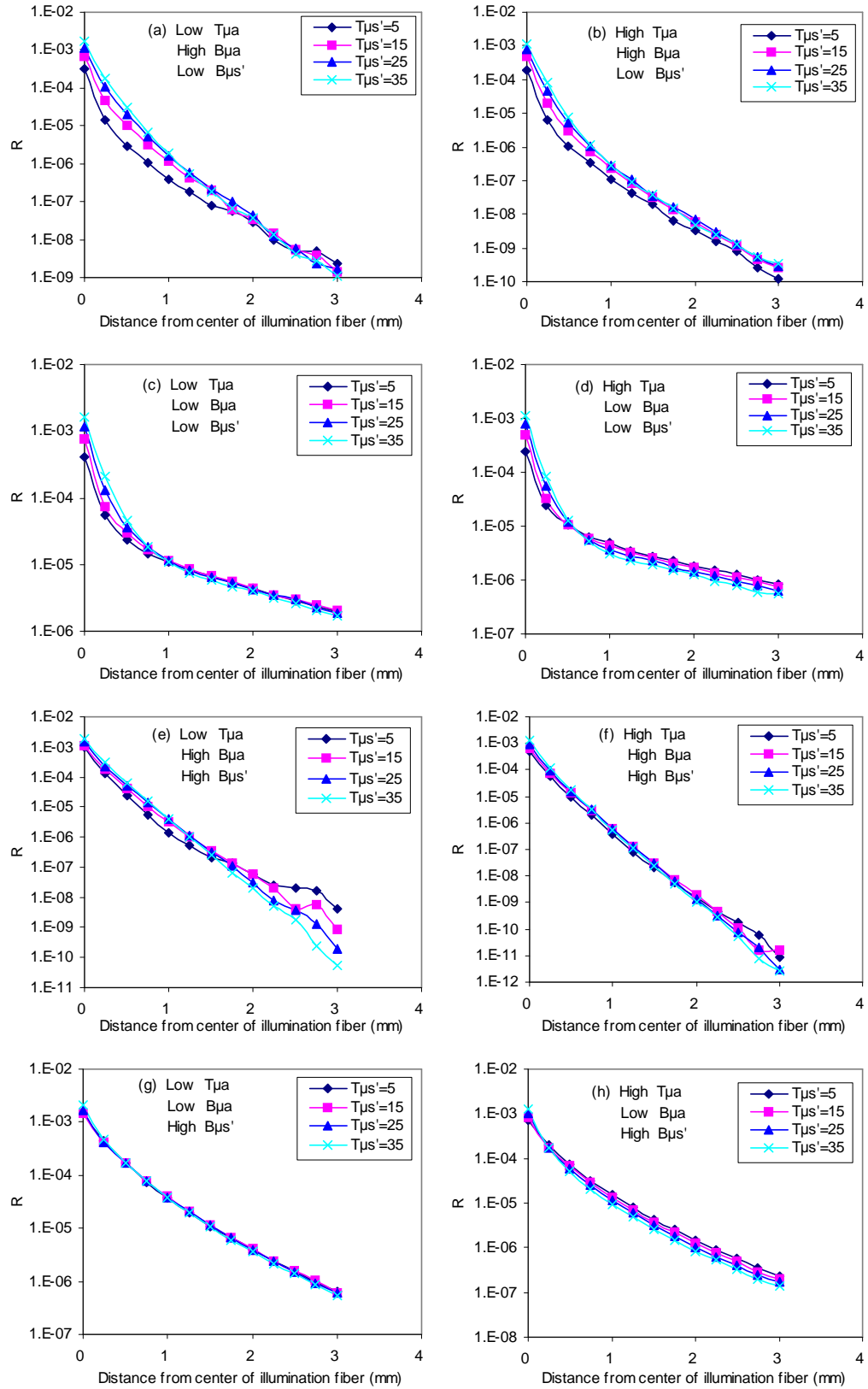


Fig. 67 Influence of top layer μ_s' on reflectance

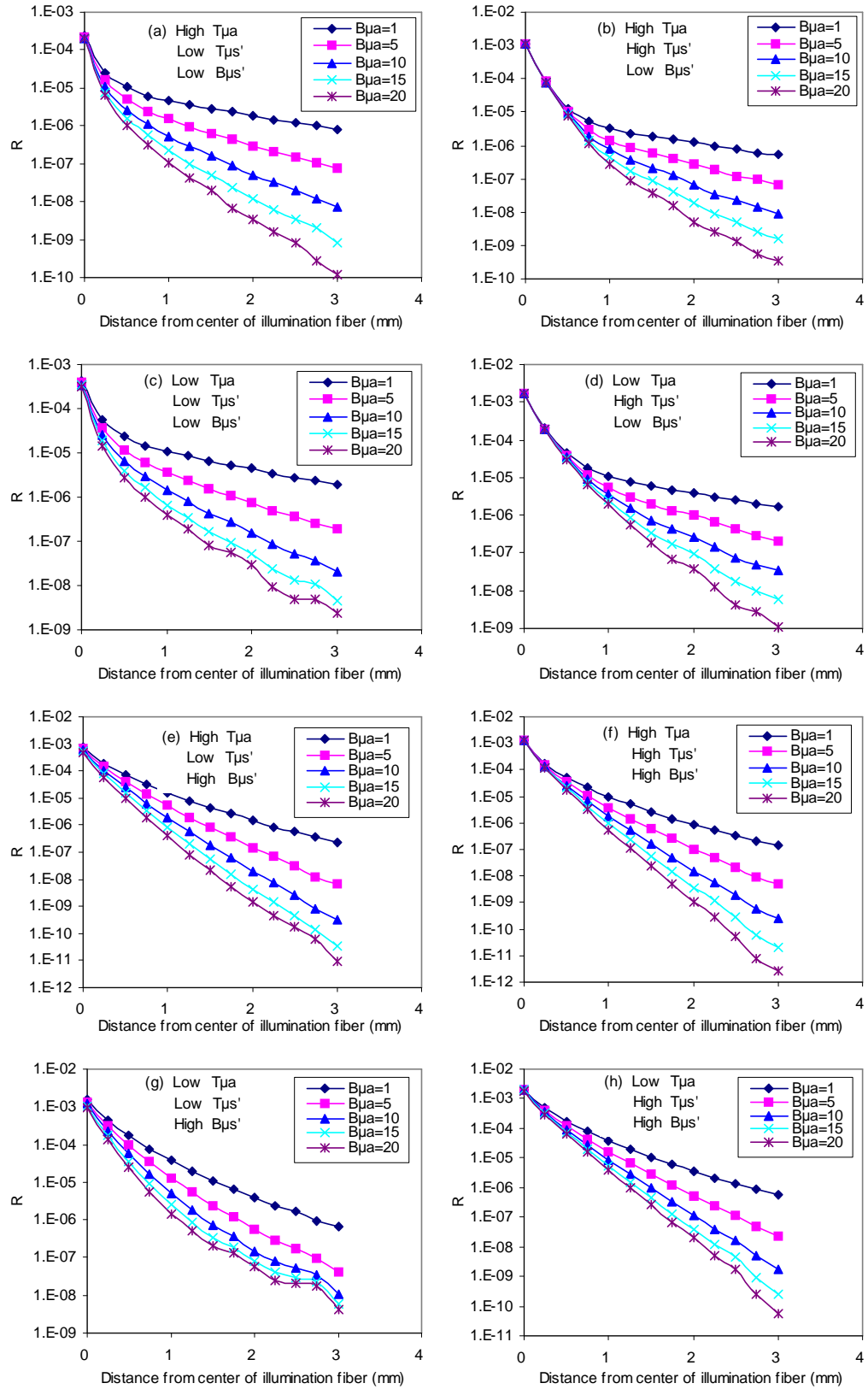


Fig. 68 Influence of bottom layer μ_a on reflectance

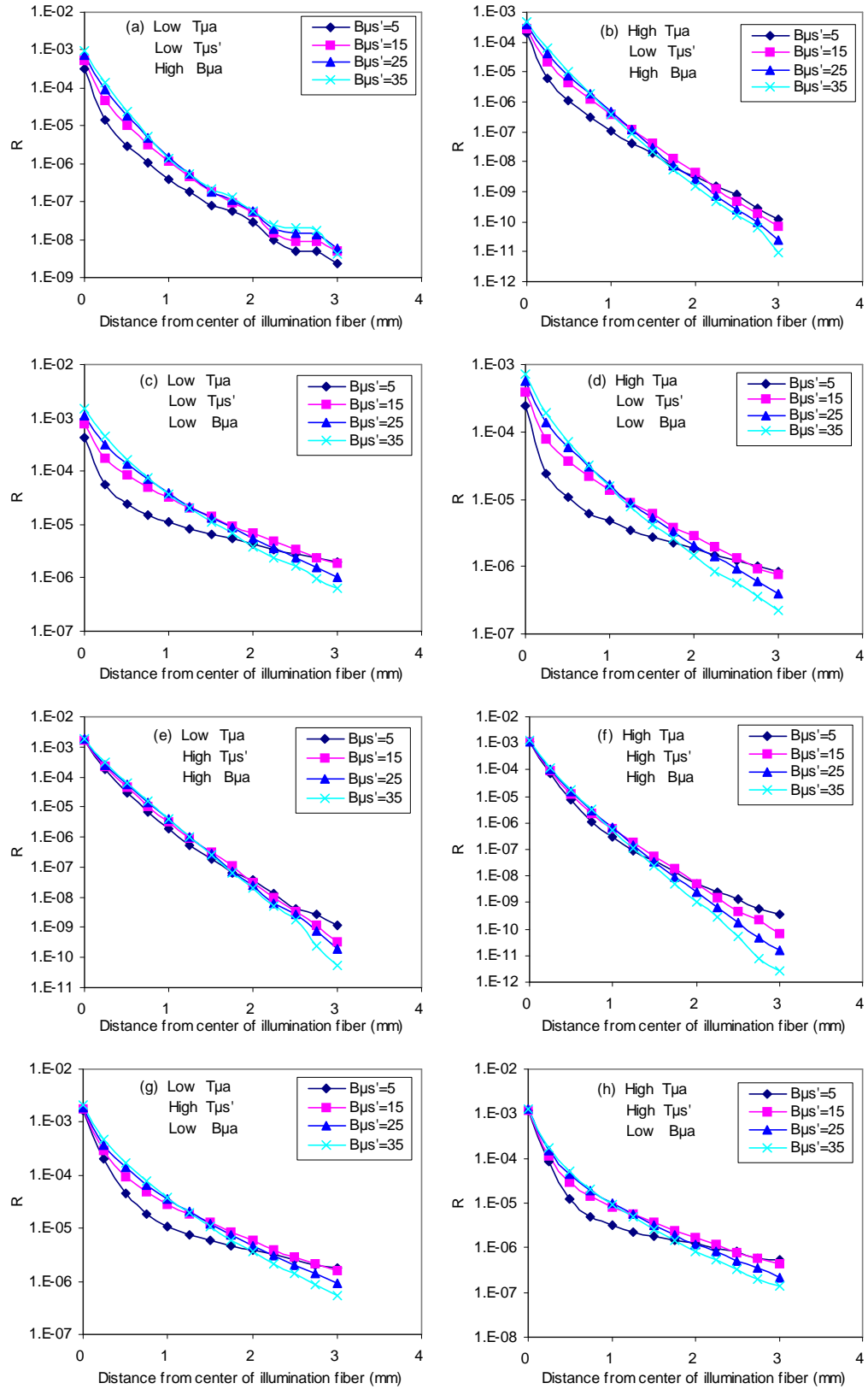


Fig. 69 Influence of bottom layer μ_s' on reflectance

Fast Monte Carlo results shown in Fig. 66 - Fig. 69 demonstrate the influence of top μ_a , top μ_s' , bottom μ_a and bottom μ_s' . All numbers in the legends of these figures have units of cm^{-1} . From these figures, reflectance values from the illumination-detection fiber are around the level of 1×10^{-3} . This value is sensitive to top μ_s' when the bottom μ_s' is low or to bottom μ_s' when the top μ_s' is low (Fig. 67 (a)-(d) and Fig. 69 (a)-(d)). Reflectance from fibers at further distance from the illumination-detection fiber carries more information about bottom μ_a . Higher bottom μ_a results in a significant lower reflectance (Fig. 66 (a), (b), (e), (f) and Fig. 68 (a), (b), (e), (f)). High attenuation in the bottom layer reduced the collection efficiency of the distant fibers to the point where the results often show significant noise levels. When bottom μ_s' is small, reflectance signal decays faster near the illumination point compared with when bottom μ_s' is large (Fig. 66 and Fig. 68). When bottom μ_s' is high, effect of top μ_s' on reflectance is concealed (Fig. 67 (e)-(h)). This effect is very clear in Fig. 67 (g). From this graph, reflectance curves from different top μ_s' almost totally overlapped. This means that solutions of optical properties from an inverse model are not unique and the error will be large. On the other hand, effect of bottom μ_s' on reflectance from further detection fibers is larger than effect of top μ_s' in general when the top layer thickness is 0.2 mm (Fig. 67 and Fig. 69), which implies that the error of top μ_s' from an inverse model will be larger than the error of bottom μ_s' . Graphs in Fig. 68 show an interesting 'broom' shape. The handle part of the 'broom' indicates that reflectance at short separation distances is not sensitive to bottom μ_a change, especially when top μ_s' is high (Fig. 68 (b),(d),(f) & (h)). Comparison of Fig. 66 and Fig. 68 shows that reflectance is more sensitive to top μ_a change for nearer fibers and more sensitive to bottom μ_a change for further fibers. For detection fibers with separation distance of 0 to 3 mm, the influence of bottom μ_a on reflectance is larger than influence of top μ_a in general, which means the error of top μ_a values estimated from an inverse model will likely be higher. Under highly attenuating conditions (tissues, wavelengths), larger

separation distance fibers did not collect sufficient signal (Fig. 66(e), Fig. 67(e), Fig. 68(g) and Fig. 69 (a)).

5.5 Determination of optical properties of a two-layer tissue with neural network models

In this investigation, a forward multi-layer Monte Carlo simulation was developed and run as a primary simulation, followed by multi-layer fast Monte Carlo simulations according to the scaling method to extend the datasets. With the reflectance datasets generated with the fast Monte Carlo simulations, four feed-forward back-propagation neural network models were trained and evaluated with the Neural Network Toolbox in Matlab® based on four different fiberoptic probe geometries. The input vector for each network (sometimes referred to as an “input layer”) consisted of 5, 6, 10 or 11 reflectance values corresponding to the number of fibers used. The probe geometries for four neural networks are shown in Table 11. Each network also contained two hidden layers of seven neurons each with logarithmic sigmoid transfer functions, and an output layer of two neurons with linear transfer functions. The output vector consisted of the values of top layer μ_a , top layer μ_s' , bottom layer μ_a and bottom layer μ_s' . A Levenberg-Marquardt backpropagation training function was used. The number of neurons came from my optimization results. The reflectance datasets used for training included 26500 optical property combinations that were evenly distributed in the range of 1-22.5 cm^{-1} for top layer μ_a and bottom layer μ_a and 5-42.5 cm^{-1} for top layer μ_s' and bottom layer μ_s' . Besides, 12800 optical property combinations that were randomly distributed within the same range were used for evaluation during training.

Table 11. Fiber geometries for neural network training (radius of each fiber is 0.1 mm)

Center position from illumination point (mm)	0	0.25	0.50	0.75	1.00	1.25	1.50	1.75	2.00	2.25	2.50
Geometry of 5 fibers			v		v		v		v		v
Geometry of 6 fibers	v		v		v		v		v		v
Geometry of 10 fibers		v	v	v	v	v	v	v	v	v	v
Geometry of 11 fibers	v	v	v	v	v	v	v	v	v	v	v

Note: 'v' means this fiber was selected.

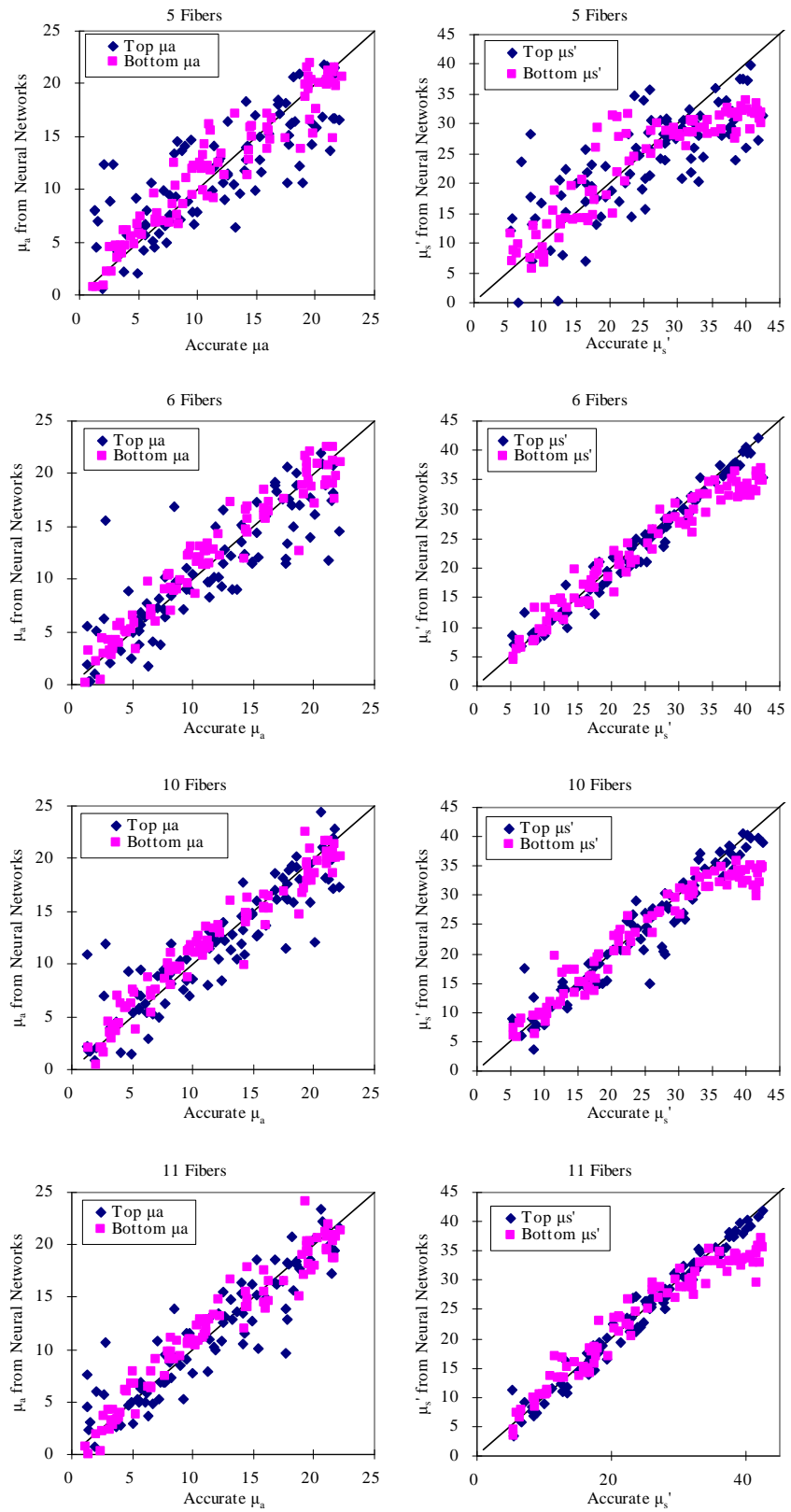


Fig. 70 Neural network results with different probe geometries (The line is where the predicted values are equal to the accurate ones.)

A set of four neural network inverse models were trained with reflectance data based on fiber geometries described in Table 11. The accuracy of these models was evaluated with 90 optical property combinations randomly distributed within the same optical range as described in Section 2.3. Fig. 70 compared the optical property values determined from the neural network model with the true values. These results indicate that estimates of bottom μ_a are more accurate than top μ_a . However, errors for top μ_s' and bottom μ_s' are at the same level. Comparison of the graphs for 5-fiber and 10-fiber probes shows that more fibers can improve the neural network accuracy within the same distance range from the illumination point. Graphs representing 6-fiber and 11-fiber probes show that reflectance from the illumination-detection fiber can significantly improve neural network accuracy particularly the top μ_s' . Table 12 provides a quantitative summary of the results in Fig. 70. The table shows that the average error in determination of μ_a ranged from 15 to 51% and average error for μ_s' ranged from 8 to 32%.

Table 12. Optical property estimation errors for neural networks based on four different probe geometries

	5 fibers	6 fibers	10 fibers	11 fibers
Top μ_a	51%	31%	31%	30%
Bottom μ_a	18%	16%	17%	15%
Top μ_s'	32%	8%	12%	8%
Bottom μ_s'	20%	11%	12%	11%

5.6 Conclusions

I have presented a fast Monte Carlo method to generate a database of reflectance from a two-layer tissue with different optical properties. The accuracy of this method was verified theoretically. Using this method, the influence of optical properties on reflectance was investigated and data for training a neural network-based inverse model was generated. The resulting model was evaluated using randomly generated reflectance data.

Results show that: (1) in general, the approach presented here for estimation of the optical properties can provide accuracy levels of 8-30% in a two-layer tissue; (2) there may be several weaknesses to this approach, including difficulties in determining top

layer μ_s' when bottom layer μ_s' is high; (3) a larger number of fibers (e.g., 11 over a 3 mm probe), including the use of an illumination collection fiber (or other approach to highly superficial signal detection), may improve accuracy (4) signal detection for highly attenuating tissues may present a significant obstacle to highly accurate measurements.

While computationally expensive to develop, neural network models calibrated with simulation data may prove to be a highly effective approach for rapid, unconstrained estimation of the optical properties of two-layer tissues. The current technique is shown to be theoretically effective, thus representing a significant step towards development of a system for unconstrained determination of optical properties in layered tissue.

Chapter 6. CONCLUDING REMARKS

6.1 Summary and contributions

The whole research include fiberoptic system construction, evaluation, and implementation, light-tissue interaction modeling, probe geometry investigation and single- and multi-layer tissue study. The goal of this work is to improve quantitative understanding of the relationship between reflectance spectroscopy and optical properties of mucosal tissues and obtain optical property data of these tissues, which will then (1) help use diffuse reflectance for cancer diagnosis, (2) improve understanding of device design parameters, (3) and provide valuable optical property data for theoretical modeling. This goal has been achieved. The contributions of this work can be summarized as follows:

1. For the first time, a noninvasive, fiberoptic probe-based approach was implemented to measure epithelial tissue optical properties at UVA-VIS wavelengths. A novel, multi-wavelength, fiberoptic system was constructed, evaluated and implemented to determine internal tissue optical properties. A condensed Monte Carlo model and an inverse neural network model were used to estimate μ_a and μ_s' based on spatially-resolved reflectance distributions. The theoretical and experimental evidence show the capability of our novel system to yield accurate optical property measurements within the UVA-VIS wavelength range.
2. I championed a novel version of the condensed Monte Carlo method for illumination-detection fiber probes, thus enabling rapid computation of large sets of tissue reflectance data. The effect of fiber diameter on the relationship between reflectance and tissue optical properties was characterized, which show

that bigger fiber is more sensitive to μ_a . The simulation of reflectance over a range of wavelengths from 400-500 nm based on the optical properties of breast tissue elucidated the effect of fiber diameter on reflectance spectra measured in malignant and adipose breast tissues. Also, the effect of adding an illumination-detection fiber to a linear array fiber probe for optical property determination was evaluated, which showed a promising accuracy improvement.

3. An unconstrained approach for estimating optical properties in a two-layer tissue, using a novel condensed Monte Carlo technique and neural network model, was developed and validated for the first time. The two-layer tissue situation was studied to elucidate light propagation mechanisms during optical spectroscopy measurement in epithelial tissue. I characterized the relationship between spatially-resolved reflectance distributions and optical properties in two-layer tissue models, then formulated and evaluated the unconstrained approach to optical property measurement. While computationally expensive to develop, neural network models calibrated with Monte Carlo simulation data proved to be a highly effective approach for rapid, unconstrained estimation of the optical properties of two-layer tissues.

In summary, the goal in the initial proposal was achieved. My research shows that the combination of condensed Monte Carlo models and neural networks models represents a powerful technique for rapid simulation of light-tissue interactions and for optical property extraction from reflectance measurement. The fiberoptic diffuse reflectance system I developed can potentially be used for *in situ* cancer diagnosis.

6.2 Suggestions for future study

Research will never end. Based on the data in this dissertation, several possible future research directions that are mainly natural extensions of this study include:

1. My study shows that absorption by other chromophores besides hemoglobin in tissues become increasingly significant in the UVA and short VIS ranges. These chromophores could be collagen, elastin, DNA and some other proteins. In the future, it may be possible to determine the concentrations of these chromophores through fitting algorithms.
2. The condensed Monte Carlo simulation for a single illumination-detection fiber was demonstrated to be a powerful technique for rapid simulation of light-tissue interaction. Theoretically, this technique can improve the accuracy of optical detection when combined with separated fiber geometries. However, this technique should be evaluated with experiments. A possible problem in experiments could be the high intensity of specular reflectance. How to separate diffuse reflectance from specular reflectance will be a challenge. Further study should be continued on this issue.
3. In the two-layer tissue modeling, I have presented a fast Monte Carlo method to generate a database for a tissue with given top-layer thickness. The accuracy of this method was verified theoretically. The current technique is shown to be theoretically effective, thus representing a significant step towards development of a system for unconstrained determination of optical properties in layered tissue. However, several additional steps will be required before this approach can be implemented on a biological tissue. Perhaps most importantly, the model will have to be trained to determine superficial layer thickness. This modification will likely require extensive additional simulations to train the model over a variety of thicknesses relevant to normal and cancerous mucosa. Experimental validation of this technique in well-controlled tissue-simulating samples will also be needed.

BIBLIOGRAPHY

- [1] A. Jemal, T. Murray, E. Ward, A. Samuels, R. C. Tiwari, A. Ghafoor, E. J. Feuer, and M. J. Thun, "Cancer statistics, 2005," *Ca-a Cancer Journal for Clinicians* **55**, 10-30 (2005).
- [2] SpectraScience, http://www.spectrascience.com/index.php?static/wavstat_system, Accessed on April 8, 2009.
- [3] L. Ries, M. Eisner, C. Kosary, B. Hankey, B. Miller, L. Clegg, A. Mariotto, M. Fay, and E. Feuer, *SEER Cancer Statistics Review, 1975-2000* (National Cancer Institute, Bethesda, MD, 2003).
- [4] N. Ramanujam, "Fluorescence spectroscopy of neoplastic and non-neoplastic tissues," *Neoplasia* **2**, 89-117 (2000).
- [5] B. C. Wilson, and S. L. Jacques, "Optical reflectance and transmittance of tissues - principles and applications," *IEEE Journal of Quantum Electronics* **26**, 2186-2199 (1990).
- [6] Y. L. Kim, Y. Liu, R. K. Wali, H. K. Roy, M. J. Goldberg, A. K. Kromin, K. Chen, and V. Backman, "Simultaneous measurement of angular and spectral properties of light scattering for characterization of tissue microarchitecture and its alteration in early precancer," *IEEE Journal of Selected Topics in Quantum Electronics* **9**, 243-256 (2003).
- [7] J. A. Freeberg, J. L. Benedet, C. MacAulay, L. A. West, and M. Follen, "The performance of fluorescence and reflectance spectroscopy for the in vivo diagnosis of cervical neoplasia; point probe versus multispectral approaches," *Gynecologic Oncology* **107**, S248-S255 (2007).
- [8] D. Arifler, C. MacAulay, M. Follen, and R. Richards-Kortum, "Spatially resolved reflectance spectroscopy for diagnosis of cervical precancer: Monte Carlo modeling and comparison to clinical measurements," *Journal of Biomedical Optics* **11**, (2006).
- [9] M. Fitzmaurice, M. B. Wallace, L. T. Perelman, V. Backman, J. M. Crawford, M. Seiler, K. Badizadegan, S. J. Shields, I. Itzkan, R. Dasari, J. Van Dam, and M. S. Feld, "Endoscopic diagnosis of dysplasia in Barrett's esophagus (BE): A novel light scattering-reflectance spectroscopy technique," *Laboratory Investigation* **79**, 428 (1999).
- [10] M. B. Wallace, J. Tunnell, S. M. Wildi, C. Jost, J. Nazemi, S. McGee, J. Mirkovic, L. Galindo, R. Dasari, and M. Feld, "Real time optical detection of dysplasia in Barrett's esophagus using tri-modal (diffuse reflectance, fluorescence, light-scattering) spectroscopy," (2005), pp. A51-A51.
- [11] M. B. Wallace, S. J. Shields, L. T. Perelman, B. Packman, G. Zonios, R. Manoharan, K. Badizadegan, A. Nusrat, M. Seller, T. Hamano, I. Itzkan, C. Lima, M. Fitzmaurice, J. M. Crawford, J. Van Dam, and M. S. Feld, "Fiber-optic detection of low-grade dysplasia in patients with Barrett's esophagus using reflectance spectroscopy," *Gastroenterology* **114**, G1337 (1998).
- [12] I. Georgakoudi, B. C. Jacobson, J. Van Dam, V. Backman, M. B. Wallace, M. G. Muller, Q. Zhang, K. Badizadegan, D. Sun, G. A. Thomas, L. T. Perelman, and M. S. Feld, "Fluorescence, reflectance, and light-scattering spectroscopy for evaluating dysplasia in patients with Barrett's esophagus," *Gastroenterology* **120**, 1620-1629 (2001).
- [13] D. Hidovic-Rowe, and E. Claridge, "Modelling and validation of spectral reflectance for the colon," *Physics in Medicine and Biology* **50**, 1071-1093 (2005).
- [14] G. Zonios, L. T. Perelman, V. M. Backman, R. Manoharan, M. Fitzmaurice, J. Van Dam, and M. S. Feld, "Diffuse reflectance spectroscopy of human adenomatous colon polyps in vivo," *Applied Optics* **38**, 6628-6637 (1999).
- [15] A. E. Arai, C. E. Kasserra, A. Gandjbakhche, R. Bonner, and R. S. Balaban, "Optical reflectance spectroscopy measures cellular oxygenation, in vivo: Effect of work," *Circulation* **96**, 3876-3876 (1997).
- [16] M. Guichard, E. Lartigau, E. Tinet, C. Thomas, and S. Avriillier, "A follow-up of non-invasive tumour oxygenation using differential reflectance," *Journal of Optics-Nouvelle Revue D Optique* **28**, 265-269 (1997).
- [17] E. Haggblad, T. Lindbergh, M. G. D. Karlsson, H. Casimir-Ahn, E. G. Salerud, and T. Stromberg, "Myocardial tissue oxygenation estimated with calibrated diffuse reflectance spectroscopy during coronary artery bypass grafting," *Journal of Biomedical Optics* **13**, (2008).

- [18] R. J. Hunter, M. S. Patterson, T. J. Farrell, and J. E. Hayward, "Haemoglobin oxygenation of a two-layer tissue-simulating phantom from time-resolved reflectance: effect of top layer thickness," *Physics in Medicine and Biology* **47**, 193-208 (2002).
- [19] Z. Y. Li, E. W. C. Tam, A. F. T. Mak, and R. Y. C. Lau, "Effects of prolonged compression on the variations of haemoglobin oxygenation - assessment by spectral analysis of reflectance spectrophotometry signals," *Physics in Medicine and Biology* **51**, 5707-5718 (2006).
- [20] U. Merschbrock, J. Hoffmann, L. Caspary, J. Huber, U. Schmickaly, and D. W. Lubbers, "Fast wavelength scanning reflectance spectrophotometer for noninvasive determination of hemoglobin oxygenation in human skin," *International Journal of Microcirculation-Clinical and Experimental* **14**, 274-281 (1994).
- [21] M. Solonenko, R. Cheung, T. M. Busch, A. Kachur, G. M. Griffin, T. Vulcan, T. C. Zhu, H. W. Wang, S. M. Hahn, and A. G. Yodh, "In vivo reflectance measurement of optical properties, blood oxygenation and motexafin lutetium uptake in canine large bowels, kidneys and prostates," *Physics in Medicine and Biology* **47**, 857-873 (2002).
- [22] M. Tsujii, S. Kawano, S. Tsuji, I. Kobayashi, Y. Takei, K. Nagano, H. Fusamoto, T. Kamada, T. Ogihara, and N. Sato, "Colonic mucosal hemodynamics and tissue oxygenation in patients with ulcerative-colitis-investigation by organ reflectance spectrophotometry," *Journal of Gastroenterology* **30**, 183-188 (1995).
- [23] H. W. Wang, T. C. Zhu, M. E. Putt, M. Solonenko, J. Metz, A. Dimofte, J. Miles, D. L. Fraker, E. Glatstein, S. M. Hahn, and A. G. Yodh, "Broadband reflectance measurements of light penetration, blood oxygenation, hemoglobin concentration, and drug concentration in human intraperitoneal tissues before and after photodynamic therapy," *Journal of Biomedical Optics* **10**, (2005).
- [24] S. Friedland, D. Benaron, I. Parachikov, and R. Soetikno, "Measurement of mucosal capillary hemoglobin oxygen saturation in the colon by reflectance spectrophotometry," *Gastrointestinal Endoscopy* **57**, 492-497 (2003).
- [25] C. M. Draque, M. Fernanda, B. Almeida, A. Sanudo, C. A. Peres, A. M. N. Santos, and B. I. Kopelman, "Transcutaneous total bilirubin levels by multiwavelength spectral reflectance: Accuracy in term newborn infants," *Pediatric Research* **51**, 1993 (2002).
- [26] V. Bhutani, L. H. Johnson, G. Gourley, and S. Adler, "Transcutaneous measurement (TcB) of total serum bilirubin (TSB) by multi-wavelength spectral reflectance (BillCheck (TM)): Accuracy and precision in newborn results," *Pediatric Research* **45**, 1089 (1999).
- [27] R. E. Hannemann, D. P. Dewitt, E. J. Hanley, R. L. Schreiner, and P. Bonderman, "Determination of serum bilirubin by skin reflectance - effect of pigmentation," *Pediatric Research* **13**, 1326-1329 (1979).
- [28] R. E. Hannemann, D. P. Dewitt, and J. F. Wiechel, "Neonatal serum bilirubin from skin reflectance," *Pediatric Research* **12**, 207-210 (1978).
- [29] K. J. Peevy, L. Mumford, R. Bruce, and S. J. Gross, "Estimation of serum bilirubin by spectral reflectance of skin," *Pediatric Research* **12**, 532-532 (1978).
- [30] R. L. Schreiner, R. E. Hannemann, D. P. Dewitt, and H. C. Moorehead, "Relationship of skin reflectance and serum bilirubin - full term Caucasian infants," *Human Biology* **51**, 31-40 (1979).
- [31] K. J. Jeon, I. D. Hwang, S. Hahn, and G. Yoon, "Comparison between transmittance and reflectance measurements in glucose determination using near infrared spectroscopy," *Journal of Biomedical Optics* **11**, (2006).
- [32] L. Huang, H. S. Ding, and G. Z. Wang, "The preliminary study on noninvasive detection using NIR diffusion reflectance spectrum for monitoring blood glucose," *Spectroscopy and Spectral Analysis* **22**, 387-391 (2002).
- [33] K. Maruo, M. Tsurugi, M. Tamura, and Y. Ozaki, "In vivo noninvasive measurement of blood glucose by near-infrared diffuse-reflectance spectroscopy," *Applied Spectroscopy* **57**, 1236-1244 (2003).

- [34] S. J. Yeh, C. F. Hanna, and O. S. Khalil, "Monitoring blood glucose changes in cutaneous tissue by temperature-modulated localized reflectance measurements," *Clinical Chemistry* **49**, 924-934 (2003).
- [35] H. Y. Zhang, D. Ding, L. Q. Song, L. N. Gu, P. Yang, and Y. G. Tang, "Achievement of the noninvasive measurement for human blood glucose with NIR diffusion reflectance spectrum method," *Spectroscopy and Spectral Analysis* **25**, 882-885 (2005).
- [36] P. R. Bargo, S. A. Prahl, T. T. Goodell, R. A. Steven, G. Koval, G. Blair, and S. L. Jacques, "In vivo determination of optical properties of normal and tumor tissue with white light reflectance and an empirical light transport model during endoscopy," *Journal of Biomedical Optics* **10**, (2005).
- [37] R. M. P. Doornbos, R. Lang, M. C. Aalders, F. W. Cross, and H. Sterenborg, "The determination of in vivo human tissue optical properties and absolute chromophore concentrations using spatially resolved steady-state diffuse reflectance spectroscopy," *Physics in Medicine and Biology* **44**, 967-981 (1999).
- [38] M. S. Patterson, B. Chance, and B. C. Wilson, "Time resolved reflectance and transmittance for the noninvasive measurement of tissue optical properties," *Applied Optics* **28**, 2331-2336 (1989).
- [39] T. J. Pfefer, L. S. Matchette, C. L. Bennett, J. A. Gall, J. N. Wilke, A. J. Durkin, and M. N. Ediger, "Reflectance-based determination of optical properties in highly attenuating tissue," *Journal of Biomedical Optics* **8**, 206-215 (2003).
- [40] Q. Z. Wang, H. Z. Yang, A. Agrawal, N. S. Wang, and T. J. Pfefer, "Measurement of internal tissue optical properties at ultraviolet and visible wavelengths: Development and implementation of a fiberoptic-based system," *Optics Express* **16**, 8685-8703 (2008).
- [41] E. Hecht, *Optics* (Addison Wesley, San Francisco, 2002).
- [42] Oregon Graduate Institute, <http://omlc.ogi.edu/classroom/ece532/index.html>, Accessed on Feb 19, 2009.
- [43] P. N. Prasad, *Introduction to Biophotonics* (John Wiley & Sons, Inc, Hoboken, New Jersey, 2003).
- [44] T. Vo-Dinh, *Biomedical Photonics Handbook* (CRC, 2003).
- [45] S. L. Jacques, and L. Wang, "Monte Carlo modeling of light transport in tissues," in *Optical-Thermal Response of Laser Irradiated Tissue*, Welch A. J., and Gemert M. J. C. V., eds. (Plenum press, New York and London, 1995), pp. 73-100.
- [46] T. Collier, D. Arifler, A. Malpica, M. Follen, and R. Richards-Kortum, "Determination of epithelial tissue scattering coefficient using confocal microscopy," *IEEE Journal of Selected Topics in Quantum Electronics* **9**, 307-313 (2003).
- [47] W. K. Hong, and M. B. Sporn, "Recent advances in chemoprevention of cancer," *Science* **278**, 1073-1077 (1997).
- [48] R. Drezek, M. Guillaud, T. Collier, I. Boiko, A. Malpica, C. Macaulay, M. Follen, and R. Richards-Kortum, "Light scattering from cervical cells throughout neoplastic progression: influence of nuclear morphology, DNA content, and chromatin texture," *Journal of Biomedical Optics* **8**, 7-16 (2003).
- [49] D. Arifler, M. Guillaud, A. Carraro, A. Malpica, M. Follen, and R. Richards-Kortum, "Light scattering from normal and dysplastic cervical cells at different epithelial depths: finite-difference time-domain modeling with a perfectly matched layer boundary condition," *Journal of Biomedical Optics* **8**, 484-494 (2003).
- [50] M. G. Muller, T. A. Valdez, I. Georgakoudi, V. Backman, C. Fuentes, S. Kabani, N. Laver, Z. M. Wang, C. W. Boone, R. R. Dasari, S. M. Shapshay, and M. S. Feld, "Spectroscopic detection and evaluation of morphologic and biochemical changes in early human oral carcinoma," *Cancer* **97**, 1681-1692 (2003).
- [51] B. Bodey, S. E. Siegel, and H. F. Kaiser, "Matrix metalloproteinase expression in malignant melanomas: Tumor-extracellular matrix interactions in invasion and metastasis," *In Vivo* **15**, 57-64 (2001).

- [52] Q. Liu, and N. Ramanujam, "Sequential estimation of optical properties of a two-layered epithelial tissue model from depth-resolved ultraviolet-visible diffuse reflectance spectra," *Applied Optics* **45**, 4776-4790 (2006).
- [53] K. J. Heppner, L. M. Matrisian, R. A. Jensen, and W. H. Rodgers, "Expression of most matrix metalloproteinase family members in breast cancer represents a tumor-induced host response," *American Journal of Pathology* **149**, 273-282 (1996).
- [54] I. Pavlova, K. Sokolov, R. Drezek, A. Malpica, M. Follen, and R. Richards-Kortum, "Microanatomical and biochemical origins of normal and precancerous cervical autofluorescence using laser-scanning fluorescence confocal microscopy," *Photochemistry and Photobiology* **77**, 550-555 (2003).
- [55] R. A. Milord, K. Lecksell, and J. I. Epstein, "An objective morphologic parameter to aid in the diagnosis of flat urothelial carcinoma in situ," *Human Pathology* **32**, 997-1002 (2001).
- [56] Y. Kumagai, K. Monma, and K. Kawada, "Magnifying chromoendoscopy of the esophagus: In-vivo pathological diagnosis using an endocytoscopy system," *Endoscopy* **36**, 590-594 (2004).
- [57] J. Folkman, "Tumor angiogenesis," in *The Molecular Basis of Cancer*, Mendelsohn J., Howley P. M., Isreal M. A., and Liotta L. A., eds. (Saunders, Philadelphia, PA, 1995), pp. 206-232.
- [58] P. Ravazoula, V. Zolota, O. Hatjicondi, G. Sakellaropoulos, G. Kourounis, and M. E. Maragoudakis, "Assessment of angiogenesis in human cervical lesions," *Anticancer Research* **16**, 3861-3864 (1996).
- [59] J. S. Lee, H. S. Kim, J. J. Jung, M. C. Lee, and C. S. Park, "Angiogenesis, cell proliferation and apoptosis in progression of cervical neoplasia," *Analytical and Quantitative Cytology and Histology* **24**, 103-113 (2002).
- [60] D. Arifler, R. A. Schwarz, S. K. Chang, and R. Richards-Kortum, "Reflectance spectroscopy for diagnosis of epithelial precancer: model-based analysis of fiber-optic probe designs to resolve spectral information from epithelium and stroma," *Applied Optics* **44**, 4291-4305 (2005).
- [61] B. Yu, E. S. Burnside, G. A. Sisney, J. M. Harter, C. Zhu, A. H. Dhalla, and N. Ramanujam, "Feasibility of near-infrared diffuse optical spectroscopy on patients undergoing image-guided core-needle biopsy," *Optics Express* **15**, 7335-7350 (2007).
- [62] A. Cerussi, D. Hsiang, N. Shah, R. Mehta, A. Durkin, J. Butler, and B. J. Tromberg, "Predicting response to breast cancer neoadjuvant chemotherapy using diffuse optical spectroscopy," *Proceedings of the National Academy of Sciences of the United States of America* **104**, 4014-4019 (2007).
- [63] D. B. Jakubowski, A. E. Cerussi, F. Bevilacqua, N. Shah, D. Hsiang, J. Butler, and B. J. Tromberg, "Monitoring neoadjuvant chemotherapy in breast cancer using quantitative diffuse optical spectroscopy: a case study," *Journal of Biomedical Optics* **9**, 230-238 (2004).
- [64] C. Zhou, R. Choe, N. Shah, T. Durduran, G. Q. Yu, A. Durkin, D. Hsiang, R. Mehta, J. Butler, A. Cerussi, B. J. Tromberg, and A. G. Yodh, "Diffuse optical monitoring of blood flow and oxygenation in human breast cancer during early stages of neoadjuvant chemotherapy," (2007).
- [65] Q. N. Zhu, S. H. Kurtzman, P. Hegde, S. Tannenbaum, M. Kane, M. M. Huang, N. G. Chen, B. Jagjivan, and K. Zarfes, "Utilizing optical tomography with ultrasound localization to image heterogeneous hemoglobin distribution in large breast cancers," *Neoplasia* **7**, 263-270 (2005).
- [66] J. Lee, A. E. Cerussi, D. Saltzman, T. Waddington, B. J. Tromberg, and M. Brenner, "Hemoglobin measurement patterns during noninvasive diffuse optical spectroscopy monitoring of hypovolemic shock and fluid replacement," *Journal of Biomedical Optics* **12**, (2007).
- [67] J. Sun, K. Fu, A. Wang, A. W. H. Lin, U. Utzinger, and R. Drezek, "Influence of fiber optic probe geometry on the applicability of inverse models of tissue reflectance spectroscopy: computational models and experimental measurements," *Applied Optics* **45**, 8152-8162 (2006).
- [68] S. T. Flock, S. L. Jacques, B. C. Wilson, W. M. Star, and M. J. C. Vangemert, "Optical-Properties of Intralipid - a Phantom Medium for Light-Propagation Studies," *Lasers in Surgery and Medicine* **12**, 510-519 (1992).

- [69] M. Firbank, and D. T. Delpy, "A Design for a Stable and Reproducible Phantom for Use in near-Infrared Imaging and Spectroscopy," *Physics in Medicine and Biology* **38**, 847-853 (1993).
- [70] G. Wagnieres, S. G. Cheng, M. Zellweger, N. Utke, D. Braichotte, J. P. Ballini, and H. vandenBergh, "An optical phantom with tissue-like properties in the visible for use in PDT and fluorescence spectroscopy," *Physics in Medicine and Biology* **42**, 1415-1426 (1997).
- [71] B. W. Pogue, and M. S. Patterson, "Review of tissue simulating phantoms for optical spectroscopy, imaging and dosimetry," *Journal of Biomedical Optics* **11**, 041102 (2006).
- [72] K. M. Quan, G. B. Christison, H. A. Mackenzie, and P. Hodgson, "Glucose Determination by a Pulsed Photoacoustic Technique - an Experimental-Study Using a Gelatin-Based Tissue Phantom," *Physics in Medicine and Biology* **38**, 1911-1922 (1993).
- [73] R. A. Schwarz, D. Arifler, S. K. Chang, I. Pavlova, I. A. Hussain, V. Mack, B. Knight, R. Richards-Kortum, and A. M. Gillenwater, "Ball lens coupled fiber-optic probe for depth-resolved spectroscopy of epithelial tissue," *Optics Letters* **30**, 1159-1161 (2005).
- [74] R. Cubeddu, A. Pifferi, P. Taroni, A. Torricelli, and G. Valentini, "A solid tissue phantom for photon migration studies," *Physics in Medicine and Biology* **42**, 1971-1979 (1997).
- [75] L. Wielopolski, M. Maryanski, A. C. Washington, G. Schidlovsky, S. H. Cohn, L. E. Reinstein, A. M. Kalend, and A. B. Meek, "Polyacrylamide-Based Phantoms as Tissue Substitute in Experimental Radiation Physics," *Medical Physics* **12**, 788-792 (1985).
- [76] G. Delacretaz, J. T. Walsh, and T. Asshauer, "Dynamic polariscopic imaging of laser-induced strain in a tissue phantom," *Applied Physics Letters* **70**, 3510-3512 (1997).
- [77] J. A. Viator, G. Au, G. Paltauf, S. L. Jacques, S. A. Prahl, H. W. Ren, Z. P. Chen, and J. S. Nelson, "Clinical testing of a photoacoustic probe for port wine stain depth determination," *Lasers in Surgery and Medicine* **30**, 141-148 (2002).
- [78] J. A. Viator, B. Choi, G. M. Peavy, S. Kimel, and J. S. Nelson, "Spectra from 2.5-15 μ m of tissue phantom materials, optical clearing agents and ex vivo human skin: implications for depth profiling of human skin," *Physics in Medicine and Biology* **48**, N15-N24 (2003).
- [79] F. Yokoyama, I. Masada, K. Shimamura, T. Ikawa, and K. Monobe, "Morphology and Structure of Highly Elastic Polyvinyl-Alcohol) Hydrogel Prepared by Repeated Freezing-and-Melting," *Colloid and Polymer Science* **264**, 595-601 (1986).
- [80] K. Yamaura, M. Itoh, T. Tanigami, and S. Matsuzawa, "Properties of gels obtained by freezing/thawing of poly(vinyl alcohol)/water/dimethyl sulfoxide solutions," *J. Appl. Polym. Sci.* **37**, 2709-2718 (2003).
- [81] U. Sukowski, F. Schubert, D. Grosenick, and H. Rinneberg, "Preparation of solid phantoms with defined scattering and absorption properties for optical tomography," *Physics in Medicine and Biology* **41**, 1823-1844 (1996).
- [82] J. C. Hebden, D. J. Hall, M. Firbank, and D. T. Delpy, "Time-Resolved Optical Imaging of a Solid Tissue-Equivalent Phantom," *Applied Optics* **34**, 8038-8047 (1995).
- [83] M. Firbank, M. Oda, and D. T. Delpy, "An Improved Design for a Stable and Reproducible Phantom Material for Use in near-Infrared Spectroscopy and Imaging," *Physics in Medicine and Biology* **40**, 955-961 (1995).
- [84] M. L. Vernon, J. Frechette, Y. Painchaud, S. Caron, and P. Beaudry, "Fabrication and characterization of a solid polyurethane phantom for optical imaging through scattering media," *Applied Optics* **38**, 4247-4251 (1999).
- [85] G. C. Beck, N. Akgun, A. Ruck, and R. Steiner, "Design and characterisation of a tissue phantom system for optical diagnostics," *Lasers in Medical Science* **13**, 160-171 (1998).
- [86] R. Bays, G. Wagnieres, D. Robert, J. F. Theumann, A. Vitkin, J. F. Savary, P. Monnier, and H. vandenBergh, "Three-dimensional optical phantom and its application in photodynamic therapy," *Lasers in Surgery and Medicine* **21**, 227-234 (1997).
- [87] J. Gade, D. Palmqvist, P. Plomgard, and G. Greisen, "Diffuse reflectance spectrophotometry with visible light: comparison of four different methods in a tissue phantom," *Physics in Medicine and Biology* **51**, 121-136 (2006).

- [88] O. F. do Nascimento, A. B. Villaverde, R. A. Zangaro, M. T. T. Pacheco, and S. F. Durrant, "Optical fiber device and biological tissue phantoms for determination of optical parameters in the near-infrared region," *Instrumentation Science & Technology* **32**, 489-505 (2004).
- [89] T. S. Tkaczyk, M. Rahman, V. Mack, K. Sokolov, J. D. Rogers, R. Richards-Kortum, and M. R. Descour, "High resolution, molecular-specific, reflectance imaging in optically dense tissue phantoms with structured-illumination," *Optics Express* **12**, 3745-3758 (2004).
- [90] S. Gupta, V. Raja, and A. Pradhan, "Simultaneous extraction of optical transport parameters and intrinsic fluorescence of tissue mimicking model media using a spatially resolved fluorescence technique," *Applied Optics* **45**, 7529-7537 (2006).
- [91] A. J. Durkin, S. Jaikumar, and R. Richardskortum, "Optically Dilute, Absorbing, and Turbid Phantoms for Fluorescence Spectroscopy of Homogeneous and Inhomogeneous Samples," *Applied Spectroscopy* **47**, 2114-2121 (1993).
- [92] O. Barajas, A. M. Ballangrud, G. G. Miller, R. B. Moore, and J. Tulip, "Monte Carlo modelling of angular radiance in tissue phantoms and human prostate: PDT light dosimetry," *Physics in Medicine and Biology* **42**, 1675-1687 (1997).
- [93] G. Soelkner, G. Mitic, and R. Lohwasser, "Monte Carlo simulations and laser Doppler flow measurements with high penetration depth in biological tissuelike head phantoms," *Applied Optics* **36**, 5647-5654 (1997).
- [94] M. Larsson, W. Steenbergen, and T. Stromberg, "Influence of optical properties and fiber separation on laser Doppler flowmetry," *Journal of Biomedical Optics* **7**, 236-243 (2002).
- [95] S. L. Jacques, and S. J. Kirkpatrick, "Acoustically modulated speckle imaging of biological tissues," *Optics Letters* **23**, 879-881 (1998).
- [96] J. P. Culver, T. Durduran, T. Furuya, C. Cheung, J. H. Greenberg, and A. G. Yodh, "Diffuse optical tomography of cerebral blood flow, oxygenation, and metabolism in rat during focal ischemia," *Journal of Cerebral Blood Flow and Metabolism* **23**, 911-924 (2003).
- [97] A. Bednov, S. Ulyanov, C. Cheung, and A. G. Yodh, "Correlation properties of multiple scattered light: implication to coherent diagnostics of burned skin," *Journal of Biomedical Optics* **9**, 347-352 (2004).
- [98] E. M. C. Hillman, D. A. Boas, A. M. Dale, and A. K. Dunn, "Laminar optical tomography: demonstration of millimeter-scale depth-resolved imaging in turbid media," *Optics Letters* **29**, 1650-1652 (2004).
- [99] J. Bateman, F. J. Weneck, and D. C. Eshler, "Determination of particle size and concentration from spectrophotometric transmission," *Journal of Colloid Science* **14**, 308-329 (1959).
- [100] X. Y. Ma, J. Q. Lu, R. S. Brock, K. M. Jacobs, P. Yang, and X. H. Hu, "Determination of complex refractive index of polystyrene microspheres from 370 to 1610 nm," *Physics in Medicine and Biology* **48**, 4165-4172 (2003).
- [101] R. H. Boundy, R. F. Boyer, and S.M.Stoesser, *Styrene: Its Polymers, Copolymers and Derivatives* (Hafner Pub. Co., New York, 1970).
- [102] A. B. Djuricic, and B. V. Stanic, "Modeling the temperature dependence of the index of refraction of liquid water in the visible and the near-ultraviolet ranges by a genetic algorithm," *Applied Optics* **38**, 11-17 (1999).
- [103] P. D. T. Huibers, "Models for the wavelength dependence of the index of refraction of water," *Applied Optics* **36**, 3785-3787 (1997).
- [104] B. C. Wilson, M. S. Patterson, and S. T. Flock, "Indirect Versus Direct Techniques for the Measurement of the Optical-Properties of Tissues," *Photochemistry and Photobiology* **46**, 601-608 (1987).
- [105] A. Kienle, L. Lilge, M. S. Patterson, R. Hibst, R. Steiner, and B. C. Wilson, "Spatially resolved absolute diffuse reflectance measurements for noninvasive determination of the optical scattering and absorption coefficients of biological tissue," *Applied Optics* **35**, 2304-2314 (1996).
- [106] S. A. Prahl, ed. *The adding-doubling method* (Plenum press, New York and London, 1995).

- [107] A. Amelink, H. Sterenborg, M. P. L. Bard, and S. A. Burgers, "In vivo measurement of the local optical properties of tissue by use of differential path-length spectroscopy," *Optics Letters* **29**, 1087-1089 (2004).
- [108] T. P. Moffitt, and S. A. Prahl, "Sized-fiber reflectometry for measuring local optical properties," *IEEE Journal of Selected Topics in Quantum Electronics* **7**, 952-958 (2001).
- [109] P. Thueller, I. Charvet, F. Bevilacqua, M. St Ghislain, G. Ory, P. Marquet, P. Meda, B. Vermeulen, and C. Depeursinge, "In vivo endoscopic tissue diagnostics based on spectroscopic absorption, scattering, and phase function properties," *Journal of Biomedical Optics* **8**, 495-503 (2003).
- [110] G. M. Palmer, and N. Ramanujam, "Use of genetic algorithms to optimize fiber optic probe design for the extraction of tissue optical properties," *IEEE Transactions on Biomedical Engineering* **54**, 1533-1535 (2007).
- [111] D. Sharma, A. Agrawal, L. S. Matchette, and T. J. Pfefer, "Evaluation of a fiberoptic-based system for measurement of optical properties in highly attenuating turbid media," *Biomedical Engineering Online* **5**, Art. No. 49 (2006).
- [112] H.-J. Wei, D. Xing, J.-J. Lu, H.-M. Gu, G.-Y. Wu, and Y. Jin, "Determination of optical properties of normal and adenomatous human colon tissues *in vitro* using integrating sphere techniques," *World Journal of Gastroenterology* **11**, 2413-2419 (2005).
- [113] J. S. Dam, C. B. Pedersen, T. Dalgaard, P. E. Fabricius, P. Aruna, and S. Andersson-Engels, "Fiber-optic probe for noninvasive real-time determination of tissue optical properties at multiple wavelengths," *Applied Optics* **40**, 1155-1164 (2001).
- [114] S. R. Millon, K. M. Roldan-Perez, K. M. Riching, G. M. Palmer, and N. Ramanujam, "Effect of optical clearing agents on the in vivo optical properties of squamous epithelial tissue," *Lasers in Surgery and Medicine* **38**, 920-927 (2006).
- [115] M. J. C. v. Gemert, A. J. Welch, and W. M. Star, eds., *One-dimensional transport theory* (Plenum press, New York and London, 1995).
- [116] S. A. Prahl, "The diffusion approximation in three dimensions," in *Optical-Thermal Response of Laser Irradiated Tissue*, Welch A. J., and Gemert M. J. C. V., eds. (Plenum press, New York and London, 1995), pp. 207-231.
- [117] L. Reynolds, C. Johnson, and A. Ishimaru, "Diffuse reflectance from a finite blood medium - applications to modeling of fiber optic catheters," *Applied Optics* **15**, 2059-2067 (1976).
- [118] B. C. Wilson, and G. Adam, "A Monte-Carlo model for the absorption and flux distributions of light in tissue," *Medical Physics* **10**, 824-830 (1983).
- [119] M. Keijzer, S. L. Jacques, S. A. Prahl, and A. J. Welch, "Light distributions in artery tissue - Monte-Carlo simulations for finite-diameter laser-beams," *Lasers in Surgery and Medicine* **9**, 148-154 (1989).
- [120] M. Keijzer, J. W. Pickering, and M. J. C. Vangemert, "Laser-beam diameter for Port wine stain treatment," *Lasers in Surgery and Medicine* **11**, 601-605 (1991).
- [121] S. T. Flock, M. S. Patterson, B. C. Wilson, and D. R. Wyman, "Monte-Carlo modeling of light-propagation in highly scattering tissues .1. Model predictions and comparison with diffusion-theory," *IEEE Transactions on Biomedical Engineering* **36**, 1162-1168 (1989).
- [122] S. T. Flock, B. C. Wilson, and M. S. Patterson, "Monte-Carlo modeling of light-propagation in highly scattering tissues .2. Comparison with measurements in phantoms," *IEEE Transactions on Biomedical Engineering* **36**, 1169-1173 (1989).
- [123] L. H. Wang, S. L. Jacques, and L. Q. Zheng, "Mcml - Monte-Carlo modeling of light transport in multilayered tissues," *Computer Methods and Programs in Biomedicine* **47**, 131-146 (1995).
- [124] Q. Liu, and N. Ramanujam, "Scaling method for fast Monte Carlo simulation of diffuse reflectance spectra from multilayered turbid media," *Journal of the Optical Society of America a-Optics Image Science and Vision* **24**, 1011-1025 (2007).
- [125] R. Graaff, M. H. Koelink, F. F. M. Demul, W. G. Zijlstra, A. C. M. Dassel, and J. G. Aarnoudse, "Condensed Monte-Carlo simulations for the description of light transport," *Applied Optics* **32**, 426-434 (1993).

- [126] G. M. Palmer, and N. Ramanujam, "Monte Carlo-based inverse model for calculating tissue optical properties. Part I: Theory and validation on synthetic phantoms," *Applied Optics* **45**, 1062-1071 (2006).
- [127] T. J. Farrell, B. C. Wilson, and M. S. Patterson, "The use of a neural network to determine tissue optical-properties from spatially resolved diffuse reflectance measurements," *Physics in Medicine and Biology* **37**, 2281-2286 (1992).
- [128] C. Svaneborg, and J. S. Pedersen, "Monte Carlo simulations and analysis of scattering from neutral and polyelectrolyte polymer and polymer-like systems," *Current Opinion in Colloid & Interface Science* **8**, 507-514 (2004).
- [129] C. M. Ma, and S. B. Jiang, "Monte Carlo modelling of electron beams from medical accelerators," *Physics in Medicine and Biology* **44**, R157-R189 (1999).
- [130] F. Verhaegen, and J. Seuntjens, "Monte Carlo modelling of external radiotherapy photon beams," *Physics in Medicine and Biology* **48**, R107-R164 (2003).
- [131] R. Gauvin, E. Lifshin, H. Demers, P. Horny, and H. Campbell, "Win X-ray: A new Monte Carlo program that computes X-ray spectra obtained with a scanning electron microscope," *Microscopy and Microanalysis* **12**, 49-64 (2006).
- [132] M. Yasuda, R. Katsuse, H. Kawata, and K. Murata, "A Monte Carlo study of magnetic domain images in a spin-polarized scanning electron microscope," *Japanese Journal of Applied Physics Part 1-Regular Papers Short Notes & Review Papers* **41**, 4246-4249 (2002).
- [133] T. Yoshida, K. Nishikata, T. Nagatomi, Y. Kimura, and Y. Takai, "Monte Carlo simulation study of backscattered electron imaging in a chemical vapor deposition scanning electron microscope," *Japanese Journal of Applied Physics Part 1-Regular Papers Short Notes & Review Papers* **40**, 3457-3462 (2001).
- [134] R. Shimizu, and K. Murata, "Monte Carlo Calculations of Electron-Sample Interactions in Scanning Electron Microscope," *Journal of Applied Physics* **42**, 387-394 (1971).
- [135] D. E. Newbury, H. Yakowitz, and Myklebus, R.I, "Monte-Carlo Calculations of Magnetic Contrast from Cubic Materials in Scanning Electron-Microscope," *Applied Physics Letters* **23**, 488-490 (1973).
- [136] M. M. Elgomati, and M. Prutton, "Monte-Carlo Calculations of Spatial-Resolution in a Scanning Auger-Electron Microscope," *Surface Science* **72**, 485-494 (1978).
- [137] L. Wang, and S. L. Jacques, "Monte Carlo Modeling of Light Transport in Multi-layered Tissues in Standard C," Wang L., and Jacques S. L., eds. (University of Texas M.D. Anderson Cancer Center, 1998).
- [138] J. R. Mourant, I. J. Bigio, D. A. Jack, T. M. Johnson, and H. D. Miller, "Measuring absorption coefficients in small volumes of highly scattering media: Source-detector separations for which path lengths do not depend on scattering properties," *Applied Optics* **36**, 5655-5661 (1997).
- [139] R. Graaff, J. G. Aarnoudse, F. F. M. Demul, and H. W. Jentink, "Similarity relations for anisotropic scattering in absorbing media," *Optical Engineering* **32**, 244-252 (1993).
- [140] C. F. Bohren, and D. R. Huffman, *Absorption and Scattering of Light by Small Particles* (Wiley-Interscience, 1998).
- [141] Q. Liu, C. F. Zhu, and N. Ramanujam, "Experimental validation of Monte Carlo modeling of fluorescence in tissues in the UV-visible spectrum," *J Biomed Opt* **8**, 223-236 (2003).
- [142] G. M. Palmer, C. L. Marshek, K. M. Vrotsos, and N. Ramanujam, "Optimal methods for fluorescence and diffuse reflectance measurements of tissue biopsy samples," *Lasers in Surgery and Medicine* **30**, 191-200 (2002).
- [143] R. Marchesini, E. Pignoli, S. Tomatis, S. Fumagalli, A. E. Sichirollo, S. Dipalma, M. Dalfante, P. Spinelli, A. C. Croce, and G. Bottiroli, "Ex-vivo optical-properties of human colon tissue," *Lasers in Surgery and Medicine* **15**, 351-357 (1994).
- [144] C. Holmer, K. S. Lehmann, J. Wanken, C. Reissfelder, A. Roggan, G. Mueller, H. J. Buhr, and J. P. Ritz, "Optical properties of adenocarcinoma and squamous cell carcinoma of the gastroesophageal junction," *Journal of Biomedical Optics* **12**, 014025 (2007).

- [145] G. I. Zonios, R. M. Cothren, J. T. Arendt, J. Wu, J. VanDam, J. M. Crawford, R. Manoharan, and M. S. Feld, "Morphological model of human colon tissue fluorescence," *IEEE Transactions on Biomedical Engineering* **43**, 113-122 (1996).
- [146] R. L. P. van Veen, W. Verkruysse, and H. Sterenborg, "Diffuse-reflectance spectroscopy from 500 to 1060 nm by correction for inhomogeneously distributed absorbers," *Optics Letters* **27**, 246-248 (2002).
- [147] W. J. Cui, and L. E. Ostrander, "The Relationship of Surface Reflectance Measurements to Optical-Properties of Layered Biological Media," *IEEE Transactions on Bio-medical Engineering* **39**, 194-201 (1992).
- [148] I. Seo, J. S. You, C. K. Hayakawa, and V. Venugopalan, "Perturbation and differential Monte Carlo methods for measurement of optical properties in a layered epithelial tissue model," *Journal of Biomedical Optics* **12**, 014030 (2007).
- [149] J. P. Ritz, A. Roggan, C. Isbert, G. Muller, H. J. Buhr, and C. T. Germer, "Optical properties of native and coagulated porcine liver tissue between 400 and 2400 nm," *Lasers in Surgery and Medicine* **29**, 205-212 (2001).
- [150] P. Parsa, S. L. Jacques, and N. S. Nishioka, "Optical-properties of rat-liver between 350 and 2200 nm," *Applied Optics* **28**, 2325-2330 (1989).
- [151] V. Tuchin, *Tissue Optics* (The International Society for Optical Engineering, Bellingham, Washington USA, 2000).
- [152] A. A. Oraevsky, S. L. Jacques, G. H. Pettit, I. S. Saidi, F. K. Tittel, and P. D. Henry, "Xecl Laser Ablation of Atherosclerotic Aorta - Optical-Properties and Energy Pathways," *Lasers in Surgery and Medicine* **12**, 585-597 (1992).
- [153] M. Keijzer, R. R. Richardskortum, S. L. Jacques, and M. S. Feld, "Fluorescence Spectroscopy of Turbid Media - Autofluorescence of the Human Aorta," *Applied Optics* **28**, 4286-4292 (1989).
- [154] I. J. Bigio, S. G. Bown, G. Briggs, C. Kelley, S. Lakhani, D. Pickard, P. M. Ripley, I. G. Rose, and C. Saunders, "Diagnosis of breast cancer using elastic-scattering spectroscopy: preliminary clinical results," *Journal of Biomedical Optics* **5**, 221-228 (2000).
- [155] T. M. Breslin, F. S. Xu, G. M. Palmer, C. F. Zhu, K. W. Gilchrist, and N. Ramanujam, "Autofluorescence and diffuse reflectance properties of malignant and benign breast tissues," *Annals of Surgical Oncology* **11**, 65-70 (2004).
- [156] T. Papaioannou, N. W. Preyer, Q. Y. Fang, A. Brightwell, M. Carnohan, G. Cottone, R. Ross, L. R. Jones, and L. Marcu, "Effects of fiber-optic probe design and probe-to-target distance on diffuse reflectance measurements of turbid media: an experimental and computational study at 337 nm," *Applied Optics* **43**, 2846-2860 (2004).
- [157] P. R. Bargo, S. A. Prahl, and S. L. Jacques, "Collection efficiency of a single optical fiber in turbid media," (2003), pp. 3187-3197.
- [158] A. F. Gmitro, F. W. Cutruzzola, M. L. Stetz, and L. I. Deckelbaum, "Measurement depth of laser-induced tissue fluorescence with application to laser angioplasty," *Applied Optics* **27**, 1844-1849 (1988).
- [159] T. J. Pfefer, D. Y. Paithankar, J. M. Poneris, K. T. Schomacker, and N. S. Nishioka, "Temporally and spectrally resolved fluorescence spectroscopy for the detection of high grade dysplasia in Barrett's esophagus," *Lasers in Surgery and Medicine* **32**, 10-16 (2003).
- [160] N. Ramanujam, M. F. Mitchell, A. Mahadevan, S. Warren, S. Thomsen, E. Silva, and R. Richards-Kortum, "In-vivo diagnosis of cervical intraepithelial neoplasia using 337-nm-excited laser-induced fluorescence," *Proceedings of the National Academy of Sciences of the United States of America* **91**, 10193-10197 (1994).
- [161] U. Utzinger, and R. R. Richards-Kortum, "Fiber optic probes for biomedical optical spectroscopy," *Journal of Biomedical Optics* **8**, 121-147 (2003).
- [162] T. J. Pfefer, L. S. Matchette, A. M. Ross, and M. N. Ediger, "Selective detection of fluorophore layers in turbid media: the role of fiber-optic probe design," *Optics Letters* **28**, 120-122 (2003).

- [163] T. J. Pfefer, K. T. Schomacker, M. N. Ediger, and N. S. Nishioka, "Light propagation in tissue during fluorescence spectroscopy with single-fiber probes," *IEEE Journal of Selected Topics in Quantum Electronics* **7**, 1004-1012 (2001).
- [164] L. Quan, and N. Ramanujam, "Relationship between depth of a target in a turbid medium and fluorescence measured by a variable-aperture method," *Optics Letters* **27**, 104-106 (2002).
- [165] N. Rajaram, T. H. Nguyen, and J. W. Tunnell, "Lookup table-based inverse model for determining optical properties of turbid media," *Journal of Biomedical Optics* **13**, (2008).
- [166] G. M. Palmer, C. F. Zhu, T. M. Breslin, F. S. Xu, K. W. Gilchrist, and N. Ramanujam, "Monte Carlo-based inverse model for calculating tissue optical properties. Part II: Application to breast cancer diagnosis," *Applied Optics* **45**, 1072-1078 (2006).
- [167] C. F. Zhu, Q. Liu, and N. Ramanujam, "Effect of fiber optic probe geometry on depth-resolved fluorescence measurements from epithelial tissues: a Monte Carlo simulation," *Journal of Biomedical Optics* **8**, 237-247 (2003).
- [168] G. H. Weiss, R. Nossal, and R. F. Bonner, "Statistics of penetration depth of photons re-emitted from irradiated tissue," *J. Mod. Opt.* **36**, 349-359 (1989).
- [169] T. J. Pfefer, K. T. Schomacker, M. N. Ediger, and N. S. Nishioka, "Multiple-fiber probe design for fluorescence spectroscopy in tissue," *Applied Optics* **41**, 4712-4721 (2002).
- [170] T. J. Farrell, M. S. Patterson, and M. Essenpreis, "Influence of layered tissue architecture on estimates of tissue optical properties obtained from spatially resolved diffuse reflectometry," *Appl. Optics* **37**, 1958-1972 (1998).
- [171] C. K. Hayakawa, J. Spanier, F. Bevilacqua, A. K. Dunn, J. S. You, B. J. Tromberg, and V. Venugopalan, "Perturbation Monte Carlo methods to solve inverse photon migration problems in heterogeneous tissues," *Optics Letters* **26**, 1335-1337 (2001).
- [172] C. M. Gardner, and A. J. Welch, Biomedical Engineering Program, University of Texas, Austin (personal communication, 1992).
- [173] S. K. Chang, D. Arifler, R. Drezek, M. Follen, and R. Richards-Kortum, "Analytical model to describe fluorescence spectra of normal and preneoplastic epithelial tissue: comparison with Monte Carlo simulations and clinical measurements," *Journal of Biomedical Optics* **9**, 511-522 (2004).